OF 1915

F
~~8482~~

168

ANALELE UNIVERSITATII BUCURESTI

FIZICĂ

ANUL XIX — 1970

ANALELE UNIVERSITĂȚII BUCUREȘTI

BUDAPESTI MŰSZAKI ÉS GAZDASÁGTUDOMÁNYI EGYETEM
Országos Műszaki Információs Központ és Könyvtár
2001

FIZICĂ

ANUL XIX — 1970

1989

FIZICĂ

BME KÖZPONTI KÖNYVTÁR
F
8432
FOLYÓIRAT OSZTÁLY

COMITETUL DE REDACŢIE

Redactor responsabil: Prof. dr. docent *Gheorghe Brătescu*

Membri: Acad. prof. dr. docent *Th. V. Ionescu*; acad. prof. dr. docent *Şerba* *Ţiţeica*; prof. dr. docent *Ion Ursu*; prof. dr. docent *V. Novacu*; prof dr. *Cristian Constantinescu*; prof. dr. *Mihai Rosenberg*; prof. dr *Mihai Gavrilă*

Secretar: Lector dr. *Constantin Vrejoiu*

BUDAPESTI MŰSZAKI EGYETEM
1848
KÖZPONTI KÖNYVTÁRA

Budapesti Műszaki Egyetem
Központi Könyvtára
Folyóiratállár
P298/1942

REDACŢIA
ANALELE UNIVERSITĂŢII BUCUREŞTI
B-dul Gh. Gheorghiu-Dej nr. 64
Telefon 160187/5

SUMAR

Pag.

I. GANOVICI și FL. NICHITIU: Asupra determinării densității bulelor în camera cu bule 9
ST. LEVAI și D. BORȘAN: Relaxometru de rezonanță magnetică nucleară 19
C. I. NISTOR și A. E. DRUKER: Erorile standard ale parametrilor spectrelor de formă Lorentz și Gauss 27
C. I. NISTOR și C. LULEA: Programe pentru analiza spectrelor Mossbauer.... 35
G. G. BRĂTESCU, I. IOVA, FLORIANA MOLDOVEANU și HRISTINA CULICĂ: Asupra fenomenelor de excitare într-o nouă sursă spectrală Korolev 39
EMIL I. TOADER: Pierderile prin difuzie și recombinare de volum în plasma unei descărcări în neon 49
MARIA COMĂNESCU: Temperatura electronilor într-o descărcare normală în hidrogen, oxigen, argon și heliu în curent continuu.......... 55
G. G. BRĂTESCU și T. TUDOR: Legea propagării funcției de coerență mutuală generalizată 91
G. G. BRĂTESCU: Asupra aberațiunilor de ordinul trei la sistemele optice centrate 97
ST. TUDORACHE: Calculul secțiunilor eficiente ale transferului de excitație prin ciocnire atomică. Cazul atomilor alcalini de tipuri diferite.......... 113
I. SPÎNULESCU-CARNARU și C. STĂNESCU: Memorie nedestructivă realizată cu straturi subțiri feromagnetice și traductori Hall.......... 123
C. STĂNESCU și I. SPÎNULESCU-CARNARU: Circuite logice cu trei valori realizate cu transzistori pe straturi subțiri și de tip Mos.......... 127
I. DIMA: Marginea absorbției fundamentale a selenurii de zinc.......... 133

СОДЕРЖАНИЕ

Стр.

И. ГАНОВИЧ и ФЛ. НИКИТЬЮ: Об измерении плотности пузырьков в пузырьковых камерах 9

ПТ. ЛЕВАЙ и Д. БОРШАН: ЯМР релаксометр 26

К. И. НИСТОР и А. Е. ДРУКЕР: Стандартные статистические ошибки параметров резонансов формы Лоренц и Гаусс..................... 27

К. И. НИСТОР и К. ЛУЛЯ: Программы для анализа Мёссбауэровских спектров 35

Г. Г. БРЭТЕСКУ, И. ИОВА, Р. МОЛДОВЯНУ, и Х. КУЛИКЭ: Возбужденные процессы в новом сорте спектрального коралевского источника.. 39

ЭМИЛ И. ТОАДЕР: Потери носителей разряда в неоном плазме вызванным рекомбинацией и диффузией 49

М. КОМЭНЕСКУ: Электронная температура в нормальном разряде постоянного тока в водороде, кислороде, гелий и органе. 55

Г. Г. БРЭТЕСКУ и Г. ТУДОР: Закон распространения общей функции взаимной когерентности 91

Г. Г. БРЭТЕСКУ: Ол оберации третьэй степени центрированных оптичэских систем 97

ШТ. ТУДОРАКЕ: Расчет эффективного сечения переноса возбуждения при атомных столкновениях 113

И. СПЫНДУЛЕСКУ-КАРНАРУ и К. СТЭНЕСКУ: Несломящаяся память на тонких ферромагнитных пленках и традикторов Холла 123

К. СТЭНЕСКУ и И. СПЫНУЛЕСКУ-КАРНАРУ: Трех — значений логические цепи реализованы на основе транзисторов в тонких пленках и транзисторов MOS 127

И. ДИМА: Край основного поглощения селенида цинка 133

SUMMARY

Page

I. GANOVICI and FL. NICHITIU: On Bubble Density Determination in Bubble Chambers 9
ST. LEVAI and D. BORȘAN: MNR Relaxometer 26
C. I. NISTOR and A. E. DRUKER: Parameters Standard Errors of Lorentz and Gauss Form Spectra 27
C. NISTOR and C. LULEA: Programs for the Analysis of Mossbauer Spectres.... 35
G. G. BRĂTESCU, I. IOVA, FLORIANA MOLDOVEANU, et HRISTINA CULICĂ: Sur les phénomènes d'excitation dans une nouvelle source spectrale Korolev 39
EMIL I. TOADER: Volume Recombination and Diffusion Losses in a Neon Discharge Plasma 49
MARIA COMĂNESCU: The Electron Temperature in a Normal Discharge in Hydrogen, Oxygen, Helium and Argon in D.C. Current.......... 55
G.G. BRĂTESCU et T. TUDOR: La loi de propagation de la fonction de cohérence mutuelle généralisée 91
G. G. BRĂTESCU: Sur les aberrations de troisième ordre des systèmes optiques centrés 97
ST. TUDORACHE: Calculus of Efficient Cross-sections of Excitation Transfer by Atomic Collisions. The Case of Alkaline Atoms of Various Types.. 113
I. SPÎNULESCU-CARNARU and C. STĂNESCU: A Non-destructive Thin-film Ferromagnetic-hall Memory 123
C. STĂNESCU and I. SPÎNULESCU-CARNARU: Three Value Logical Circuits Realized with MOS-transistors and thin-film Transistors 127
I. DIMA: The Fundamental Absorption Edge of the Zinc Selenide.............. 133

ON BUBBLE DENSITY DETERMINATION IN BUBBLE CHAMBERS

I. GANOVICI and FL. NICHITIU

The gap distribution function was extended for negative gaps and the mean length of the gaps, the lacunarity and the gap density were calculated for two possibility: when the blobs were not considered and when the blobs were considered. The bubbles density g, was proposed to be determined from the mean value of the bubble + blob size $(\overline{D_{b+B}})$.

The determination of the ionization caused by a charged particle in a bubble chamber, may help mass particle identification. One way to check ionization is to determine bubble density, g, along the particle track in the bubble chamber; hence, in practice, the identification is achieved according to the value of g. Having measured some typical track parameters (gap mean length, blob mean size, gap density), and having established their dependence on g, this important parameter can be determined. There will occur some difficulties in g determination, they can be dealt with from two different points of view: experimental difficulties due to the requirement to measure a large number of bubbles (large size bubble chambers) to get a good statistics and difficulties due to the superpositions of the bubbles, engendering „blobs".

This paper will discuss the interdependence of different experimenta- parameters when the blobs are not measured, starting with the gap distril bution function[1-3].

We have extended these distribution functions to include the superimposed bubble case, thereby establishing the term of the negative gaps between the bubbles.

We have also sugested an alternative method for the g determination by including the blobs in measurements; the method to measure the experimental values and their interdependence is given. There are also given informations to be got with the distribution functions extended for the general parameters characterising the blobs.

The symbols given in fig. 1 are agreed to be used in the discution to folow.

It is generally considered that the occurence of the ionization centers is hazardous, hence Poisson probability will give the distance distribution, l,

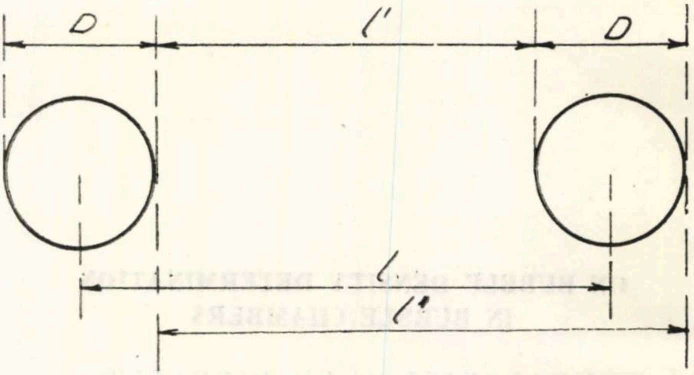

Fig. 1 – The distance definitions between two bubbles

between the succesive bubbles or its equivalent distance l''. Being normed on the complete variation gap range of l'', $(0, \infty)$, the probabiliy tis $\varphi(l'') = g \cdot \exp\,(-\,gl'')$ and the distribution function becomes $N(l'') = N_0 \cdot g \cdot \exp\,(-\,gl'')$, where g is the bubble or gap density, being function of the particle speed and mass, the nature of the liquid in the bubble chamber and the exposure conditions, while N_0 is the total number of the gaps on the track.

When considering the particule track on a film image whith the track on the Ox axis length, measurement technique, if applied to separate bubbles given: $l'_1 = x_3 - x_2$, $D_1 = x_2 - x_1$, $l''_1 = x_4 - x_2$, the directly experimentally determined parameters being the coordinates $x_1, x_2, x_3, \ldots$ (fig. 2).

In a more general case, when the track is not on the Ox axis, for each and every point, the pair of the coordinates x, y in the film plan will be measured, the distance between the point being consequently calculated.

We have extended the method, at least theoretically, to the superimposed bubbles taking l' as the oriented distance between the end of a bubble, point 2, and the beginning of the next bubble, point 3. The gap l' will always be calculated as the difference between the coordinate of the beginning point minus the coordinate of the end point of the preceding bubble $(x_3 - x_2)$, even if the bubbles are superimposed. Thus, $l'_3 = x_7 - x_6$ and $l''_3 = x_8 - x_6$; hence, under the assumption we made, l' can assume negative values too (the meaning of the negative vlaues concerning only the direction of the beginning-end succession). Thus values will vary within

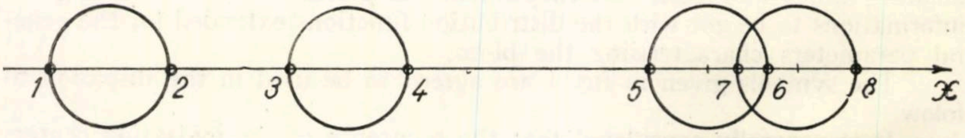

Fig. 2 – The coordonate definitions for the beginning-end of the bubbles

$-D \leqslant l' < \infty$ and $0 \leqslant l'' < \infty$, respectively; the values $l' = -D$ and $l'' = 0$ are obtained when the bublcs are completely superimposed, hence the point 7 with 5, and 8 with 6, respectively. Under these conditions, the probability of having a gap l' between the bubbles will become $\psi(l') = g \cdot \exp(-gD \cdot \exp(-gl')$ while the distribution function $N(l') = N_0 g \cdot \exp(-gD) \cdot \exp(-gl')$ normed on the range $(-D, \infty)$ and not on the range $(0, \infty)$ at it is commonly used[4–7].

We have considered constant the bubble diameter D; its value is given by the mean value for the Gaussian distribution resulted from the measurement carried on separate bubbles.

When identifying a particle according to g, the people engaged in the experiment are faced with two methods. The parameters that are commonly used to determine g will be measured either avoiding the blobs or taking them into account. These two cases will be analysed.

1. BLOBS ARE AVOIDED

Making use of the above distribution functions, resulted from the theoretical hypothesis of a perfect separation of the bubbles, even when superimposed, the parameters experimentally used to determine g were calculated. The calculation results for the mean length of the $\bar{l}'$ and $\bar{l}''$ gap, lacunarity ν and bubble or gap density n, are given in the columns of the tabel 1 and they represent three measurement hypotheses, namely:

1) there is the possibility (the theotetical case) to distinguish the bounderies of the separate bubbles even when superimposed ($-D \leqslant l' < \infty$ and $0 \leqslant l'' < \infty$);

2) there is the possibility to distinguish separate bubbles if tangent or distinct from one another;

3) the distance between the bubbles is considered as a "gap" only if it exceeds α. The resolution α is usually taekn $D/2$ ($D/2 = \alpha \leqslant l' < \infty$ and $3D/2 = \beta \leqslant l'' < \infty$).

The only case that can be experimentally analysed is the last one, on condition that the parameters l', l'', D are measured as in fig. 3, eliminating the blobs but measuring l' and l'' from the front of the blob.

In the last column of the table, the method to measure experimentally each parameter is indicated.

The meaning of g is obviously revealed by the results we have got as being the gap density, n, when considering all gaps N_0 (the negative gaps suggested here, included) on the whole length L of the track; hence $g = N_0/L$. The value $1/g$ corresponds to the medium gaps in two different situations: for l' when the measurement is made on the tangent bubbles and for l'' when the measurement (the theoretical one) is made on the superimposed bubbles, that is for both cases the same range $(0, \infty)$. For a real

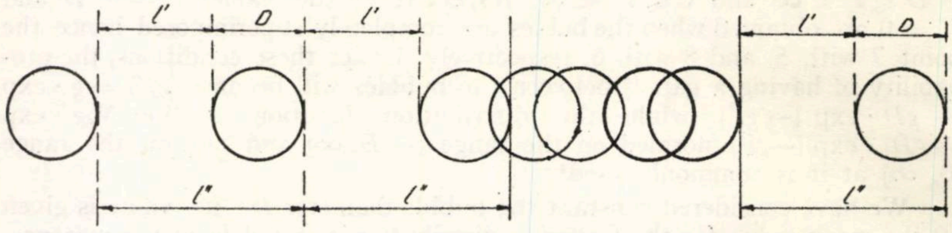

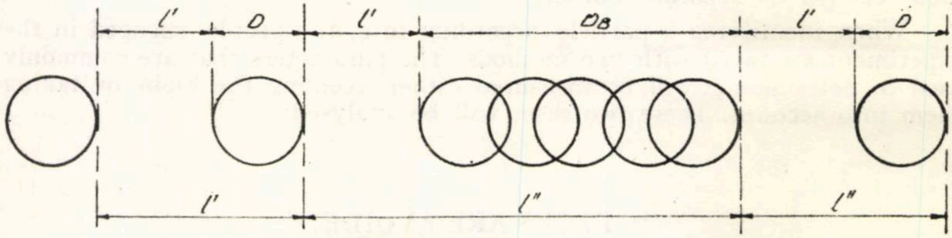

Fig. 3 — Measurement method when the blobs are eliminated

Fig. 4 — Measurement method when the blobs are not eliminated

measurement, with a resolution α, the parameters l' and l'' will be corrected with α and $\beta = D + \alpha$, respectively; it results:

$$\bar{l}' = \alpha + \frac{1}{g} \quad \bar{l}'' = \beta + \frac{1}{g} \tag{1}$$

Similarly, the values for the lacunarity ν and the gap density n are corrected. When measuring ν and n, the case when the blobs present are eliminated, it is normal not to relate ν and n to the whole length L of the track (as it is usually done) but to a blobless track section $\Sigma l''(l'' > \beta)$ as it was in the tabel 1. This is aecounted by the fact that inside the blobs, ν and n have different values from those outside the blobs.

Hence, leaving the blobs aside, g can be determined from $\bar{l}'$, $\bar{l}''$, ν, n, experimentally measured and by using the relations in the tabel 1, but only one of them being independent, $e \cdot g \cdot \bar{l}'$. Between these parameters there are obvious relation:

$$\bar{l}'' = \bar{l}' + D; \quad \frac{\bar{l}'}{\bar{l}''} = \frac{\bar{l}'}{\bar{l}' + D}; \quad n = \frac{1}{\bar{l}''} = \frac{1}{\bar{l}' + D} \tag{2}$$

The relations we discussed, apart from the parameter experimentally measured, may also include the diameter of the separate bubbles; it has to be separately determined. D is a parameter that is function of the time the picture is tacken and less of ionization. D has its part also in but not exclussively, because an alternative experimental parameter, independent of D can be selected for the resolution.

TABEL 1

The parameters used to determine g when the blobs are not measured.

Parameter	Range of measurement			rimental emethods
	$-D \leqslant l' < \infty$ $0 \leqslant l' < \infty$	$0 \leqslant l' < \infty$ $D \leqslant l'' < \infty$	$D/2 = \alpha \leqslant l' < \infty$ $3D/2 = \beta \leqslant l'' < \infty$	
$\bar{l}' = \dfrac{\int_\alpha^\infty l' \mathrm{n}(l') \cdot dl'}{\int_\alpha^\infty n(l') \cdot dl'}$	$-D + \dfrac{1}{g}$	$\dfrac{1}{g}$	$\alpha + \dfrac{1}{g}$	$\dfrac{\Sigma l'(> \alpha)}{\text{gap numbers } l' < \alpha}$
$\bar{l}'' = \dfrac{\int_\beta^\infty l'' n(l'') \cdot dl''}{\int_\beta^\infty n(l'') \cdot dl''}$	$\dfrac{1}{g}$	$D + \dfrac{1}{g}$	$\beta + \dfrac{1}{g}$	$\dfrac{\Sigma l''(> \beta)}{\text{gap number } l'' > \beta}$
$\nu = \dfrac{\int_\alpha^\infty l' n(l') \cdot dl'}{\int_\beta^8 l'' n(l'') \cdot dl''}$	$1 - Dg$	$\dfrac{1}{1 + Dg}$	$\dfrac{1 + \alpha g}{1 + \beta g}$	$\dfrac{\Sigma l'(> \alpha)}{\Sigma l''(> \beta)}$
$n = \dfrac{\int_\alpha^\infty n(l') \cdot dl'}{\int_\beta^\infty l'' \cdot n(l'') \cdot dl''}$	g	$\dfrac{1}{1 + Dg}$	$\dfrac{1}{1 + \beta g}$	$\dfrac{\text{gap number } l'' > \beta}{\Sigma l''(> \beta)}$

2. BLOBS ARE TAKEN INTO ACCOUNT

The parameters discussed above will be extended for the case when the blobs are taken into account, both experimentally and from the point of view of the calculation, on condition that the measurement should follow fig. 4. The required alternations in the experimental measurement include not only the determination of the bubble diameters, D_b but also the blob sizes, D_B; while in the blob vecinity, both l' and l'' will be measured as if the blob were a bubble of different dimensions.

From the previously described parameters, it is only $\bar{l}'$ that remains uncharged in this latter case, as it operates only with gaps.

smaller than α (negative gaps, included). In the theoretical case of a perfect resolution ($\alpha = 0$) when the track have no longer blobs because the blobbes can be distinguished even if superimposed, there is only one independent parameter left, $\bar{l}'$, D becoming constant as the negative gaps are abstent.

The simplest basic relation to measure g in the two cases are

$$\bar{l}' = \frac{\Sigma l'(> \alpha)}{N_0'} = \frac{1}{g} + \alpha ; \quad \bar{l}''_B = \frac{L}{N_0^1} = \frac{1}{g} \cdot \exp\left[g \cdot (D + \alpha)\right] \tag{10}$$

They include informations either only on the range $\alpha \infty l' < \leqslant$ or on the whole range $-D \infty l' < \leqslant$. The measurements that take into account blobs are more general because they allow the use of all the information on the track.

But, from a mathematical point of view, blobs can be considered with difficulty as g cann't be directly explained.

Up to now there was developed no distribution function for the length of the blobs. The only parameters that can be experimentally measured and related to the information resulted from the gap distribution functions are ΣD_B and N_B — the number of the blobs.

In measurements, the distribution of the bubbles according to their diameter, includes a Gaussian section due to the individual bubbles that show measurement errors; this section is followed by a tail of large diameters, because of the blobs.

The number N_B illustrates the difference between the total number of the bubbles and blobs, N_0', and the bubbles with the Gaussian distribution. Making use of $\varphi(l'')$, the sum of the blobs dimensions was calculated.

$$\Sigma D_B = D \cdot N_B + \Sigma l''(< \beta) = D \cdot N_B + L[1 - (1 + \beta g) \cdot \exp(-g\beta)] \tag{11}$$

This relationship permits the checking of the above statements by substitution of the experimental values ΣD_B, N_B and g that was determined by another simpler method.

It is wortly noting that the total number of the superimposed bubbles included in the blobs can be evaluated: the number of the superimposed bubbles $= N_B +$ the gap number

$$l'(< \alpha) = N_B + Lg \cdot \{1 - \exp[-g(D + \alpha)]\} \tag{12}$$

Both the sum of the bubble dimensions and their number represent, at least for the time being, general informations on all the blobs in the track without being yet able establish their distribution.

At the beginning we consider the number of the objects on the track N'_0, the separate bubbles and blobs, that is equal to the number of the gaps larger than

$$N'_0 = \int_\alpha^\infty N(l')dl' = N_0 \exp[-g(D+\alpha)] \tag{3}$$

In order to include the blobs in the lacunarity it is necessary to relate it to the total track length L, that is to define it as $\nu_B = \Sigma l'(>\alpha)/L$. The value of ν_B was calculated from the distribution function

$$\nu_B = \frac{1}{L}\int_\alpha^\infty l'N(l')dl' = (1+\alpha g)\cdot\exp[-g(D+\alpha)] \tag{4}$$

The value of g can be determined using ν_B, measured experimentally and the relation (4).

The experimental determination of $L = \Sigma l'(>\alpha) + \Sigma D_{b+B}$ will include both the sum of the gaps $l' > \alpha$ and the sum of the blob and bubble dimensions (ΣD_{b+B}). The quantity D_{b+B}, related to N'_0 gives D_{b+B}, a mean value calculated for all the objects in the track. Thus, the lacunarity relation becomes:

$$\nu_B = \frac{\Sigma l'(>\alpha)}{L} = \frac{\Sigma l'(>\alpha)}{\Sigma l'(>\alpha) + \Sigma D_{b+B}} \cdot \frac{N'_0}{N'_0} = \frac{\bar{l}'}{\bar{l}' + \overline{D_{b+B}}} \tag{5}$$

Substituting (4) and (1) in (5), one gets

$$\overline{D_{b+B}} = \frac{1}{g}[\exp(g\beta) - 1 - \alpha g] = D + \frac{1}{g}[\exp(g\beta) - 1 - \beta g)] \tag{6}$$

The experimental determination represents a new method that we suggest to determine g from (6). The value of $\overline{D_{b+B}}$ is function of g and makes it possible to calculate it, when D does not depend on g. This is quite natural for in case the blobs are included in the calculation, we took in fact into account the negative gaps l', we have already introduced, they depending on g. To pass over from the formulas that do take into account blobs to those leaving them aside is in fact to pass over from $\overline{D_{b+B}}$ to D, N'_0 to N_0 and ν_B in the tabel 2 to ν in the tabele 1.

The mean length of the gap l'' when taking into account the measured blobs as it was suggested in fig. 4 will have the form $\bar{l}''_B$ obtainable by substitution of (1) and (6) into (7)

$$\bar{l}''_B = \frac{\Sigma l'(>\alpha) + \Sigma D_{b+B}}{N'_0} = \bar{l}' + \overline{D_{b+B}} = \frac{1}{g}\cdot\exp[g\cdot(D+\alpha)] \tag{7}$$

The measurement of $\bar{l}''_B$ and the use of (7) is an alternative solution to determine ionization.

Consequently, the density of the intervals larger than α and that of the blob + bubbles modify, taking the value

$$n_B = \frac{N'_0}{\Sigma l'(>\alpha) + \Sigma D_{b+B}} = g \cdot \exp\left[- g \cdot (D + \alpha)\right] \tag{8}$$

The results of the calculations are given in table 2 for the resolution α and $\alpha = 0$ when determining the boundaries of the bubbles.

TABEL 2

The parameters used to determine g when the blobs are measured

Parameters	Range of measurement			Experimental methods
	$-D \leqslant l' < \infty$	$0 \leqslant l' < \infty$	$D/2 = \alpha \leqslant l' < \infty$	
$\bar{l}''_B = \dfrac{L}{\int_{\alpha}^{\infty} n(l') \cdot dl'}$	$\dfrac{1}{g}$	$\dfrac{1}{g} \exp(gD)$	$\dfrac{1}{g} \exp\left[g(D+\alpha)\right]$	$\dfrac{\Sigma l'(>\alpha) + \Sigma D_{b+B}}{N'_0}$
$\nu_B = \dfrac{1}{L} \int_{\alpha}^{\infty} l' \cdot n(l') \cdot dl'$	$1 - Dg$	$\exp(-gD)$	$(1+\alpha g) \cdot \exp\left[-g(D+\alpha)\right]$	$\dfrac{\Sigma l'(>\alpha)}{\Sigma l''}$
$n_B = \dfrac{1}{L} \int_{\alpha}^{\infty} n(l') \cdot dl'$	g	$g \cdot \exp(-gD)$	$g \cdot \exp\left[-g(D+\alpha)\right]$	$\dfrac{\text{gap number } l' > \alpha}{\Sigma l'_{,}}$

The case $\alpha = - D$ corresponds to an ideal resolution when the bubbles inside the blobs are also distinguishable; the resulted values agree with those in the second column of the tabel 1 when the blobs are eliminated.

Consequently, g can be determined (when blobs are taken into account) from the parameters $\bar{l}''_B$, ν_B, n_B, $\overline{D_{b+B}}$ but the only one independent is $\overline{D_{b+B}}$. The other parameters can be function of l' and $\overline{D_{b+B}}$ using the following relations:

$$\bar{l}''_B = \bar{l}' + \overline{D_{b+B}}; \quad \nu_B = \frac{\bar{l}'}{\bar{l}''_B} = \frac{\bar{l}'}{\bar{l}' + \overline{D_{b+B}}}; \quad n_B = \frac{1}{\bar{l}''_B} = \frac{1}{\bar{l}'_B + \overline{D_{b+B}}} \tag{9}$$

The parameters $\bar{l}'$ and $\overline{D_{b+B}}$ are independent because they refer to distinct ranges namely: $\bar{l}'$ to the gaps larger than α and $\overline{D_{b+B}}$ to the gaps

REFERENCES

A. Ahmadzadeh and N. N. Biswas, *Nuovo Cim.*, 19, 958 (1961).

M. Blau, S. C. Bloch, C. F. Carter and A. Perlmutter, *Rev. Sci. Instr.*, **31**, 289, (1960).

C. Dilworth, D. R. O. Morrison and G. Mambriani, *Nuovo Cimento*, **32**, **1432**, (1964).

G. A. Blinov, I. S. Kresinikov and M. F. Lomanov, *J. Exp. i Teoret. Fiz.*, *31*, 762 (1956).

M. F. Lomanov and B. V. Cirikov, *Priborî i Tehn. Exper.*, (1957), 22, nr. 5

W. H. Barkas, *Phys. Rev.*, *124*, 897 (1961).

R. L. Gluckstern, *Nuclear Instr. Methods*, *45*, 166, (1966).

W. H. Barkas, *Rev. Sci. Instr.*, *38*, 425 (1967).

J. Gezelter, *Nuclear Instr. Methods*, *73*, 109, (1969).

G. Yekutieli, *R.* Yaffe and S. Toaff, *Nuclear Instr. Methods*, *67*, 305, (1969).

APESTI MŰSZAKI EGYET
KÖZPONTI
1848

RELAXOMETRU DE REZONANȚA MAGNETICĂ NUCLEARĂ

ȘT. LEVAI și D. BORȘAN

Metodele nestaționare de detectare a semnalelor de *RMN* au condus la cele mai exacte determinări ale timpilor de relaxare magnetică și a coeficientului de difuzie ale nucleelor. Aceste măsurători se realizează cu ajutorul relaxometrelor de *RMN* în impulsuri. În cele ce urmează vom descrie un asemenea relaxometru, realizat de autori la facultatea de Fizică a Univ. București.

La baza funcționării relaxometrului de *RMN* în impulsuri stă fenomenul de spin ecou [1] care, în principiu, constă în următoarele: un circuit oscilant, în bobina căruia se află proba de studiat, este introdus într-un cîmp magnetic H_0. La circuit este trimisă o anumită succesiune de impulsuri, a căror frecvență de umplere este egală cu frecvența de rezonanță a nucleelor în cîmpul magnetic H_0. După impulsuri și între impulsuri în bonina circuitului oscilant sînt induse semnalele inducției nucleare care amplificate pot fi observate pe ecranul unui oscilograf.

Amplitudinea și forma semnalelor de rezonanță nucleară depind de parametrii impulsurilor folosite, de succesiunea de impulsuri, de timpii de relaxare ale nucleelor (T_1 și T_2) și de neomogenitatea cîmpului magnetic. Pentru ca semnalele de spin ecou să ia naștere durata și amplitudinea impulsurilor folosite trebuie să îndeplinească condițiile

$$t_i \ll T_2, \quad \frac{1}{\gamma \Delta H_0}$$

$$\gamma H_1 t_i = \theta,$$

unde θ este unghiul sub care este răsucit vectorul macroscopic de magnetizare $\vec{M}$ în urma acțiunii impulsului de durată t_i și de amplitudine H_1, ΔH_0 — neomogenitarea cîmpului magnetic H_0 în limitele eșantionului. Măsurarea timpilor de relaxare și a coeficientului de difuzie se face cel mai rapid folosind anumite succesiuni de impulsuri de 90° $\left(\theta = \frac{\pi}{2}\right)$ și de 180° $(\theta = \pi)$.

În prezent cele mai folosite succesiuni de impulsuri sînt [2, 3]:

pentru T_1,

$$90° - \tau - 90°;\quad 180° - \tau - 90°;$$

$$90° - \tau_1 - (90° - \tau_0 - 180° - \tau_0 - 90°) - \tau_2 - ...,$$

pentru T_2,

$$90° - \tau - 180°;\quad 90° - \tau - 180° - 2\tau - 180° - 2\tau - ...$$

Descrierea instalaţiei

Relaxometrul *RMN* conţine trei părţi de bază şi anume: blocul de programare, modulatorul şi linia de amplificare. Schema bloc a relaxometrului este redată în fig. 1.

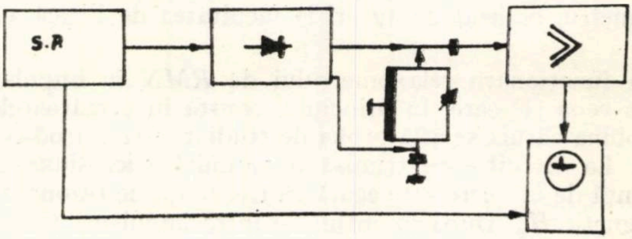

Fig. 1

Electromagnetul folosit este de tip Weiss. Alimentarea lui se face de la o baterie de acumulatori de 120 V. Stabilizarea curentului de alimentare este asigurată de un stabilizator tranzistorizat care dă o stabilizare a curentului de 10^{-5}. Observarea semnalelor de ecou se face pe un oscilograf sincronizat de la blocul de programare.

Blocul de programare are posibilitatea de a programa impulsuri dreptunghiulare de durată variabilă, între limitele 2 şi 20μs, de polaritate pozitivă sau negativă. Schema poate prelucra oricare din seriile de perechi de impulsuri [3]

$$\frac{\pi}{2} - \tau - \frac{\pi}{2};\quad \pi - \tau - \frac{\pi}{2}\quad \text{şi}\quad \frac{\pi}{2} - \tau - \pi,$$

cu timpul τ variabil între limitele 100μs — 1s. Intervalul de timp după care seria de impulsuri se repetă este de asemenea variabil şi este cuprins între 0,1 şi 10 s. Pentru a exclude influenţa autodifuziei asupra valorii lui T_2

schema de programare poate prelucra seria de impulsuri $\frac{\pi}{2} - \tau - \pi - 2\tau - - \pi - 2\tau - \pi \ldots$ avînd același timp de repetare. Schema de realizare a acestui bloc este redată în figura 2.

Pentru a înțelege modul de funcționare al schemei vom descrie obținerea unei perechi de impulsuri. Comutatorul K_1 se află în poziția 1. În acest caz

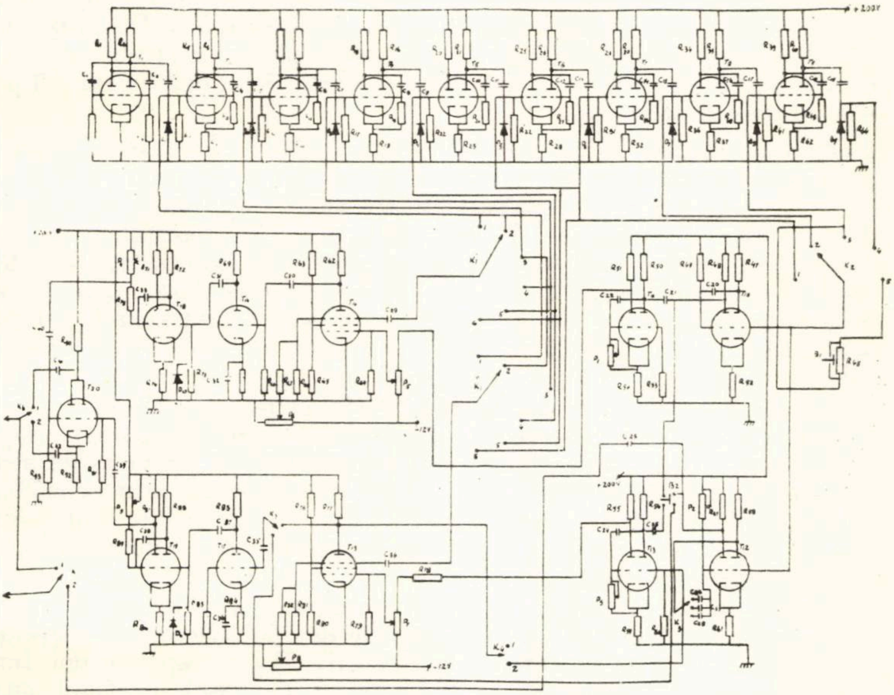

Fig. 2

impulsurile de la multivibratorul T_1, după diferențiere și limitare, ajung la etajele de coincidență T_{14} și T_{15} cu frecvența de 180 Hz. Tot de la multivibrator impulsurile sînt trimise la linia de divizare $T_2, \ldots, T_9$. Primele etaje $T_2, \ldots, T_6$ (6N2P) au raportul de divizare 2 iar ultimele $T_7 - T_9$ au pentru acest raport valoarea 4, 5, 5. Cu ajutorul comutatorului K_2 se alege intervalul dintre două serii de impulsuri. Prin acest comutator impulsurile rare sînt aplicate la grilele de comandă ale etajelor de întîrziere T_{10} și T_{12} (6N1P) care sînt deschise în același timp. Durata impulsurilor prelucrate de prima întîrziere T_{10} este fixă și egală cu 3 ms iar durata impulsurilor prelucrate de T_{12} este variabilă (potențiometrul P_1). Impulsul prelucrat de T_{10} se aplică etajului T_{11} care prelucrează un impuls dreptunghiular de durată variabilă, pozitiv. Acest impuls se aplică etajului de coincidență T_{14} la care sosesc şi impulsuri scurte, pozitive de la T_1. Coincidenţa T_{14} prelucrează un impuls negativ numai în momentul în care lampa este deschisă simultan de către cele două impulsuri. De aici impulsul este trimis la etajul de scurtare T_{16} apoi la generatorul T_{18} şi de aici la etajul de ieşire T_{20} care este un repetor catodic sau anodic. În felul acesta s-a realizat primul impuls de 90° sau de 180° după cum este fixată durata impulsului la generatorul T_{18}. Al doilea impuls din serie se realizează prin trimiterea impulsului prelucrat de T_{12} la schema de scurtare T_{17}. Impulsul format aici comandă cel de-al doilea generator T_{19} de unde impulsul este trimis la etajul final T_{20}. Distanţa dintre aceste două impulsuri se stabileşte cu ajutorul potenţiometrului P_2, de la întîrzierea T_{13}. În funcţie de poziţia comutatorului K_2, după un timp θ perechea de impulsuri se va repeta.

Obţinerea seriei $90° - \tau - 180° - 2\tau - 180° - 2\tau - 180°$. Comutatorul K_1 se pune într-una din poziţiile 2, 3, 4, 5 sau 6. În acest fel la coincidenţele T_{14}, T_{15} vor sosi impulsuri de frecvenţe 160, 80, 40, 20 respectiv 80, 40, 20, 10 Hz. Comutatorul K_2 se pune într-una din poziţiile 1, 2, 3, 4, 5 care determină intervalul dintre seriile de impulsuri. Impulsurile rare de la K_2 deschid cele două întîrzieri T_{10} şi T_{12}. Etajele selectoare T_{11} şi T_{13} sînt deschise de impulsul venit de la T_{10} (T_{12} este deconectată prin B_2). Impulsurile pozitive de la cele două selectoare se aplică la grilele de comandă ale etajelor de coincidenţă. La grilele supresoare se aplică şi impulsurile de la K_1 de frecvenţe 160 — 20 respectiv 80—10 *Hz*. Durata impulsului prelucrat de T_{11} este astfel aleasă încît acesta să permită trecerea unui singur impuls prin coincidenţa T_{14}. Durata impulsului prelucrat de T_{13} este astfel aleasă încît acesta să permită trecerea cîtorva impulsuri (serie) prin coincidenţa T_{15}. Impulsurile negative, ascuţite, prelucrate de coincidenţe sînt trimise la etajele de scurtare iar de aici la cele două generatoare. Generatoarele prelucrează impulsuri dreptunghiulare de durată variabilă. Aceasta se alege în aşa fel încît impulsul prelucrat de primul generator T_{18} să fie de 90° iar cele prelucrate de generatorul al doilea T_{19} să fie de 180°. Deoarece frecvenţele impulsurilor sosite la coincidenţele T_{14} respectiv T_{15} au raportul doi, intervalul dintre impulsul prelucrat de coincidenţa T_{14} (90°) şi primul impuls din seria de impulsuri prelucrată de coincidenţa a doua T_{15} (180°) va fi de $1/f$. Intervalul dintre impulsurile seriei prelucrată de coincidenţa T_{15} va fi de $2/f$ adică tocmai seria propusă.

Blocul modulator are ca scop transformarea video-impulsurilor sosite de la blocul de programare în impulsuri de radiofrecvenţă. Frecvenţa de lucru este de 19 MHz. Schema de realizare a modulatorului este redată în fig. 3.

Tupurile T_1 şi T_2 (6*NIP* şi 6*J*4*P*) formează un generator cu excitaţie în şoc. T_3 este etaj preamplificator iar T_4 etaj amplificator de putere. Sarcina tubului T_5 este un circuit oscilant. În interiorul bobinei acestui circuit se introduce substanţa de studiat. Impulsurile de *RF* prelucrate de acest bloc permit obţinerea unui impuls de 90° pentru o durată de 7μs a impulsurilor prelucrate de blocul de programare.

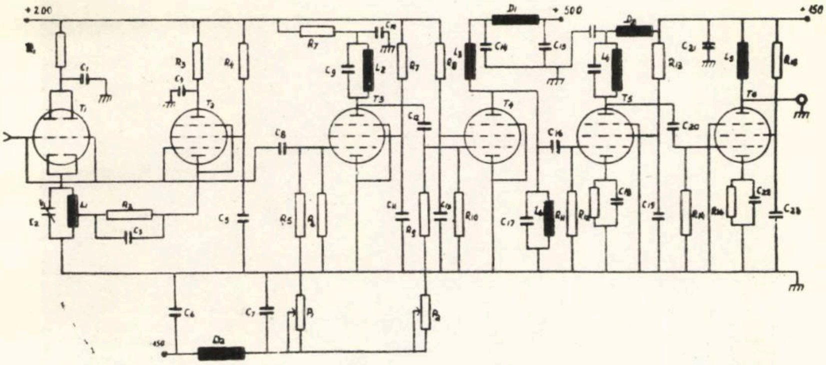
+200
T₁
C₁
C₂
L₁
R₂
C₃
R₃
T₂
R₄
C₅
C₆
C₇
C₈
R₅
R₇
C₉
L₂
T₃
P₁
P₂
D₃
D₁
+500
L₃
C₁₄
C₁₅
T₄
C₁₆
C₁₇
D₂
L₄
T₅
C₁₈
C₁₉
C₂₀
R₁₃
C₂₁
L₅
T₆
R₁₆
C₂₂
C₂₃
+150

Fig. 3

Linia de amplificare constă din două părți: Un preamplificator (fig. 3), tuburile T_5 și T_6, montate direct în blocul de modulare și amplificatorul principal, fig. 4.

Tubul T_1 realizează o heterodinare iar tuburile T_2, T_3 și T_4 (6J9P) lucrează pe frecvența intermediară de 4,5 MHz. Detectarea semnalelor se face cu dioda *D2B*. Linia de amplificare are coeficientul de amplificare de 10^5.

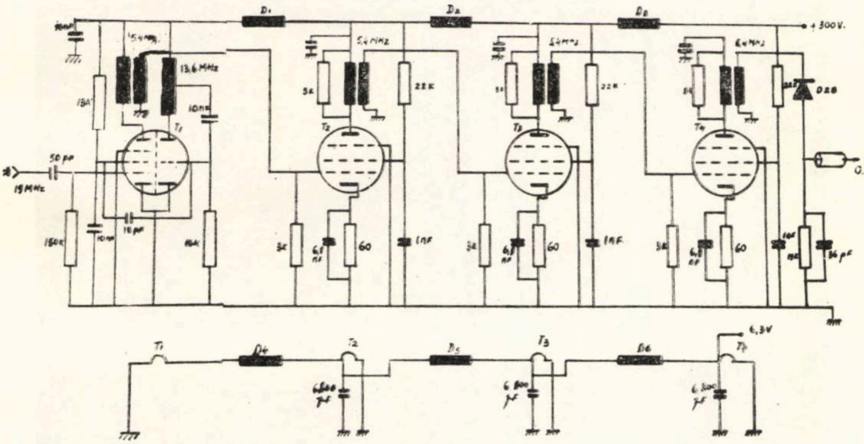
D₁
D₂
D₃
+300V.
13,6 MHz
50 pF
19 MHz
150K
10 pF
T₁
T₂
T₃
T₄
22K
3K
60
1nF
D2B
O.C
36 pF
D4
D5
D6
6,3V
6800 pF

Fig. 4

În figurile ce urmează sînt exemplificate cîteva din posibilitățile aparatului pentru determinarea timpilor de relaxare T_1 și T_2. Substanța pe care s-a lucrat în acest caz a fost o soluție de sulfat de cupru. În fig. 5, *a* este fotografiat un semnal de spin ecou. Fig. 5, *b* ilustrează posibilitatea de-a deter-

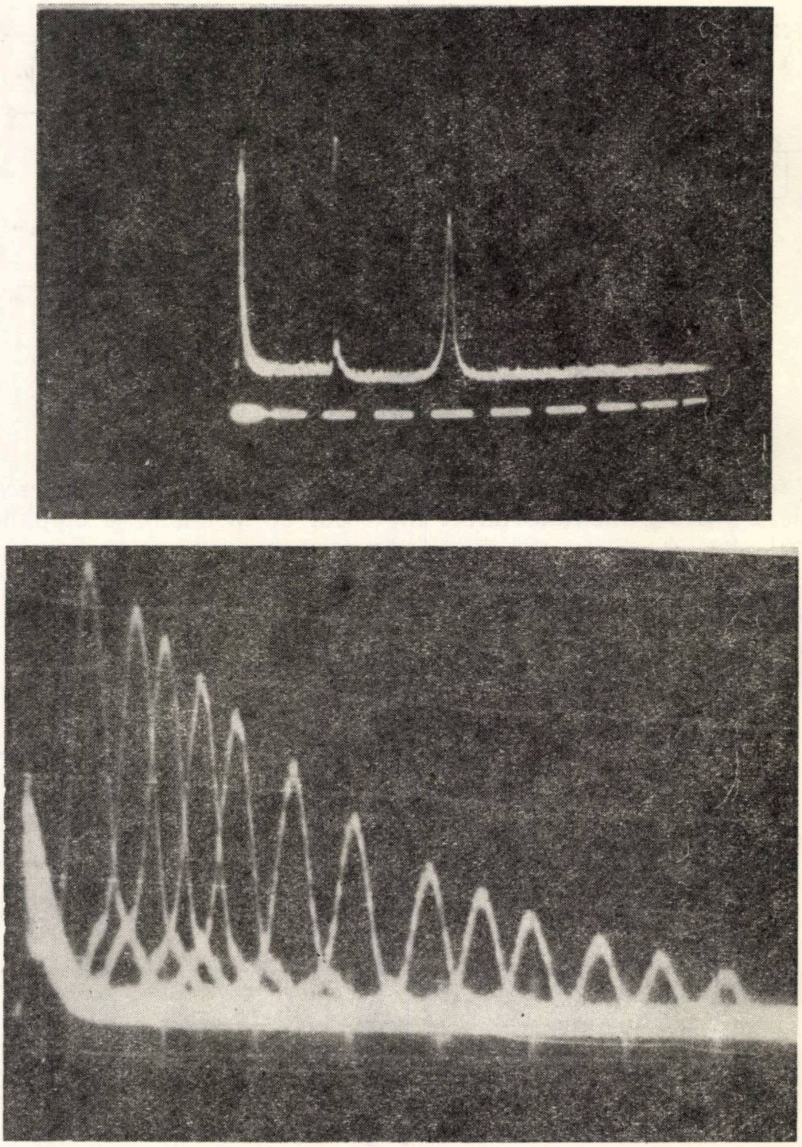

Fig. 5 *a*, *b*

mina pe T_2 folosind seria de impulsuri 90° — τ (variabil) — 180°, sincronizarea oscilografului este realizată cu impulsul al doilea. Tot pentru determinarea lui T_2 (pentru a exclude influenţa autodifuziei) se poate folosi seria 90° — τ — 180° — 2τ — 180° — ... fig. 5, *c*. Timpul T_1 poate fi determinat folosind seria de impulsuri 180° — τ (variabil) — 90°, fig. 5,*d*.

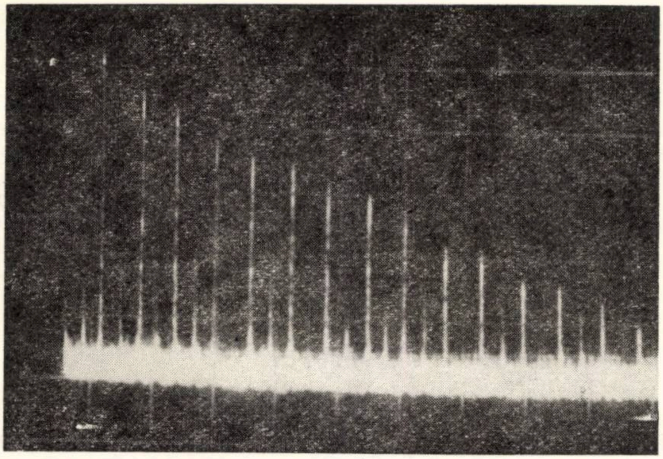

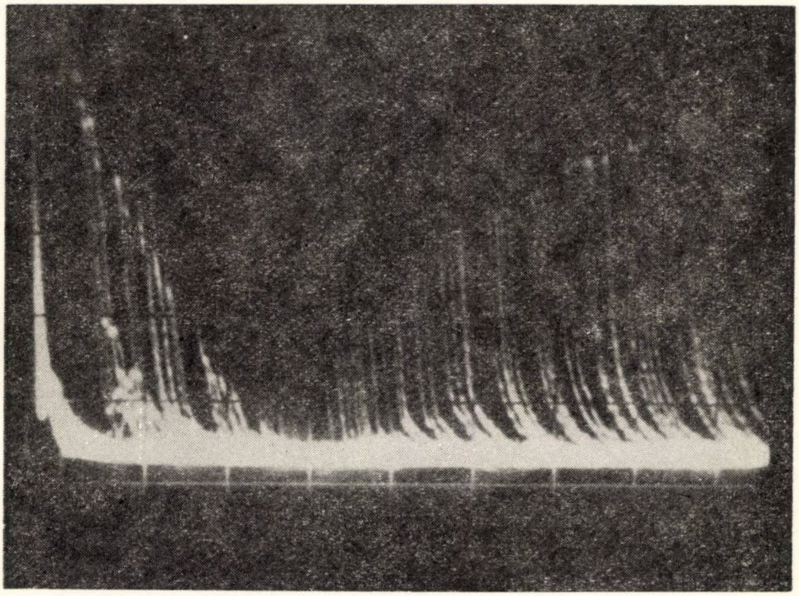

Fig. 5 *c*, *d*

BIBLIOGRAFIE

1. E. L. Hahn, Phys. Rev. 80, 580, 1950.
2. H. Y. Carr, E. M. Purcell, Phys. Rev. 94, 630, 1954.
3. V. I. Cijik, Vestnic L.G.U. Nr. 22, 64, 1961.

ЯМР РЕЛАКСОМЕТР

Краткое содержание

В работе описан релаксcметр ЯМР построенный на физическом факультете Бухарестского Университета. Релаксометром можно измерять времена реласкcации спин — спин T_2, спин — решетоъное T_1 а также коэффициент дифузий в жидкостях.

Прибор работает на частоте 19 Мгц для протонов. Для измерения времен релаксаций используются разные комбинации паров импульсов а также серии импульсов.

MNR RELAXOMETER

Abstract

This paper presents a *MNR* relaxometer deviced and constructed at the Departamente of Physics of the University of Bucharest. It is adapted for the T_1 and T_2 relaxation times and diffusion coefficient measurements for liquids. The work frequence for protons is 19 MHz. The scheme can give either various pair combinations or seria of pulses.

Facultatea de Fizică, Universitatea Bucureşti

PARAMETERS STANDARD ERRORS OF LORENTZ AND GAUSS FORM SPECTRA

C. I. NISTOR and, A. E. DRUKER

Spectral parameters are determined either with the help of electronic computers, which sometimes give also the values of the standard errors (1) or graphically. This work supplies the simple formulae obtained by as,that allow to determine the parameter standard errors of the Lorentz and Gauss form non superposed resonances.

These formulae are useful when the electronic computing method does not supply the standard errors or when the parameters are graphicaly determined. and also in study of relative efficience of different experimental arangements (for example; the determination of optimum width of absorbers in Mössbauer experiments (2). In the end of the present work there is an aplication of the optained formulae for determination of optimum width of a chennal for detection in γ — ray spectrometry in general (in particular) for Mössbauer spectrometry).

The method of the least squares (2, 3) enables to determine parameters $\alpha_i (i = 1, 2, ..., n)$ a spectrum of the form:

$$f(x, \alpha_1, \alpha_2, ..., \alpha_n) \equiv f(x; \vec{\alpha})$$

by minimizing expression

$$\chi^2 = \sum_{i=1}^{N} [f(x_i; \vec{\alpha}) - y_i]^2 P(y_i) \tag{1}$$

where

$\{y_i\}_{(i=1,2,...N)}$ is the set of experimental values for points x_i of variable x which supposed to be unaffected by errors; $P(y_i) = (\sigma y_i)^{-2}$ is the statistic weight of experimental result y_i, while σy_i is the standard error of the y_i measuring.

The minimum condition become then

$$\sum_{p=1}^{n} \mathrm{F}_{lp}(\vec{\alpha}^\circ)\Delta\alpha_p = F_l(\vec{\alpha}^\circ); \qquad (l = 1, 2, ..., n) \tag{2}$$

where

$$F_{lp}(\vec{\alpha}^{\circ}) = \sum_{i=1}^{N} (\partial f(x_i , \vec{\alpha}) / \partial \alpha_l)_{\vec{\alpha}^{\circ}} (\partial f(x_i, \vec{\alpha}) / \partial_p)_{\vec{\alpha}^{\circ}} P(y_i) \tag{3}$$

$$F_l(\vec{\alpha}^{\circ}) = \sum_{i=1}^{N} [f(x_i, \vec{\alpha}) - y_i] (\partial f(x_i, \vec{\alpha}) / \partial \alpha_l)_{\vec{\alpha}^{\circ}} \mathrm{P}(y_i) \tag{4}$$

and where $\Delta\alpha_p = \alpha_p - \alpha_p^0$ expresses the correction of initial parameters $\alpha_p^0 (p = 1, 2, ..., n)$.
used the error matrix $F^{(-1)}$ that, for the mean square deviation $\sigma\alpha_p$ gives (3, 4):

$$\sigma\alpha_p = [F_{pp}^{(-1)}(\vec{\alpha})]^{1/2} \tag{5}$$

where $F_{pp}^{(-1)}(\vec{\alpha})$ is the pp element of the inverted of$(F_{lp}(\vec{\alpha}))$ matrix, as considered for its most probable values α_p.

For parameters error calculation (5) of Lorentz — f_L and f_G — Gauss resonance situated on an N_F constant ground, we took:

$$\begin{aligned} f_L(x_i, x_0, \Gamma, \varepsilon_0) &= N_F \{\varepsilon_0 \Gamma^2 / [\Gamma^2 + 4(x_i - x_0)^2] + 1\} = \\ &= h\Gamma^2 / [\Gamma^2 + 4(x_i - x_0)^2] + N_F \end{aligned} \tag{6}$$

$$\begin{aligned} f_G(x_i, x_0, \Gamma, \varepsilon_0) &= N_F [\varepsilon_0 \exp \{- 4(x_i - x_0)^2 \ln 2 / \Gamma^2\} + 1] = \\ &= h \exp \{ - 4(x_i - x_0)^2 \ln 2 / \Gamma^2\} + N_F \end{aligned} \tag{7}$$

where x_0 represents the resonance position, Γ is resonance width at its half-height, ε_0 the relative value of the resonance in regard to the ground and h represents the resonance amplitude.

The following hypotheses and approximations were made:

1. $x_{i+1} - x_i =$ constant

2. (8) $P(y_i) = (\sigma y_i)^{-1} = [f(x_i ; \vec{\alpha})]^{-1}$

valid in the case when y_l is a number of indepndent events (such as nuclear processes), with

$$\sigma y_i = [f(x_i ; \vec{\alpha})]^{1/2}$$

3. The sums were approximated, with the help of the average theorem by means of integrals;

4. x_0 is placed within the integration interval, whose extend is at least 4 times larger than Γ.

In order to obtain the simplest possible formulae, we took into consideration either $|\varepsilon_0| \ll 1$ or $|\varepsilon_0| \gg 1$, while for the Lorentzian we considered also $|\varepsilon_0| = 1$; the results are to be found in table 1. where N_0 is the experimental points number coresponding to Γ width.

TABLE 1

Standard errors of a resonance parameters: x_0 is the position; Γ the width at the half-height; ε_0 is the relative amplitude and h the amplitude, as a function of N — the number of experimental points on Γ and on of N — the number of ground impulses.

F	Approx.	σx_0	$\sigma\Gamma$	$\sigma\varepsilon_0$	σh_0
L	$\lvert\varepsilon_0\rvert < 1$	$\frac{0.798 \cdot \Gamma}{\lvert\varepsilon_0\rvert \sqrt{N_0 N_F}}$	$\frac{2.258 \cdot \Gamma}{\lvert\varepsilon_0\rvert \sqrt{N_0 N_F}}$	$\frac{1.594}{\sqrt{N_0 \cdot N_F}}$	$1.594 \cdot \sqrt{\frac{N_F}{N_0}}$
	$\varepsilon_0 \simeq 1$	$\frac{1.013 \cdot \Gamma}{\lvert\varepsilon_0\rvert \cdot \sqrt{N_0 N_F}}$	$\frac{2.714 \cdot \Gamma}{\lvert\varepsilon_0\rvert \sqrt{N_0 N_F}}$	$\frac{2.155}{\sqrt{N_0 \cdot N_F}}$	$2.155 \cdot \sqrt{\frac{N_F}{N_0}}$
	$\lvert\varepsilon_0\rvert > 1$	$\frac{0.564 \cdot \Gamma}{\sqrt{\lvert\varepsilon_0\rvert \cdot N_0 \cdot N_F}}$	$\frac{1.130 \cdot \Gamma}{\sqrt{\lvert\varepsilon_0\rvert N_0 \cdot N_F}}$	$1.383 \sqrt{\frac{\lvert\varepsilon_0\rvert}{N_0 N_F}}$	$1.383 \sqrt{\frac{\lvert h_0\rvert}{N_0}}$
G	$\lvert\varepsilon_0\rvert < 1$	$\frac{0.691\, \Gamma}{\lvert\varepsilon_0\rvert \sqrt{N_0 N_F}}$	$\frac{1.633 \cdot \Gamma}{\lvert\varepsilon_0\rvert \sqrt{N_0 \cdot N_F}}$	$\frac{1.412}{\sqrt{N_0 N_F}}$	$1.412 \sqrt{\frac{N_F}{N_0}}$
	$\lvert\varepsilon_0\rvert > 1$	$\frac{0.336 \cdot \Gamma}{\sqrt{\lvert\varepsilon_0\rvert N_0 \cdot N_F}}$	$\frac{0.560 \cdot \Gamma}{\sqrt{\lvert\varepsilon_0\rvert N_0 N_F}}$	$0.973 \sqrt{\frac{\lvert\varepsilon_0\rvert}{N_0 N_F}}$	$0.973 \sqrt{\frac{\lvert h_0\rvert}{N_0}}$

In the work (5), where was obtained the formulae forming the first line of this table, we found for the Mössbauer spectrum a quite good concordance between the values calculated by these formulae and those given by a computer, which proves the accuracy of method.

In order to compare the standard errors thus obtained with the errors introduced by graphic plotting, we procceded at a working test with 40 distinct persons, concerning the values $\{y_i\}$ of a Mössbauer spectrum, also supplied by an electronic computer (5). The results are recorded in table 2, where $\overline{[(\Delta_p/\sigma\alpha_p)^2]}^{1/2}$ is the mean square value of the ratio between the deviation of parameter α_p value, graphically determined, from the computer determined value and the standard statistical deviation $\sigma\alpha_p$ supplied by the computer or by the above mentioned formulae.

TABLE 2

The quadratic mean of the ratio between the subjective error and standard error in a spectum treatment, with $\varepsilon_0 = 0.125$ and $N_0 = 3$.

α_p	x_0	Γ	ε_0
$\overline{(\Delta\alpha_p/\sigma\alpha_p)^2}]^{1/2}$	0.719	0.774	0.780

It is supposed that $[\overline{(\Delta\alpha_p/\sigma\alpha_p)^2}]^{1/2}$ increase with $\varepsilon_0/\sigma\varepsilon_0$; here we have $\varepsilon_0/\sigma\varepsilon_0 \simeq 12$.

The results thus obtained are equally valid when y_i is not number of independent events, by substituting, in the above formulae, $\sqrt{N_F}$ to $|\varepsilon_0| < 1$ or $\varepsilon_0 = 1$, and $\sqrt{|\varepsilon_0| N_F}$ to $|\varepsilon_0| > 1$, with the standard errors of peak measurements.

Making use of the above results, will enable us to determine the optimum width of the detection channel in some cases of nuclear experiments. So as to define more concretely the notions involved here we shall refer to the Mössbauer effect.

The experiment efficiency η is defined as the inverse of the measuring time, necesary to obtain the same parameters with a given error:

$$\eta = \frac{1}{T}$$

Since this measuring time is closely related to a given error, we endeavour to establish the dependance of the efficiency on the width of the detection channel in this relation.

Table 1. shows that the standard deviation of parameters x_0 — position and Γ — width, for $|\varepsilon_0| \lesssim 1$, as inversely proportional to $\varepsilon_0 \sqrt{N_F}$. As the detection channel growth larges, the intensity of the recorded quanta γ increases, as therefore does N_F, while on the other hand effect — ε_0 — decreases, since ratio $\varkappa$ between the number of the energy under study quanta γ and the total number of the recorded quanta in the channel (including the background) is also decreasing (fig. 1).

Consequently, in the case of a given γ detection equipment and of a given energetic line to be recorded, it is found that there exists a certain optimum detection with of the single channel analyser which depends on the ratio between the peak height and the background height.

The measuring time, for $|\varepsilon_0| \lesssim 1$, as deduced from $\sigma x_0 |2|$, is

$$\eta = \frac{1}{T} \sim \varepsilon_0^2 N_F \sim \varkappa^2 (S_r + S_F) \tag{9}$$

where:

$$\varkappa \equiv S_r/(S_r + S_F)$$

$$S_F \equiv I_F \Delta E$$

$$S_r \equiv I_r(E_0) \int_{E - E\Delta/2_0}^{E_0 + \frac{\Delta E}{2}} e\text{xp} \left\{ - \left(\frac{2}{G}\right)^2 (E - E_0)^2 \ln 2 \right\} \mathrm{d}E$$

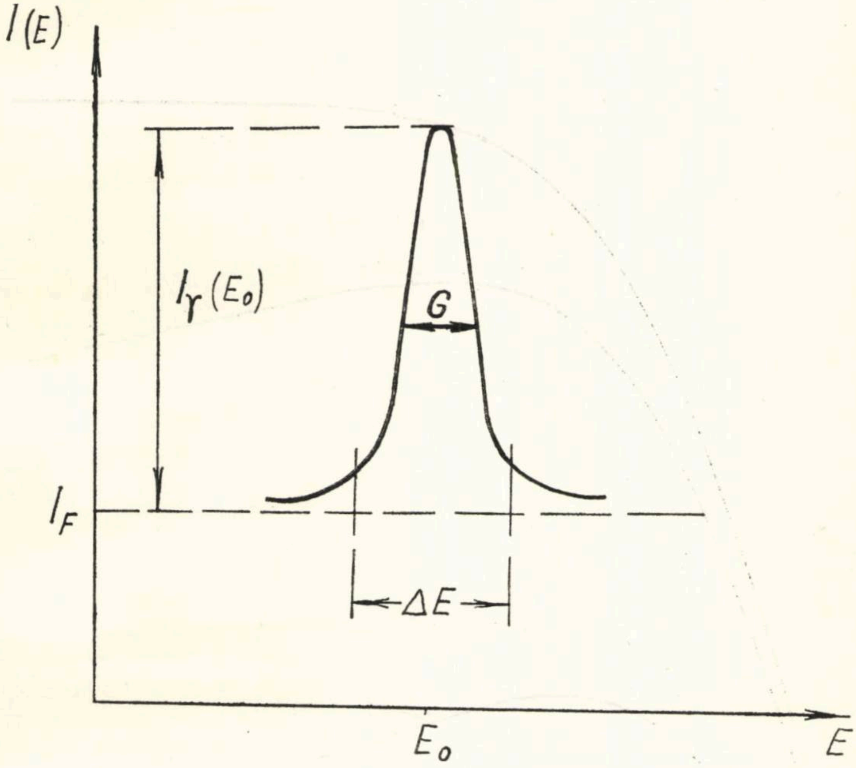

Fig. 1

I_F — being the background intensity supposed to be constant in the domain of the peak;

$I_r(E_0)$ — being the peak intensity of the energy under study;

ΔE — being the window width of the single channel analyser, centered on E_0;

G — being the width of Gaussian peak of spectrum.

We shall make use of the dimensionless quantities: $\xi = \Delta E / G$ and

$$\varkappa_0 = \lim_{\Delta E \to 0} \varkappa = \frac{I_r}{I_r + I_F}$$

Finally, the graph in figure 2 was obtained, where η^* is given by:

$$\eta(\xi, \varkappa_0) = K(\varkappa_0) \cdot \eta^*(\xi, \varkappa_0) = K_0 I_F \frac{\varkappa_0}{1 - \varkappa_0} \cdot \eta^*(\xi, \varkappa_0) \tag{10}$$

where K_0 is depending neither on ξ, nor on $\varkappa_0$.

Since we are interested in the optimum ζ's, we only represented here the values corresponding to $\varkappa_0 = 0, 1;\ 0, 5;\ 0{,}9;\ 1$

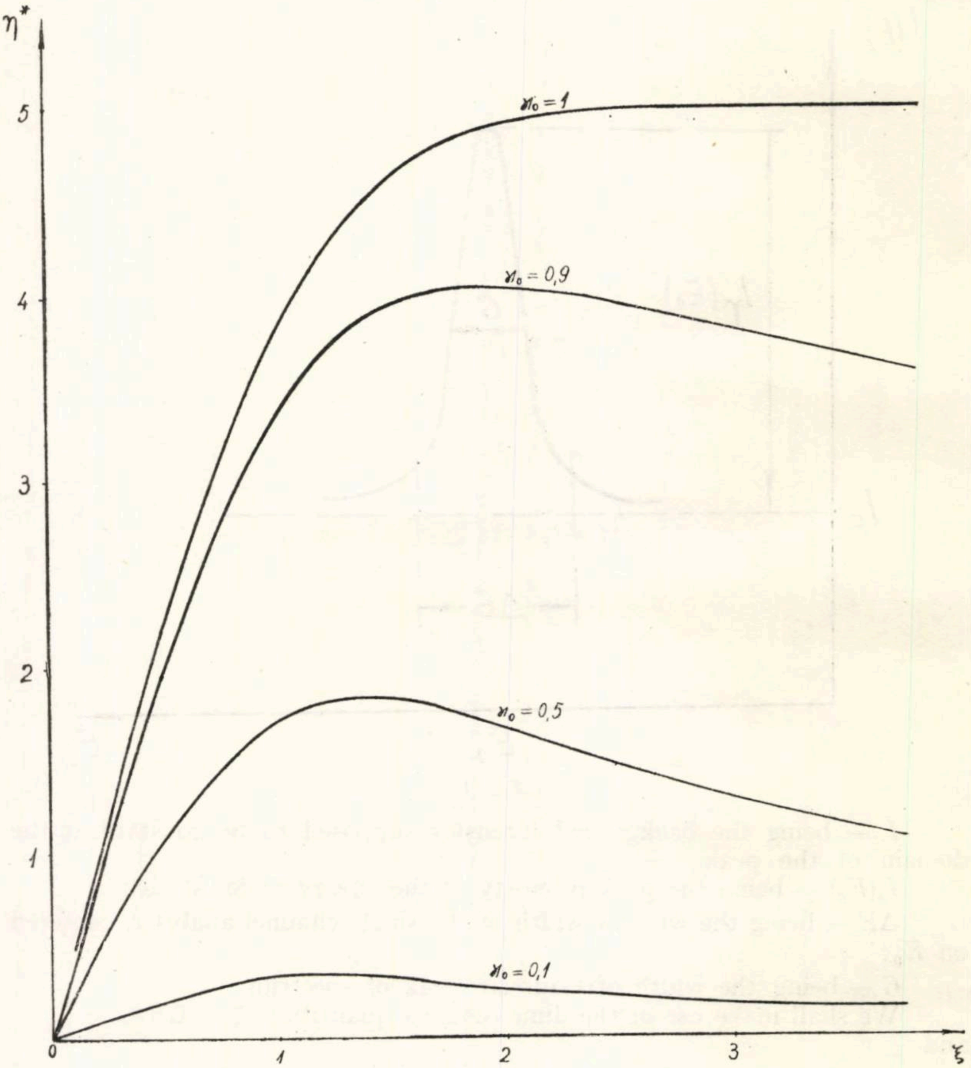

Fig. 2

From this graph, we can draw the conclusion that, since the maximum is not a sharp one, anyone of the values $\Delta E \in [G, 2G]$ can be considered optimum whichever x_0 may be. Therefore:

$$G \leqslant \Delta E \leqslant 2G \tag{11}$$

Up to now, we established the efficiency variation as a function of the channel width by means of:

$$\sigma x_0 = \sigma x_0(\eta, \xi) = \text{const} \tag{12}$$

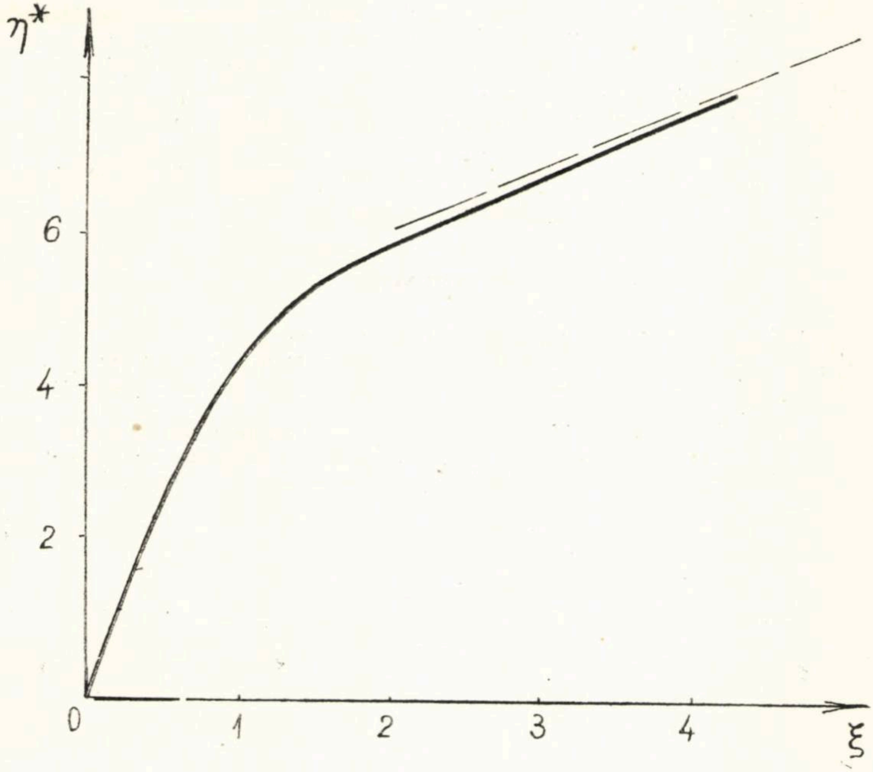

Fig. 3

or of

$$\sigma\Gamma = \sigma\Gamma(\eta,\ \xi) = \text{const} \tag{13}$$

for $|\varepsilon_0| \lesssim 1$. As a matter of fast, these are the only interesting cases, since to they only corresponds the optimum width. With the same parameters, but for $|\varepsilon_0| > 1$, any $\varkappa_0$ shall lead to a dependence similar to the preceding one for $\varkappa_0 = 1$.

Trying to determine the efficiency with the help of the standard deviation of the relative amplitude parameter:

$$\sigma\varepsilon_0 \equiv \sigma\varepsilon_0(\eta,\ \xi) = \text{const} \tag{14}$$

or of the amplitude parameter:

$$\sigma h_0 \equiv \sigma h_0(\eta,\ \xi) = \text{const} \tag{15}$$

we shall obtain a $\eta^*(\xi)$ variation of the form shown by figure 3. Where the asymptote, whose is always positive, changes its gradient concomitently with $\varkappa_0$.

The curves obtained for $|\varepsilon_0| > 1$ are similar, which means that there exists no other finite parameter ξ corresponding to the highest efficiency besides the above studies one, therefore that the optimum width can only by obtained by formulae (12) or (13).

Of course, these results allow for other discussions too.

Bucharest University, Faculty of Physics

REFERENCES

1. J. Duke, T. C. Gibb, J. Chem. Soc. (A) 1478 (1967)
2. Gavron, D. Kedem, T. Rothem, Nucl. Instr. Meth., *61* (1968) 213
3. E. Deming „Statistical Adjustement of Data" John Wiley and Sons (Inc.), New York, 1943
4. Nistor, C. Protop, G. Martin, Studii şi Cercetări de Fizică, *20* (1968) 117
5. Martin, C. Nistor, C. Protop, în „Colecţie de programe pentru Calculatorul Electronic CET-500" ed. Acad. Roum. Bucharest 1967 p. 408

PROGRAMS FOR THE ANALYSIS OF MOSSBAUER SPECTRES

C. NISTOR and C. LULEA

1 INTRODUCTION

In Mossbauer spectroscopy, the spectres consist in a superposition of absorbtion resonances on a ground, which is in general constant. The processing of the spectres consists in determining ist parameters and their standard errors, from which it is possible to determine the physical parameters.

The methods used for processing the spectres and the advantages of these methods are described in [1—7].

In this paper are described two programs made at the Computing Centre of the University of Bucharest, written in FORTRAN using an IBM 360/30 computer.

The first program named FITMOSSI was made to calibrate the spectrometer and it processes a Mossbauer spectre in which the positions of the resonances are known, and gives us the coefficients of the calibration polynom, which gives us the value of the speed, as a function of the number of detection channels from the spectre.

The second program, FITMOSS2 processes Mossbauer spectres, using the standard coefficients of the spectrometer and determines the physical parametres and their standard errors, for the spectres with at most three sets of six patterns of resonances, and the total spectre and its components.

The two programs use the Gauss-Newton method for determining by the iterative method the corrections to the initial values of the parameters, described in detail in [3, 4].

This method consists in transforming into a linear form, the analytical form of the function $F(I)$ of the spectre, using the parameters $Z(J)$ and with the condition that χ^2 (the sum of the squares of the deviation of $F(I)$ from the experimental spectre $AI(I)$, is to be minimum which leads us to a system of simultaneous linear equations; its solutions are the corrections of the initial values of the parameters. Then, the corrections are multiplied by a subunitar factor G, so chosen that χ^2 to be minimum, and the process is repeated for IT times. The standard errors of the parameters are represented by the square roots of the diagonal elements of the inverse matrix of this system.

2. THE PROGRAM FITMOSSI

The most wide-spread type of Mossbauer spectrometers are those in which the relative speed — source-absorbent varying linearly with time — is synchronized with a multichannel *analysor*, that is working in the *flying time* mode. For every spectrometer the deviation from the *linearity* is larger or smaller, remaining constant in time. To enlarge the precision of the determinations and to consider the relation between the positions of the resonances in the hyperfine splitting, we must know the dependence of the speed and the number of the detection channel.

For this purpose the program FITMOSS 1 was written, in which we take as input data the following:

— NS number of the spectre
— MN number of experimental points of the spectre
— N number of parameters
— IT number of iteratios
— $V(\mathrm{I}), \mathrm{I} = 1, 2, \ldots, 6$ the given positions of the experimental peaks in mm/S
— $Z(I), \mathrm{I} = 1, 2, \ldots, N$ the approximative parameters of the spectre
— $AI(I), \mathrm{I} = 1, 2, MN$ the experimental spectre

With the function subprogram FUNCI we determine the form of the spectre $F(I), \mathrm{I} = 1, 2, \ldots, MN$, using the parameters $Z(I), I = 1, \ldots, N$

Then the value of χ^2 was calculated where:

$$\chi^2 = \sum_{F=1}^{MN} \frac{(AI(\mathrm{I}) - F(\mathrm{I}))^2}{AI(I)\,(MN - N)} = \mathrm{P}H(L)$$

for every iteration and the numerical values for $\frac{\partial F(\mathrm{I})}{\partial Z(K)}$. which help us to determine the coefficients:

$$A(j,\ K),\ j = 1,\ N;\quad K = 1, N + 1$$

of the system, which we shall use to correct the initial values.

This system is solved with the Gauss method by chosing the pivot on the whole matrix, and we find the solution $V(I)$.

Then we calculate the $\mathrm{P}H(L, K)$ for $Z(\mathrm{I}) = Z(\mathrm{I}) + \frac{KX(I)}{2}$, where $K = 0, 1, 2$ and we determine a value for K, so that $\mathrm{P}H(\mathrm{I})$ to be minimum. All the computations are repeated as long as $L < IT$. As results, the computed spectre $F(I)$, the number of spectre NS, and the parameters $Z(I)$ from the last iteration are written.

Then we determine a polynom by the least-squares-method, using the points $(Z(I), V(I))$, $I = 1, 2, \ldots, 6$ and in this mode the coefficients $C(I)$ are computed.

3. THE SECOND PROGRAM FITMOSS 2

The second program FITMOSS2, decomposes the experimental spectre $AI(I)$ in three six-patterns. We tried to determine every six-pattern, using only the physical parameters. Thus, $Z(I)$ and $Z(2)$ are isomerical and quadrupolar shift, $Z(3)$ the magnetic field at nucleus in MO_e, $Z(4)$ and $Z(5)$ are width parameters, and $Z(6)$ the amplitude.

For the determining of the resonance parameters, we have put the following conditions, the widths and the amplitudes equal two by two, the areas of the peaks in the relation 3, 2, 1, 1, 2, 3, the positions of the peaks determined by $Z(1), Z(2)$ and $Z(3)$ and by the proportion $\mu_0/\mu_e = -1{,}73$.

The input data in this program are:

- NS number of the spectre
- MN number of the point on the spectre
- N number of parameters
- IT number of iterations
- $Z(I)$ — $(I = 1, 2, ..., N)$ the initial values of the parameters.
- $AI(\mathrm{I})$, $(\mathrm{I} = 1, 2, ..., MN)$ the points of the experimental spectre.
- NE the number of the calibration spectre
- $C(I)$ — $(I = 1, 2, 3, 4)$ the coefficients of the calibration polynom.
- P(I) the alphanumerical characters used to draw the spectre.

Using the independent parameters $Z(I)$, $(I = 1, ..., N)$, we calculate the components of the vector $U(J)$, $(J = 1, 2, ..., JS = 18)$ which represent the position, the widths and the amplitudes of the resonances. Using the coefficients of the calibration polynom, we calculate the components of the vector $V(I), I = 1, ..., MN$ the speeds corresponding to every experimental point of the spectre.

As in FITMOSS1, we must calculate the following values:

- $\partial \mathrm{P}H(L)/\partial Z(K),\ K = 1, 2, ..., N$
- $\mathrm{P}H(L) = \chi^2$ and
- $A(J, K), J = 1, ..., N, K = 1, ..., N + 1$

Then, with the same subprogram, we solve the system and the inverse matrix. The corrections are made as in FITMOSS1 and the processing continues as long as $L < IT$ and it is finished if $L = IT$ or if the maximum value of the proportion between the corrected and standard error, for all the parameters, is less than 0.25.

As results, are written the values of the parameters, of their standard error at every iteration, $PH(L)$, $(F(I), I = 1, ..., MN)$ the computed spectre, $(ES(J, I), J = 1, ..., JS,\ \mathrm{I} = 1, ..., MN)$ the separated spectres of the six-patterns, where JS is the number of the six-patterns; $(U(I), I = JP)$ the parameters of the resonances, where JP is equal to $18 = \mathrm{n}$, $\mathrm{n} =$ number of the six-patterns.

On the same graphic, are drawn the spectres $AI(I)$, $F(I)$ and $FS(J, I)$.

The program FITMOSS2, although it is made especially for the processing of Mössbauer spectres, obtained with Fe^{57} and in presence of the internal magnetic field, with three six-patterns and for the maximum 400 detection channels, it is very easy to modify it for another nucleus and for the spectres in which there is no magnetic splitting, by changing only a subroutine in the whole program. The number of the experimental points of the spectre may be enlarged.

University of Bucharest Dept. of Physics
University of Bucharest Computing Centre

REFERENCES

1. R. Gabriel and S. L. Ruby, Nucl. Instr. Methods, *36*, (1965), 23
2. R. Gabriel, în: Mossbauer effect methodology, vol. 1 ed. I. J. Gruverman (Plenum Press New York, 1965), p. 121
3. J. Duke, T. C. Gibb, J. Chem Soc. (A), (1967), 1478
4. Nistor, C. Proţop, şi G. Martin, St. Cerc. Fiz., Bucureşti, *20*, (1968), 117
5. H. Muir Jr., in Mossbauer effect methodology, vol. 4, ed. I. J. Gruverman (Plenum Press, New York, 1968), p. 75
6. Gavron, D. Kedem and T. Rothem, Nucl. Instr. Methods, *61* (1968) 213
7. F. Bent, B. I. Persson and D. G. Agresti, Computer Physics Comm. *1* (1969), 67

SUR LES PHÉNOMÈNES D'EXCITATION DANS UNE NOUVELLE SOURCE SPECTRALE KOROLEV

G. G. BRĂTESCU, I. IOVA, FLORIANA MOLDOVEANU
et HRISTINA CULICĂ

INTRODUCTION

L'influence des gaz étrangers sur les spectres des éléments chimiques, par exemple l'influence des gaz inertes sur l'intensité et la structure des raies spectrales de Hg, a presenté un grand intéret dans les laboratoires de specialité, spécialement après la découverte de l'effet laser dans le spectre du mercure pur (1) ou Hg + Ar (2).

Dans ce mémoire on étudie l'influence de *Kr* et *Xe* sur l'intensité et la structure de quelques raies spectrales de *Hg*, quand on réalise l'excitation du spectre dans une source spectrale Korolev (3).

Nous faisons ici une succinte remarque en ce qui concerne l'influence de la pression et de la nature du gaz étranger sur l'intensité des raies de *Hg* 3663,28 Å ($6^1D_2 - 7^3S_1$), 4046,56 Å ($6^3P_0 - 7^3S_1$) et 4358,35 Å ($6^3P_1 - 7^3S_1$) et sur la structure hyperfine des raies 4358,35 Å ($6^3P_1 - 7^3S_1$) et 5460,73 Å ($6^3P_1 - 7^3S_1$) de même élément.

LE DISPOSITIF EXPÉRIMENTAL

Le dispositif expérimental (représenté dans la figure 1) consiste d'une source spectrale I, Korolev, dont les phénomènes d'excitation on étudie là, un spectrographe Zeiss Q-24 utilisé comme monochromateur et d'un étalon Fabry-Perot à des plaques de quartz ayant la distance entre les surfaces intérieures de 3 mm, utilisé comme analiseur de raies, dans un montage en lumière convergente. Dans cette figure *D* représente un diaphragme, O_1 et O_2 sont des objectifs de projection et P.F. la plaque photographique du spectrographe.

La source spectrale realisée par les auteurs peut être examinée dans la figure 2 avec ses détails de construction.

Le tube de décharge électrique est construit en verre „razoterm" avec une fenêtre de quartz.

La décharge électrique employée comme source spectrale se produit entre la cathode *K* et l'anode *A* à une différence de potentiel $V = 1200$ *V*.

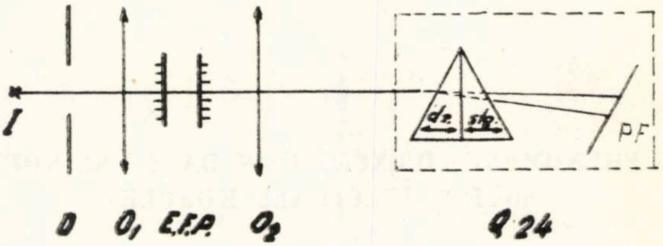

Fig. 1

Pour amorcer la décharge électrique à des faibles pressions il est nécessaire une décharge auxiliaire.

C'est pourça que dans la partie inférieure du tube on a encore introduit un électrode de wolfram *a* comme anode qui permet une décharge électrique entre le mercure qui se trouve à l'intérieur de la cavité P, et celui de son extérieur à une différence de potentiel $V = 120\ V$.

La plus parte de la vapeur du mercure évaporée de la cathode *K*, condensée dans l'étranglement inférieur du tub tombe dans la cavité inférieure. Seulement une petite parte de la vapeur passe dans le tube de décharge.

Grâce au refroidissement du tube à l'eau, la vapeur près de tube se condense et le flux de la vapeur devient un faiseau fin au long de l'axe centrale du tube.

Ainsi cette source spectrale présente d'une part quelques caractéristiques communes avec la source spectrale à faiseau atomique et d'autre part quelques caractéristiques communes avec l'arc électrique en vid. C'est pour ça que la finesse des raies spectrales obténues avec cette source este disposée entre les finesses des raies spectrales obténues avec les sources spectrales mentionnées.

Le tube a fonctioné à une installation de vide à 10^{-6} mmHg. La pression du gaz de travail (Kr ou Xe) a été mésurée à l'aide d'un manométre Mac-Leod.

RÉSULTATS EXPÉRIMENTAUX. DISCUSSIONS

Pendant le travail, le tube de décharge se trouve à une température pratiquement constante ($\approx 22°C$). Ça signifie que c'est le régime de la décharge électrique qui détermine la pression de la vapeur du mercure à l'interieur du tube.

Un premier group d'expériences effectué dans ce travail consiste en l'enregistrement du spectre de la décharge électrique à des diférentes pressions de Xe, tandis que les autres conditions restent invariables.

On constate que les intensités des raies spectrales du mercure considérées ici (λ 3663,28 Å, 4046,56 Å et 4358,35 Å) croissent en fonction de la

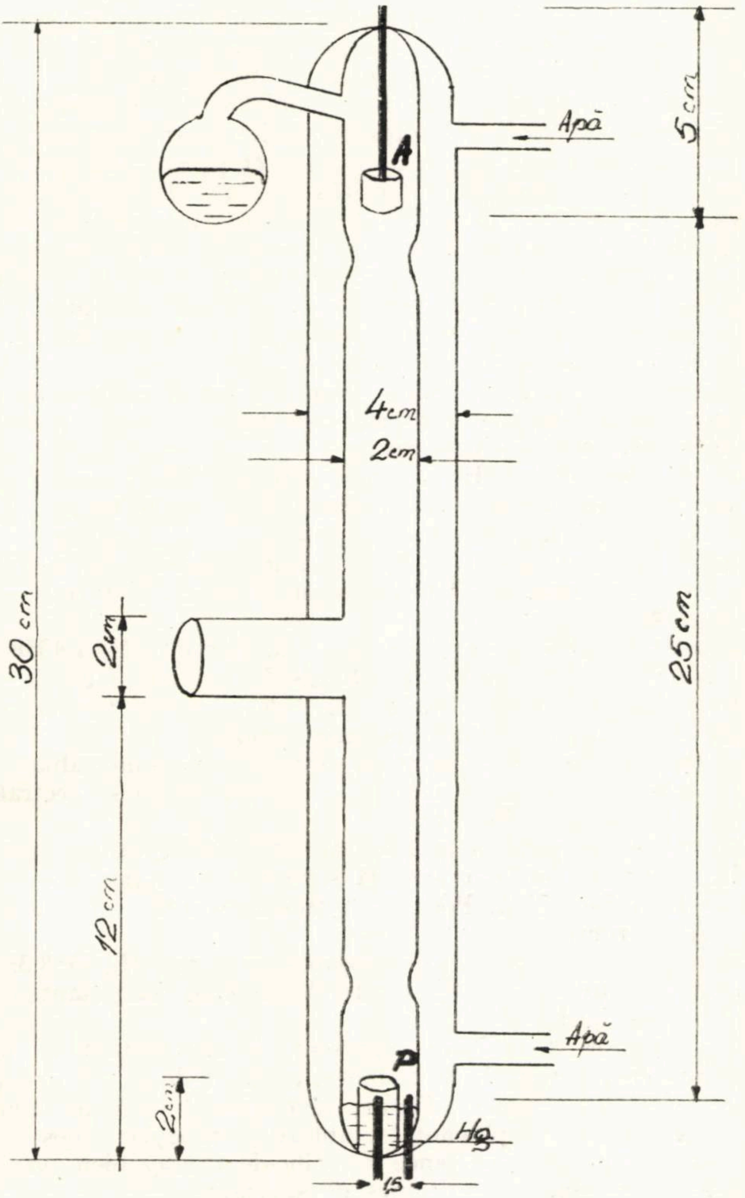
Apă
5cm
A
4cm
2cm
30 cm
2cm
25cm
12cm
2cm
P
Apă
Hg
1,5

Fig. 2

pression de Xe pour les valeurs $p = 0{,}05$ mm*Hg*, p = 0,4 mm Hg et $p = 2$ mm*Hg* (Fig. 3, *a*, *b*, *c*).

La raie Hg I λ 5460,73 A n'est pas mentionnée ici parce-que nous avons enregistré ces phénomènes sur les plaques spectrales ORWO-BLAU, insensibles pour le domaine spectrale où se trouve cette raie.

On constate aussi une évolution semblable des intensités des raies spectrale de *Hg*, en fonction de la pression de Kr, pour les valeurs $p_1 = 0{,}35$ mm Hg, $p_2 = 0{,}95$ mm Hg, $p_3 = 1{,}35$ mmHg et $p_4 = 2{,}5$ mm Hg.

Il faut remarquer que les intensités absolues des raies spectrales du mercure sont plus élevées dans le cas du mélange Hg + Kr que dans le cas du mélange Hg + Xe dans les conditions precisées. Evidemment, cette augmentation des intensités des raies spectrales du mercure ne se produit pas continuellement en fonction de la pression du gaz noble (krypton ou xénon). On connaît que les intensités des raies spectrales de cet élément présentent des maxima à des pressions bien définies (4), (5).

Une importante questions qui se pose ici c'est de trouver les pressions qui correspondent au spectres d'interférence d'optime clarté pour la structure des raies spectrales du mercure.

Ainsi pour le mélange Hg + Xe le spectre d'interférence du mercure d'optime clarté a été obtenu à la pression du xénon de 0,4 mm*Hg* et pour le mélange Hg + Kr à la pression du krypton $p = 0{,}95$ mm Hg.

La différence entre les intensités des raies spectrales du mercure excitées dans les deux conditions au dessus mentionées, peut être remarqué dans la figure 4.

Dans cette figure *a* désigne le spectre du mercure (Hg I 4358,35, Hg I 4046,56 et 3663,28 Å) enregistré dans le cas du mélange Hg +X e, et *b* le même spectre dans le cas du mélange Hg + Kr. Les spectres ont été enregistrés dans les mêmes conditions spectrographiques.

Pour obtenir une spectrogramme claire et photométrable, le temps de cinq minutes d'enregistrement sur les mêmes plaques spectrales, c'est entièrement satisfaisant (Fig. 5).

On constate que pour la pression de 0,95 mm*Hg* du krypton dans le mélange Hg + Kr, on obtient aussi la structure hyperfine des raies Hg I 4358,35 Å et Hg I 5460,73 Å. Pour les autres pressions c'est très difficile à distinguer cette structure.

La structure résolue a trois composants de la raie Hg 4358,35 Å,

on peut la voire dans la fig. 6, et celle de cinq composants de la raie Hg I 5460,73 dans la fig. 7.

Dans ces figures (6 et 7) on représente la distribution des intensités des composants en fonction de la distance, à partir de centre des anneaux.

Les valeurs des longuers d'onde, determinées pour les composants des ceux deux raies en employant le tableau rectangulaire des carrés des diametres des anneaux d'interférence [6] coincident assez bien avec les données des autres ouvrages scientifiques de spécialite (6).

C'est assez intéressant le fait que aucune pression de xénon dans le mélange Hg + *Xe* ne permet pas à bien résoudre la structure des raies spectrales indiqués dans les figures 6 et 7.

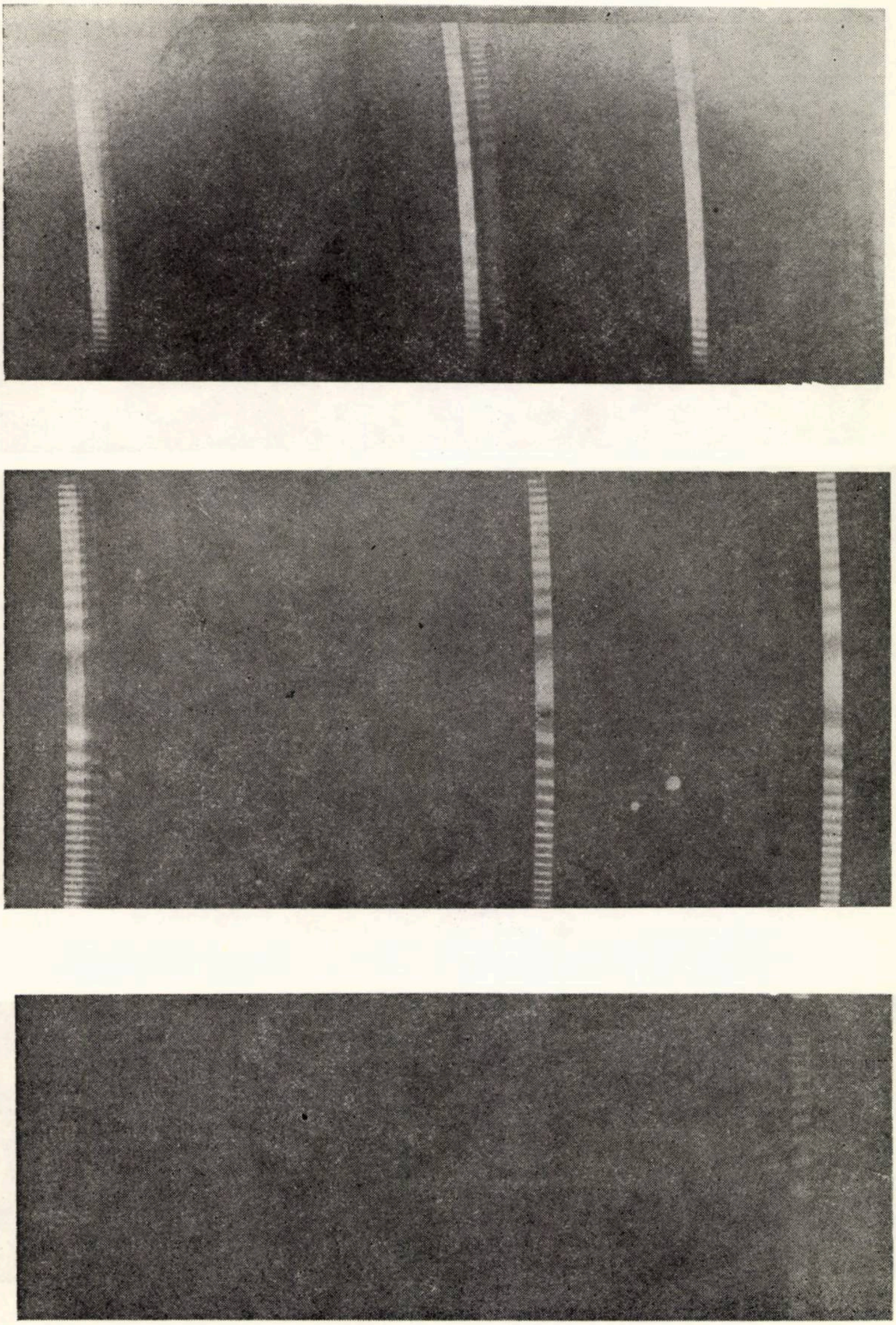

Fig. 3

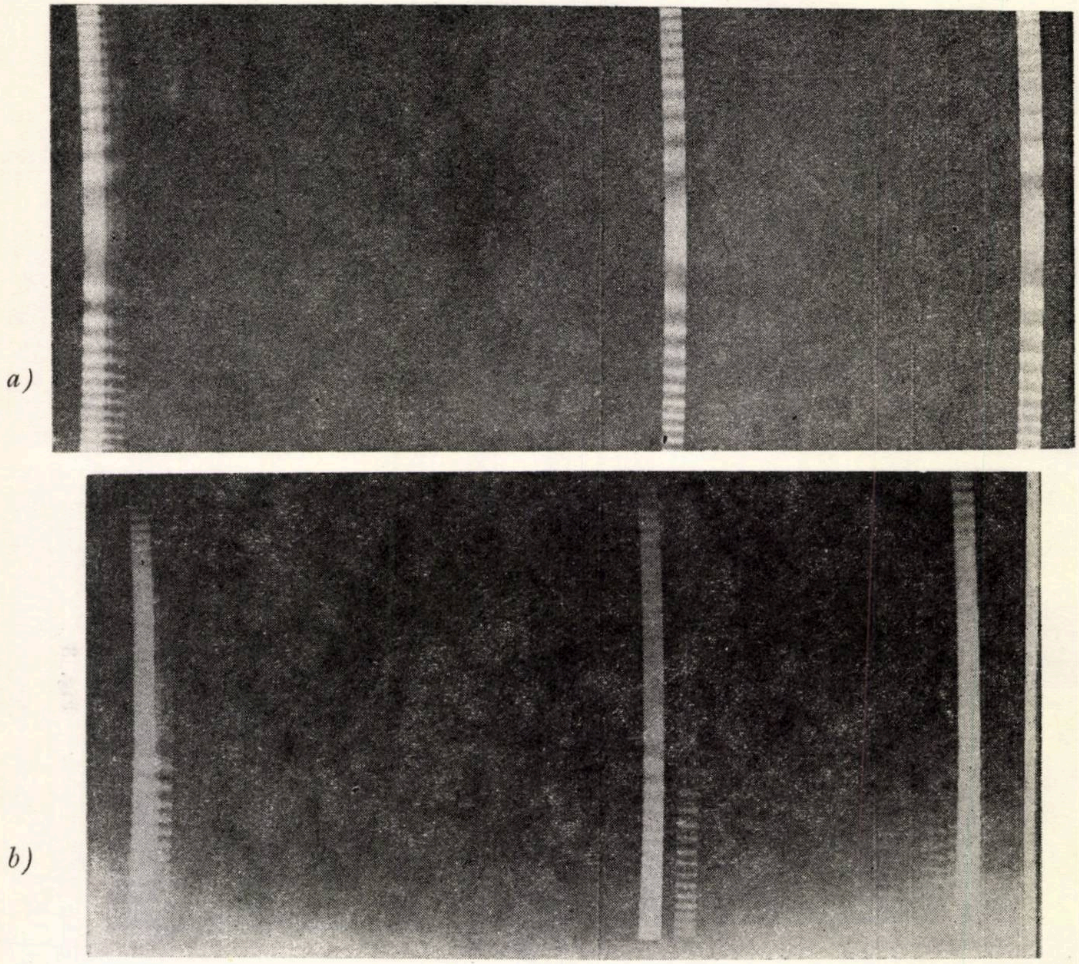

Fig. 4

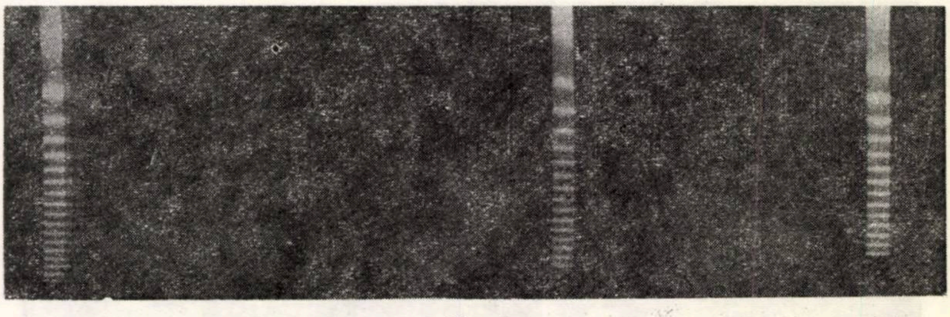

Fig. 5

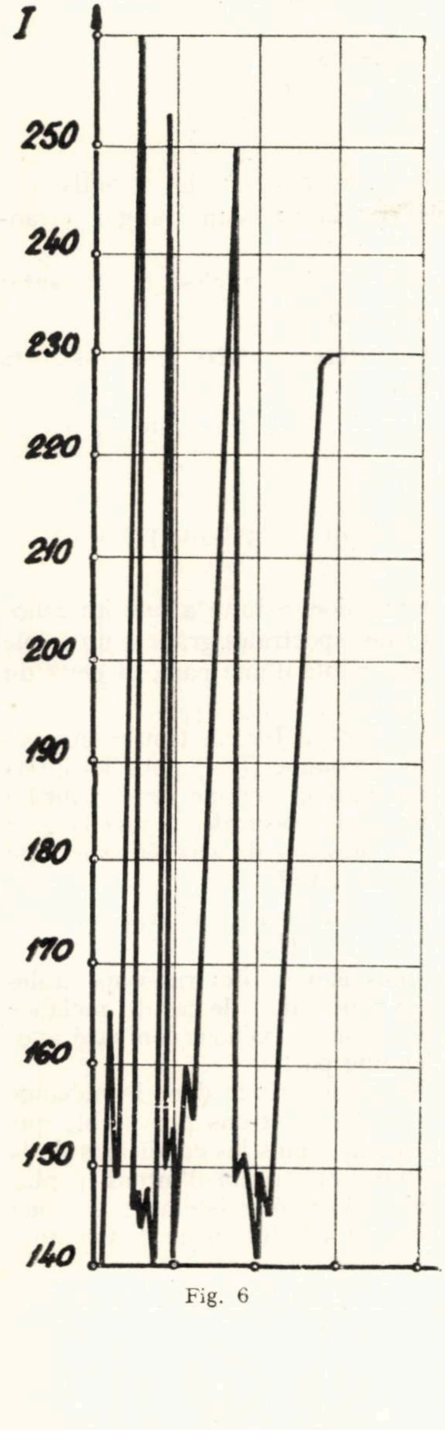
I
250
240
230
220
210
200
190
180
170
160
150
140

Fig. 6

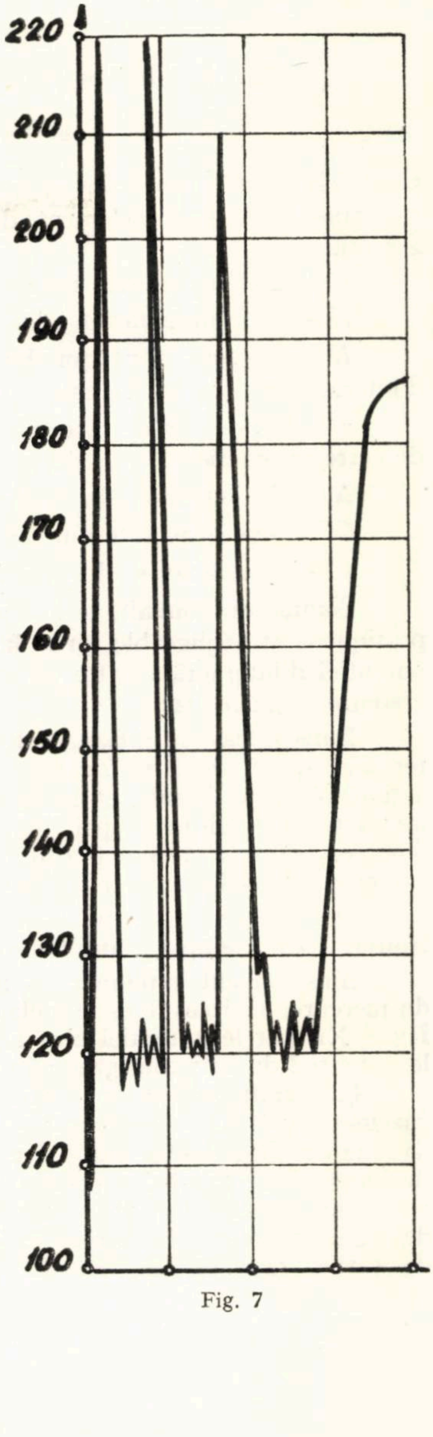
220
210
200
190
180
170
160
150
140
130
120
110
100

Fig. 7

On sait que la théorie quantique donne la relation:

$$\mathrm{I}(\nu) = \frac{4\pi N^{3/\eta}}{\eta(2\pi\Delta\nu)^{\frac{\eta+3}{\eta}}}\left(1 + \frac{4\pi C''\Delta\nu}{3KkT}\right)^{1/2}$$

pour l'intensité des raies spectrales, dans le cas où les profils des ces raies sont essentiellement déterminés par la pression du gaz étranger (7).

La signification des notations dans cette relation c'est là suivante:

N — la concentration des atoms perturbateurs

K — un coefficient qui dépend de la différence entre les constantes d'interaction pour les niveaux perturbateurs

η — le pouvoir de la constante d'interaction qui détermine la nature de cette interaction

$\Delta\nu$ — la lageur de la raie en sec^{-1}

C'' — une constante qui caractérise le niveau énergétique perturbateur

k — la constante du Boltzmann.

Comme on connaît, le gaz noble à la pression reduite a une influence pratiquement négligeable sur la largeur des raies spectrales grâce à un faible potentiel d'interaction entre les atoms du gaz noble d'une part, et ceux du mercure, d'autre part.

Dans le cas du mélange alcalines-gaz noble J. Jordan trouve des potentiales qui varient en fonction de la distance comme $f(r^{-6})$ pour les interactions Wan-der-Waals, et des potentiales qui varient comme $f(r^{-8})$ pour les interactions dipol-quadrupol, l'intensité d'une raie spectrale, à une largeur donnée, ayant déterminé, pratiquement, par la pression du gaz étranger qui exercite une influence sur les paramètres de similitude.

Des détails en ce qui concerne le mécanism de la décharge on peut trouver, par exemple, dans les ouvrages (10), (11), (12).

Ainsi on eut expliquer les intensités plus élevées des raies spectrales du mercure, excitées dans le mélange Hg + Kr, que dans le cas du mélange Hg + Xr, par le potentiel plus faibles d'ionisation du xénon, comparé avec le potentiel du krypton, grâce à un effet Penning partiel.

Ça signifie que dans le cas de la décharge électrique dans le mélange gazeuse Hg + Xe on obtient une température des électrons plus faible que dans le cas du mélange Hg + Kr. Par conséquence dans les conditions de la décharge dans Hg + Xe on obtient un courant électrique d'intensité plus élevé que dans le cas Hg + Kr et ça conduit à un élargissement Doppler des raies spectrale du mercur et à une mauvaise résolution de la structure de cettes raies.

Université de Bucarest, Faculté de Physique

BIBLIOGRAPHIE

И. М. Бетеров, В. М. Клементиев, В. П. Чедотиев Опт. и (спектр., 25, 477, 1968.
В. Числер, Опт. и (спектр. 29, 208, 1970.
Ф. А. Королев, Вестник М.Г.У. 1957.
V. Drăgănescu: Studii şi Cercetări de Fizică, 4, 855, 1959.
Iancu Iova: An. Univ. Buc. seria Ştiinţele naturii Fizică. An. XIV, 15, (1965).
S. Tolansky: High Resolution Spectroscopy, London 1947.
Alexander Iablonsky: Phys. Rev. Vol. 68 Nr. 34, Pag. 78 (1945)
Ф. А. Королев, Спектроскопия высокой разрещающей силы. Г.У.Т.Т.Л. — Москва 1953.
J. Jordan: Thesis, Univ. of Michigan, 1964.
N. A. Kapţov: Fenomene electrice în gaze şi vid, Bucureşti, Editura Tehnică, 1955 (Traducere din limba rusă)
E. Bădărău şi Popescu: Gaze Ionizate: Descărcări electrice în Gaze, Bucureşti, Editura Tehnică, 1965.
G. G. Brătescu: Fizica Plasmei, Editura Didactică şi Pedagogică Bucureşti, 1970.

VOLUME RECOMBINATION AND DIFFUSION LOSSES IN A NEON DISCHARGE PLASMA

EMIL I. TOADER *

1. INTRODUCTION

The contracted cylindrical plasma column is the subject of many investigation and two modes of study of the contraction phenomenon can be distinguished: the diffusion mode and the volume mode. Both diffusion mode and volume mode are stationary modes. In comparison with the Schottky theory (1924), the main new ideas of the diffusion mode deal with two-step ionization (Spenke 1950), multistep ionization and recombination (Ul'yanov 1965) and the fact that the excitation of high levels and the ionization depend very strongly on the type of tail of the electron velocity-distribution, which is not Maxwellian (Kagan and Lyaguschenko 1965). The volume mode describes the contraction from the termal point of view (Golubovskii et al. 1951, Kenty 1962, Massey and Cannon 1965, Baranov and Ul'yanov 1969, Rachimov and Ulinich 1970).

In a recent work (Toader 1967), in which was studied the contraction of a Neon d.c. discharge, long positive column for a pressure range of 2—32 Torr, the author obtained a fair agreement between experimental results and theoretical data based on the diffusion mode proposed by Kagan and Lyagushchenko, but only for the pressures which vary slightly from 8 Torr. The higher the pressure the more significant was discrepancy between the experiment and the theory. But it must be remarked that the diffusion mode assumes that the recombination in the plasma volume may be ignored in comparison with the diffusion. It seems to us that this approximation is not real for pressures higher than 10 Torr.

The subject of this paper is the examination of the rapport between ambipolar diffusion loss and volume recombination loss of the charge carriers, on a contracted Neon discharge, long positive column for the pressure range 2—32 Torr. For this we will use experimental results obtained for the electron temperature T_e, the density of the electrons n_e across the centre-line tube, the axial electric field E, the ionic current density at the discharge tube walls J_p and for the electron radial distribution $n_e(\mathrm{r})$ (Toader 1967). At the same time, we will use the results obtained by Frommhold, Biondi and Mehr (1968) for recombination coefficient α_r as a function of the electron temperature.

---

* Permanent Address: University of Bucharest, Departament of Physics 14 Academiei, Rumania.

2. CHARGE CARRIER LOSSES

The steady-state plasma column which forms the cylindrically simmetric homogeneous positive column, was obtained in a 150 cm long, 2.2 inside diameter tube (Toader 1967). The plasma column loses its ions through diffusion if ions to the tube walls and through recombination. The laws governing losses by diffusion and recombination with time differ, and in many cases one process or the other can be made to predominate. Ambipolar diffusion losses are described by ambipolar diffusion coefficient D_a and predominate at lower pressures. Volume recombination losses become important at higher pressures and are described by recombination coefficient α_r.

The recombination processes may be radiative recombination processes or/and dissociative recombination processes. In our conditions, for the pressures of 2, 8, 16 and 32 Torr and for the electric current of 80, 160, 320 and 400 mA, radiative recombination processes in three-body collicions $Ne^+ + e + Ne - 2Ne + h\nu$ become ineffective in comparison with nonradiative recombination precesses (Veselovskii 1969). The radiative recombination coefficient α for the processes of the type $Ne^+ + 2e - Ne + e + h\nu$ has value $\alpha = 2 \cdot 3\, 10^{-8}\, n_e T_e^{-9/2}$ cm^3 s^{-1} (Mackin and Keck 1962) with the temperature expressed in degrees and n_e in cm^{-3}. Then, the only important process is the dissociative recombination between electrons and molecular ions of the type $Ne_2^+ + e \rightarrow Ne + Ne +$ kinetic energy, where $\alpha_r \sim T_e^{-0.49}$ (Frommhold, Biondi Mehr 1968).

3. BALANCE OF CHARGE CARRIERS

The balance between charge production and diffusion and recombination losses is given by:

$$Z = n_e \frac{1}{\tau} \tag{1}$$

where Z is the number of the ionization events in a c.c. and τ is the mean time an ion remains in discharge. It may be observed that we retain the assumptiones made in the diffusion mode, because Z can have any form. The only new process is dissociative recombination. Then, in our conditions:

$$\frac{1}{\tau_{\text{diff}}} + \frac{1}{\tau_{\text{rec}}} = \frac{1}{\tau} \tag{2}$$

where τ_{diff} is the mean diffusion time an ion remains in discharge and τ_{rec} is the mean recombination time an ion remains in discharge. The mean diffusion time can be estimated from the ambipolar processes:

$$\tau_{\text{diff}} = \frac{1}{(2 \cdot 4/r)^2} \, \frac{1}{D_a} \tag{3}$$

The mean recombination time can be estimated from the dissociative recombination processes:

$$\tau_{\text{rec}} = \frac{1}{\alpha_{\text{rec}} \, n_2^+} \tag{4}$$

where r is the radius of the plasma column and n_2^+ is the density of the molecular Neon ions.

4. RESULTS AND DISCUSSION

The values for the mean diffusion time τ_{diff}, the mean recombination time τ_{rec}, the mean total time τ, the density of molecular ions n_2^+, the number of the ionization events Z and the plasma column radius r, obtained in the case of Neon positive column are given in tables I, II, III and IV for the

TABLE I

Computed data at different pressures in Neon plasma,
Current intensity i = 80 mA

Pressnre p (Torr)	E/p_0 (V/Torr)	$n_2^+ \times 10^{10}$ (cm^{-3})	$\tau_{\text{diff}} \times 10^{-4}$ (s)	$\tau_{\text{rec}} \times 10^{-4}$ (s)	$\tau \times 10^{-4}$ (s)	$Z \times 10^{16}$ ($\text{cm}^{-3}\,s^{-1}$	r (cm)
2	1.9	0.62	0.8	70	0.8	0.77	1.1
8	0.67	2.8	2.5	15	2.2	1.1	0.92
16	0.47	42	4.9	0.88	0.88	4.9	0.72
32	0.30	61	32	0.54	0.54	11.3	0.55

TABLE II

Computed data at different pressures in Neon plasma
Current intensity i = 160 mA

Pressure (Torr)	E/p_0 (V/Torr)	$n_2^+ \times 10^{10}$ (cm^{-3})	$\tau_{\text{diff}} \times 10^{-4}$ (s)	$\tau_{\text{rec}} \times 10^{-4}$ (s)	$\tau \times 10^{-4}$ (s)	$Z \times 10^{16}$ ($\text{cm}^{-3}\,s^{-1}$)	r (cm)
2	1.56	0.9	0.84	50	0.84	1.0	1.1
8	0.53	5.2	3.1	7.7	2.3	2.3	0.95
16	0.36	72	5.6	0.49	0.49	14.7	0.82
32	0.25	126	6.4	0.26	0.26	48.4	0.58

TABLE III

Computed data at different pressures in Neon plasma.
Current intensity i = 360 mA

Pressure p (Torr)	E/p_0 (V/Torr)	$n_2^+ \times 10^{10}$ (cm^{-3})	$\tau_{\mathrm{diff}} \times 10^{-4}$ (s)	$\tau_{\mathrm{rec}} \times 10^{-4}$ (s)	$\tau \times 10^{-4}$ (s)	$Z \times 10^{16}$ ($\mathrm{cm}^{-3}\,s^{-1}$)	r (cm)
2	1.32	1.9	0.96	21	0.96	2.0	1.1
8	0.44	0.8	3.9	3.6	1.8	54	0.98
16	0.30	168	4.0	0.2	0.19	84	0.86
32	0.20	315	9.1	0.09	0.09	350	0.61

TABLE IV

Computed data at different pressure in Neon plasma.
Current intensity ï = 400 mA

Pressure p (Torr)	E/p_0 (V/Torr)	$n_2^+ \times 10^{10}$ (cm^{-3})	$\tau_{\mathrm{diff}} \times 10^{-4}$ (s)	$\tau_{\mathrm{rec}} \times 10^{-4}$ (s)	$\tau \times 10^{-4}$ (s)	$Z \times 10^{16}$ ($\mathrm{cm}^{-3}\,s^{-1}$)	r (cm)
2	1.25	2.6	1.0	17	1.0	2.6	1.1
8	0.44	12.7	5.1	2.7	1.7	7.4	1.9
16	0.24	182	8.8	0.18	0.18	101	0.92
32	0.18	362	10	0.08	0.08	452	0.65

pressures of 2, 8 16 and 32 Torr and for the electric current of 80, 160, 320 and 400 mA, respectively. The plasma column radius r was obtained making the extrapolation of the experimental curves which give the variation of the electron density across the tube, at the point where $n_e(r)/n_e(0) = 0$ (see figs. 2 and 3 from Toader, 1967). Under the present conditions, the density of the molecular ions have been considered 1% of the electron density for the pressures of 2 Torr and 8 Torr, and 10% for the pressures of 16 Torr and 32 Torr (Pahl and Weiman, 1958, 1959).

For the recombination coefficient α_{rec} we used the results obtained by Frommhold, Biondi and Mehr (1968). In general, $\alpha_{\mathrm{rec}}(Ne_2^+) \sim T_e^{-0.43}$ and for $T_e = 10^4\ ^\circ K$ there have been obtained the value $\alpha_{\mathrm{rec}} = 3 \cdot 5\ 10^{-8}\ \mathrm{cm}^3\ s^{-1}$. The ambipolar diffusion coefficient was computed from the relation $D_a = \frac{kT_e}{e}\mu_i$, and the ion mobility have been computed as a function of E/p_0 (Beaty and Patterson 1968):

$$\mu_i = 4.07\left\{1 + 8\ 10^{-3}\left(\frac{E}{p_0}\right)^2 + 2\ 10^{-6}\left(\frac{E}{p_0}\right)^4\right\}^{1\ 8}\frac{760}{p_0}\ \frac{T_0}{T} \tag{5}$$

where E is the electric field in V/cm and $p_0 = p\left(\frac{T_0}{T}\right)$($p$ is the gas pressure in Torr and $T = 400°K$ is the gas temperature).

The results obtained by us for the mean diffusion time τ_{aiff} and for the mean recombination time τ_{rec} (Tables I—IV) can be said to be a little unaspected. While the results obtained at pressure $p = 2$ Torr follow the ambipolar diffusion mechanism for all electric current values, when pressure raises at the value of 8 Torr the volume recombination mechanism becomes as important as ambipolar diffusion mechanism. To calculate the mean time an ion remains in discharge, one must take into consideration both diffusion loss and recombination loss. The higher the electric current the most effective are dissociative recombination processes. For pressure of 16 Torr the diffusion loss is smaller than recombination loss and becomes much smaller when $p = 32$ Torr. The values of the number of the ionization events Z computed from relation (1) describe correctly the processes from the discharge, We can verify this computing the ionic current density at the discharge tube walls using the relation $J_p^c = r^2 e Z/2R$. Thus, at the pressure of 2 Torr and for the electric current of 80 mA, the computed value of the ionic current density is 0.68 mA cm^{-2} which is in fair agreement with the experimental value 0.42 mA cm^{-2} (Toader 1967). At the pressure of 32 Torr, where the recombination losses are extremely effective, the computed value of the ionic current density is 2.46 $mA\ cm^{-2}$ which differes very much from the experimental value 0.15 $mA\ cm^{-2}$. This great discrepancy appears because to compute the ionic current density, the recombination loss was not taken into consideration.

In general, the results presented in this paper are in fairly good agreement with the conclusions raported by Chiplonkar and Joshi (1969) who showed that the process of volume recombination plays a significant role in determining the radial distribution of charge-carrier density even for low pressures (Chiplonakar and Joshi) used an argon and air positive column within a pressure range of 0.2—1 Torr).

As regards the radial variation in the electron temperature T_e and in the gas temperature T_e function of the pressure and current, Baranov and Ul'yanov (1969) used movable double probes to determine the electron temperature and they were able to report the radial variation in T_e even for an argon pressure of 1 Torr. Also they raported high variation in the gas temperature distribution over the discharge cross section. In contradiction with these results, Golubovskii, Kagan and Lyagushchenko (1966) raported no sistematical change in T_e along the radius, T_e being constant within the error of measurements. Subsequent observation taken by Chiplonkar and Joshi (1969) showed that the radial variation of electron temperature was insignificant. Our tests (Toader 1967, 1969) have shown that at pressures smaller than 10 Torr the electron temperature may be considered constant, the variation found during the experiments being within the experimental error range. However, at pressure higher than 10 Torr the electron temperature was found to decrease from the tube centre-line toward the tube walls. The question of the atom temperature T has been discussed by Edwin and

Turner (1969) who showed that T is in fact quite low. Obviously, new experimental studies are needed to decide between these different results. Therefore, we have adopted the T_e value obtained across the tube centre-line (Toader 1967) and $T = 400°K$.

ACKNOWLEDGEMENT

I wishe to express thanks to Prof. F. Crawford, Dr. J. Forrest and Dr. S. Self for many interesting discusions. Thanks are also due to the Senior Fulbright-Hays Program and Stanford University for financial support.

REFERENCES

Baranov, V. Yu., Ul'yanov, K. N., 1969, Soviet Physics-Technical Physics, 14, 176
Beaty, E. C., Patterson, P. L., 1968, Phys. Rev., 170, 116
Chiplonkar, V. T., Joshi, S. B., 1969, Physica, 45, 189
Edwin, R. P., Turner, R., 1969, Proc. 9-th Int. Conf. on Ionization Phenomena in Gases, Bucharest, (1969), pp. 155
Frommhold, L., Biondi, M. A., Mehr, F. J., 1968, Phys. Rev., 165, 44
Golubovskii, Yu. B., Kagan, Yu. M., Lyagushchenko, R. I., 1951, Opt. Spektrosk., 20, 561, 1966, 21, 525
Kagan, Yu. M., Lyagushchenko, R. I., 1965, Soviet Physics-Technical Physics, 9, 1445
Kenty, C., 1962, Phys. Rev., 126, 1235
Mackin, B., Keck, J. C., 1963, Phys. Rev. Lett., 11, 281
Massey, J., Cannon, S., 1965, J. Appl. Phys., 36, 361 and 373
Pahl, M., Weimer, U., 1957, Zs. Naturforsch., 12a, 926; 1958, 13a, 50, 278, 745, 753 1959, 14a, 239
Rakhimov, A. T., Ulinich, F. R., 1970, Soviet Physic-Docladay, 14, 655
Spenke, E., 1950, Phys. Zs., 127, 221
Schottky, W., 1924, Phys. Zs., 25, 635
Toader, E. I., 1967, Int. J. Electronics, 23, 417; 1969, 26, 553
Ul'yanov, K. N., 1965, Magnetohydrodynamics (In Russian) 4, 45
Veselovskii, I. S., 1969, Soviet Physics-Technical Physics, 14, 193

THE ELECTRON TEMPERATURE IN A NORMAL DISCHARGE IN HYDROGEN, OXYGEN, HELIUM AND ARGON IN D.C. CURRENT

MARIA COMĂNESCU

I. INTRODUCTION

As it is known, in order to know the phenomena occuring into the volume of a discharge in gases, a series of parameters in connection with the discharge process must be determined; the electron and ion velocities distribution law, the electron concentration and temperature in a certain region of the discharge.

Our aim is to determine the discharge parameters in D.C. current in the space between the cathode and the beginning of the positive column as a function of the gas nature, pression and discharge current intensity.

Because of the numerous necessary measurements, in order to know the velocities distribution, we had to limitate ourselves to a method without too big technical difficulties and at the same time giving the possibility to recognise the maxwellian velocities distribution directly from the characteristics resulted from measurements. We found suitable for this purpose the Lougmuir probe method because if the probe semilogarithmic characteristic is linear we have a certain indication for maxwellian distribution. Moreover, the probe method allows the determination of the other plasma parameters.

II. MEASUREMENT DEVICE

We used a 5.5 cm diameter discharge tube with two aluminium electrodes, a disc cathode and a ring anode located at 25 cm from the cathode, into the tube.

The movable platinum probe, 0.2 mm in diameter and 0.5 cm long, was placed axially to the tube. The measurement device is given in fig. 1.

The voltage applied to the probe was taken on a double potentiometric device from a 250 V rectifier. The sonde current was measured with a galvanometer ($K = 7 \times 10^{-8}$ A/div. and $R_1 = 2 \cdot 5\ K\Omega$), and the current through the discharge tube with a miliampermeter.

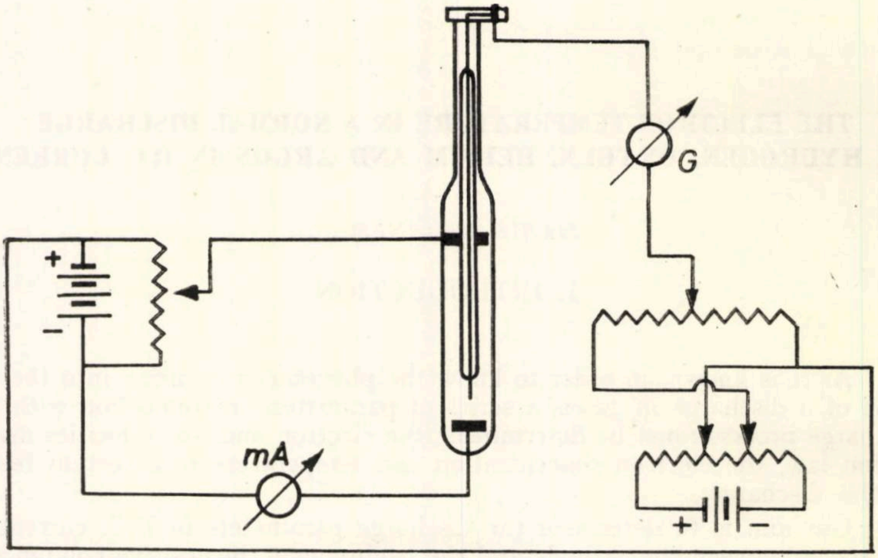

Fig. 1

The discharge tube feeded by means of a potentiometric device and a 20,000 ohm variable resistance from a 1200 V accumulator battery is put in connection with a molecular pump with mercury vapours preceeded by a rotative oil pump. The pressure was measured with a Mac-Leod gauge calibrated in the 10^{-1} up to 10^{-5} torr range. Y*A* liquid nitrogen trap was used in order to eliminate mercury vapours.

Measurements were made in hydrogen, oxygen, helium and argon.

The hydrogen was prepared in a Kipp apparatus ($Zn + H_2So_4$) and introduced into the tube after being purified through a series of washing vases with lead acetate, alkalinised potassium permanganate, potassium hydroxide, pyrogallol and finally dryed with calcium cloride.

The oxigen was prepared by potassium permanganate heating and helium and argon were taken from vessels produced by Veb Technische Gase-Werke Berlin.

The probe characteristic $i_s = f(V_s)$ was plotted beginning from the high negative potentials of the probe when the probe current is produced by positive ions only. By decreasing the probe negative potential, the electrons with higher energies than $(V_s - V_o)$, in the probe direction, can reach the probe and by this way over the ion current (i^+) a electron current of opposite sign (i^-) is superimposing. V_o is the plasma potential in the probe region. By substracting ion current (i^+) from the total probe current, the electronic one (i^-) can be obtained. When the probe characteristic $i_s = v(V_s)$ is plotted, a straight line is obtained for the region where i^+ exists only. The graphic difference $i - i^+$ is logarithmically plotted, $\log i^- = f(V_s)$.

If there is only a group of electrons, the curve $i = f(V)_s$ will be a straight line with a sudden deviation for $V_s > V_o$.

In the case when there are more groups of electrons, the curve presents several straight portions.

According to Langmuir the electron current logarithmic characteristics with three or two fracture points is explained by the existence of three groups of electrons (primary, secondary and slow) orof two groups (secondary and slow).

Kaptzow instead of two groups, (both of them with maxwellian distributions with different average velocities), suggests to consider a only group with a velocities distribution deviating from the maxwellian one.

Medicus and Waymouth consider that the characteristics shape is owing to the existence of two groups: a slow one (secondary) with an enough good maxwellian distribution and a fast group (primary) with a more or less marked velocities spectrum. M. Schönhuber calls these characteristics with two or three bend points recognizing lines, *c* (C Kennlinien), because of their resemblance with C letter.

I. Paulus, L. Schott in the paper „Die Geschwindikeitsverteilung der Elektronen in der positive Saule einer eigenschnurten Niederdrukentladung", by introduction of a diaphragm in the positive column of a discharge at low pressure in nitrogen, found similar characteristics explained by the superimposing of two groups of maxwellian electrons with different temperatures.

Paul Stubei in the paper „Studiul ionilor negativi de H_2 în prezența vaporilor de mercur", finds in the Faraday space characteristics with two bend points which he explains as being owed to the existence of two distinct electron groups with maxwellian distribution.

Langmuir formula allows the calculation of the temperature and concentration of each electron group

$$i^- = N^- e \sqrt{\frac{K}{2\pi m}} \cdot T^{1/2} \varepsilon^{-\frac{e}{KT}(V_s - V_o)}$$

where N is the electron concentration in a cubic cm

e is the electron charge $= 4.8 \times 10^{-10}$ electrostatic units,

K is the Boltzman constant $= 1.38 \times 10^{-16}$ erg. grad^{-1},

m is the electron mass $= 9.1 \times 10^{-28}$ gramm.

We established that between cathode and positive column, in hydrogen, oxygen and argon, the logarithmic characteristics of the electron current were always broken lines with three straight segments denoting the existence of three electron groups with different temperatures. These two or three electron groups can't be identified with the three electron groups found by Langmuir in the positive column of the mercury arc.

The three electron groups found by Langmuir can be observed even on the sonde characteristics, the logarithmic one being no more necessary.

The trajectory of the cathodic electrons is parallel to the probe platinum wire, and consequently these electrons will be rejected even for the lowest negative probe potentials $(V_s - V_o) < 0$. This remark is important because in the region between the cathode and positive column approximately half of the current is carried by the high velocity electrons (cathodic). Because of that, the probe was located coaxially with the discharge tube axis and parallel to this axis.

The electrons catched up to the potentials $(V_s - V_o) > 0$ have a distribution on all azimuths. (R. Pârvan: „Proprietățile electronilor rapizi din descărcările în gaze în curent continuu la presiuni joase".

Since on the first straight segment of the characteristic is corresponding to high negative probe potentials (V_s) and only a few electrons from the second group is contributing, from the slope of this segment results the temperature of the first group. The slope of the second straight segment of the electron current characteristic allows the temperature calculation of the second electron group. (Francis P. Chen. — Electric probes. Plasma diagnostic techniques).

The temperature of the second group of electrons was calculated too according to the method indicated by Th. V. Ionescu:

The probe curve and the curve $\log i^- = f(V_s)$ up to the region $V_s = V_o$ was plotted obtaining a straight line. This line was prolonged and it was passed from $\log i^-$ values to i_1^- further, getting this way the whole curve of the first electron group.

The curve representing $\log i_2^-$ was obtained by taking the logarithm of the differences between the computed curve i_1^- and the experimental one.

The resulted straight line may represent the second group of free electrons and the slope of this line allows the temperature calculation of the second electron group (T_2^-).

In fig. 2 both ways of calculation are presented.

From the probe current characteristic the electron density in plasma can be computed too using Langmuir relation for cylindrical probes *if* plasma potential is known and *if* there is one electron group only so that $V_s = V_o$. In this case:

$$s^- = 2\pi r_s e N_e^- \sqrt{\frac{KT^-}{2\pi m}}$$

where j^- is the current on probe unit length and this current corresponds to the bend point (sudden slope changing) of the line $\log i^- = f(V_s)$. Knowing electron temperature, their average energy can be immediately computed using the relation:

$$W_e = \frac{mV^2}{2} = \frac{3}{2} KT \text{ ergs} = T/7740 \text{ V}.$$

where K is Boltzmann's constant $= 1.38 \times 10^{-6}$ erg/grad^{-1} and $T =$ electron temperature.

As far as the probe potential is lower than that of the surrounding plasma, the logarithmic characteristic of the electron current must be a straight

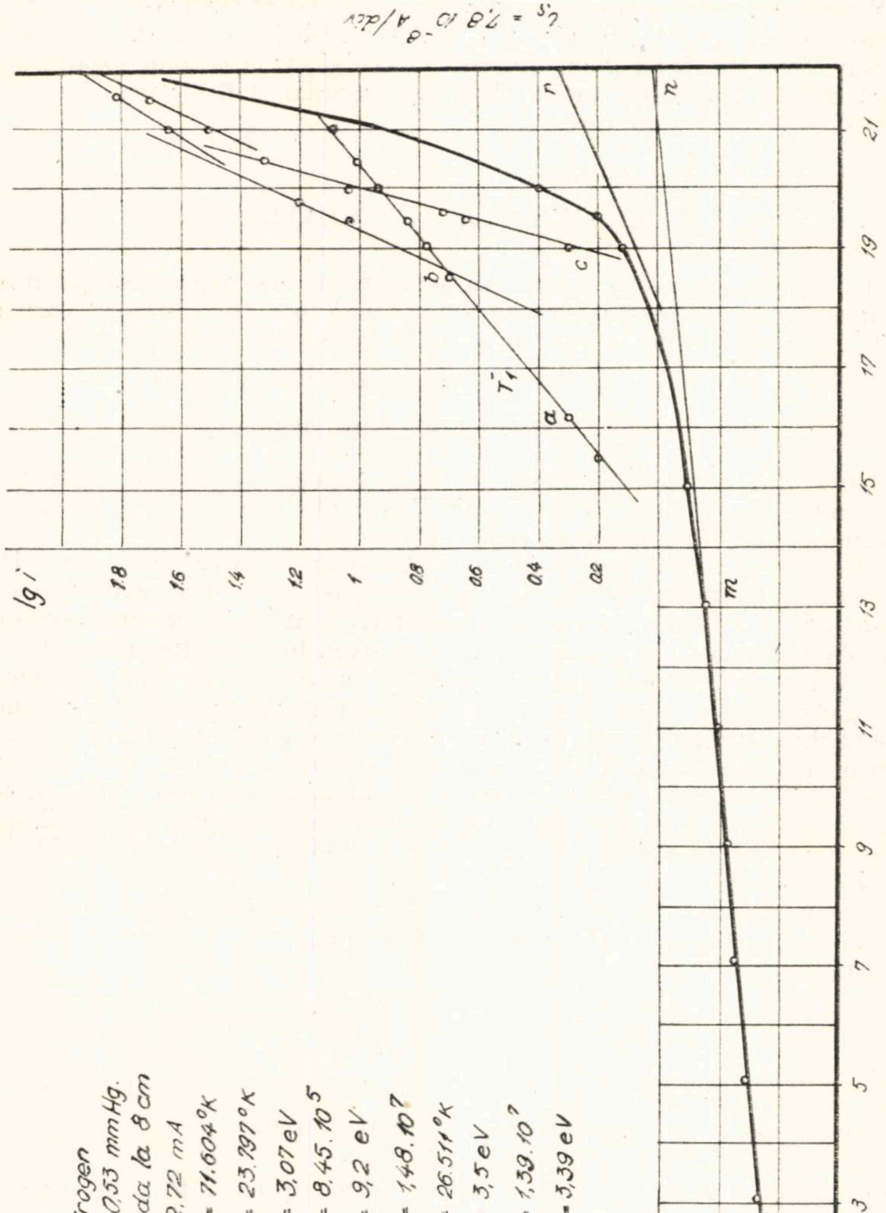
$i_s = 7,8\ 10^{-8}$ A/div
lg i
1.8
1.6
1.4
1.2
1
0.8
0.6
0.4
0.2
1
3
5
7
9
11
13
15
17
19
21
m
m
n
r
a
b
c
T_1^-
Hidrogen
p = 0,53 mmHg.
Sonda la 8 cm
I = 2,72 mA
$T_1^- = 71.604\,^\circ K$
$T_2' = 23.797\,^\circ K$
$W_2 = 3,07$ eV
$N_1^- = 8,45 . 10^5$
$W_e = 9,2$ eV
$N_2^- = 1,48 . 10^7$
$T_2' = 26.511\,^\circ K$
$W_2' = 3,5$ eV
$N_2^- = 1,39 . 10^7$
$W_2^- = 3,39$ eV

Fig. 2

line. When the probe potential becomes equal to that of the plasma, the characteristic log $i^- = f(V_s)$ suddenly changes his shape — Langmuir's point. This way, from the bend point abscissa of the electron current logarithmic characteristic it is possible to establish the potential of the place where the probe is introduced into the plasma.

IV. EXAMPLE OF CALCULATION

In fig. 2 is shown a probe characteristic in hydrogen resulted from experiment. The gas pressure in the tube is 0.53 torr, the discharge current I = 2.72 mA, the probe is located at 8 cm from the cathode.

$$T_i = 71600°K,\ N_i^- = 8.45 \times 10^5,\ W_i^- = 9.2\ eV.\ .$$

$$T_2^- = 26511°K,\ N_2^- = 1.39 \times 10^7,\ W_2^- = 3.5\ eV.,$$

calculated from the slope of the second linear segment of the electron current logarithmic characteristic or $T_2^- = 23797°K$ and $W_2^- = 3.07\ eV$, calculated according to the other method (Th. V. Ionescu).

The experimental probe characteristic is drawn with thick line. The probe current produced by positive ions only was obtained by extending the straight line representing the probe characteristic at high negative values of the probe potential. The probe current i_s is given by the difference between the experimental curve i and the positive ion current i^+. This difference was logarithmically drawn on the diagram obtaining always a broken line made of three straight segments. From the slope of the first straight segment the temperature of the first electron group has been calculated. For that two points on the segment whose currents are in 2.72 ratio were chosen, for instance the point a corresponds to log $i = 0.3$, and consequently, $i = 2$, and the point b corresponds to $i = 2 \times 2.73 = 5.44$ and log $5.44 = 0.73$. On the probe potentiometer rule the difference $(a—b) = 27$ mm.

From experimental data to these 27 mm there correspond 6.17 volts.

Since the slope of the curve representing the electron current is given by

$$\frac{d(\log \cdot 1^-)}{dV} = \frac{e}{KT} = \frac{1 \cdot 17 \times 10^4}{T^-},\ \text{and because}$$

the slope is inversely to the potential difference between two points whose currents are in $\frac{1}{2 \cdot 72}$ ratio, the calculation is simplified:

$$T_i^- = 1.17 \times 10^4\ V_s — \text{therefore}\ T_i^- = 1.17 \times 10^4 \times 6.17 = 71.604°K$$

The temperature of the second kind of electrons was calculated using both methods.

In order to eliminate from the next calculations the influence of the first electron group, according to Th. V. Ionescu — the values on the line

T_i^- are taken from the begining of the probe characteristic curvature to the right side, and the corresponding currents were logarithmically marked with respect to the straight line (m — n). We obtain so the probe characteristic (m — r) representing the action of the first electron group.

The difference between the straight line, (p — r), and the total current curve gives the action of the second electron group.

These differences were logarithmically plotted and it was obtained the straight line T_2^-.

From the slope of this line the second electron group temperature was calculated, that, in this case, was 26,242°K.

If the second electron group temperature is calculated from the slope of the second straight segment of the logarithmic characteristic $\log i^- = f(V_s)$ then $T_2' = 26{,}511°K$.

The straight line T_i^- briskly changes its slope for the probe current log $= 0.72$, therefore $i^- = 5.3 \times 7 \times 10^{-8} = 37.1 \times 10^{-8} A$.

The current on the probe unit length is:

$$j = \frac{37 \cdot 1 \times 10^{-8} \times 3 \cdot 10^{9}}{0.5} = 22.2610^{2} \text{ electrostatic units.}$$

The electron concentration in 1 cm³, if the constants are introduced in Langmuir's formula, is given by:

$$N_i^- = \frac{449 \times 10^5\, i}{\sqrt{T_i}} = \frac{449 \times 10^5}{\sqrt{71\,600}} \times 5 \cdot 3 = 8.45 \times 10^5$$

From the straight line T_2^- and from the second segment of the straight line T_1^-, the density (electron number in 1 cm³) of the second electron group can be similarly calculated that in the present case is $N_2^- = 1 \cdot 48 \times 10^7$ or $1 \cdot 39 \times \times 10^7$. From the relation:

$$We^- = \frac{mV^2}{2} = \frac{3}{2} KT \text{ erg} = T^- /7740\, eV.$$

The average kinetic energy of both electron groups was calculated obtaining 9.2 eV for the first group and 3.07 eV or 3.5 eV for the second one.

The probe Volt-amper characteristic can get out of shape when the electron distribution function changes. Druyvesteyen showed how can the electron velocities distribution function be found from the probe characteristics, by twice differentiating of the electron current with respect to the probe potential

Medicus has suggested a method of double graphical derivation to find this function. This method was used in the present paper.

The probe curve from fig. 2 has been analised with Medicus graphical method and a distribution like in fig. 3 was obtained. On this distribution the two electron groups can be observed.

Remarks about electron velocities and concentration calculation methods follow.

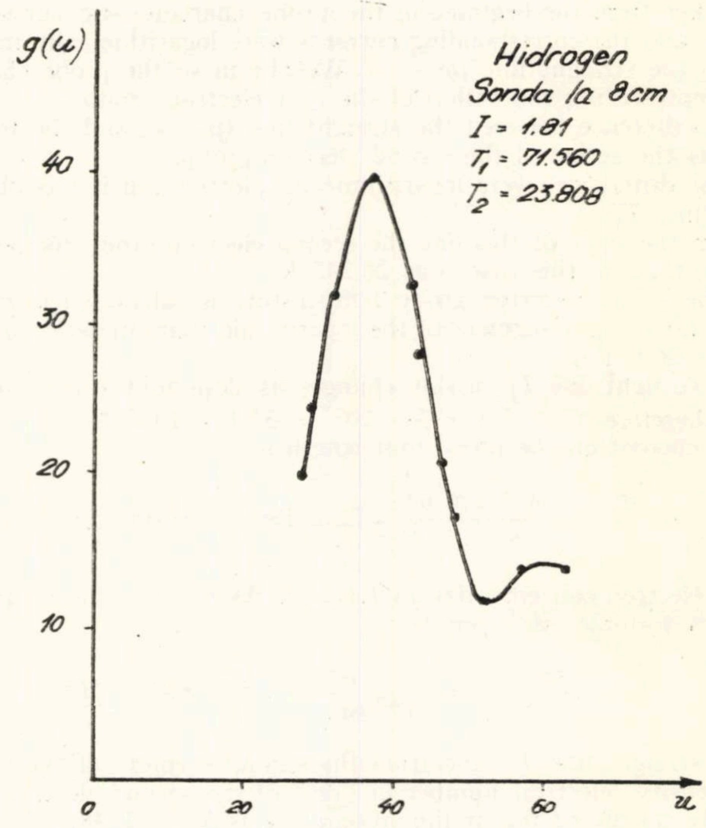

Fig. 3

In the first calculation method (Langmuir) the experimental curvt logarithm in this discharge region, as it was said and can be seen from whae follows, is dividing in a few straight segments.

Each segment corresponds to an electron group of a certain temperature and given concentration. All is happening as if for a value of the probe potential $V_s - V_o$, the maxwellian repartition briskly changes the parameters. T_1^- becomes T_2^- and N_1^- becomes N_2^-; similarly when a third segment exists N_2^- changes in N_3^- and T_2^- in T_3^-. The plasma potential remains unchanged. In this case the current intensity can be calculated on both sides of the fracture points, that differs very little from V_s, and at limit tends towards V_s. consequently It can be written:

$$i = N_1^- e \sqrt{\frac{K}{2\pi m}}\, T_1^{1/2} = N_2^- e \sqrt{\frac{K}{2\pi m}}\, T_2^{1/2}$$

because $\varepsilon^{-\frac{e}{KT}(V_s - V_0)}$

keeps the same value for both segments.

Therefore,

$$N_1 T_2^{1/2} = N_2 T_2^{1/2} \quad \text{and} \quad \frac{T_1}{T_2} = \frac{N_2^2}{N_1^2}$$

That is, the temperatures ratio is inversely to the square of the ionisation densities. In this case one can not say that the two groups of electrons whose temperatures should be T_1 and T_2 coexist, because both of them being exponential, the logarithm of sum is not equal with the sum of the logarithms. herefore in the moment when the group with temperature T_1 disappears, the group with temperature T_2 appears.

Let us admit two groups with temperatures T_1 and T_2. For $V_s = V_o$, j has a value say j_2, and consequentey,

$$J_2 = 2\pi r_s e N_e^- \sqrt{\frac{KT_2}{2\pi m}}$$

If only existed this group, the straight line T representing it (log i) should prolong towards high values of (V_s) until $j_2 = O$.

If only existed the first group, the straight line corresponding to T_1 prolonged towards low (V_s) values should give for $V_s - V_o = 0$ a value for j_1 unlike j_2.

We can't measure j_1, and consequently, can't measure N_1^- but we can deduce N_2 too from the relation

$$\frac{T_1}{T_2} = \frac{N_2^2}{N_1^2}$$

In the case of the second method (Th.V. Ionescu) all is happening as if j would have the value

$$j = N_1 e \sqrt{\frac{K}{2\pi m}}\, T_1^{1/2} \varepsilon^{-\frac{e}{KT}(V_s - V_o)}\, N_2 e \sqrt{\frac{K}{2\pi m}}\, T_2^{1/2} \varepsilon^{-\frac{e}{KT}(V_s - V_o)}$$

because in this case the product of logarithms can be considered as sum of logarithms.

Two straight lines with T_1 and T_2 temperatures appear but the electron group with T_2 temperature appears at a determined $V_s - V_o$ value deviating a little from the $V_s - V_o$ value from the precedent case. All happens as if in the case of high probe potentials the electron velocity entering the probe influence space diminishes because of the antagonist electric field. For probe potentials at which the second electron group appears, their velocity is enough to produce by ionisations this electron group with T_2 temperature. The electrons of N_1 concentration remain and are captured but those corresponding to N_2 concentration appear too.

If the apparition of the second electron group $(N_2 T_2)$ should be owed to the photons produced by the $(N_1 T_1)$ electron impact against the probe, then the number of the electron appeared (N_2) were proportional with N_1. This mechanism should be able to explain why the two electron groups put in evidence by the method of Th. V. Ionescu remain separable.

V. EXPERIMENTAL RESULTS

The mobile probe allowed that the whole region between the negative light and the cathodic edge of the positive column should be examined.

Probe characteristics have been plotted for discharge currents of 2.75 mA 1.81 *mA* and 0.9 *mA*. That is at 0.136 *mA* /cm^2, 0.09 *mA* /*cm*^{2} and 0.045 mA/ /cm^2 current densities, the gas pressure into the discharge tube remaining always 0.53 torr.

Because the logarithmic characteristics of the electron current were always straight lines, but with two bend points i.e. three straight segments, it was admitted the existence of an electron velocities distribution that can be considered as a product of three maxwellian distributions.

The temperature of this electron group depends upon the experimental conditions: the discharge current intensity, the gas pressure, the probe position with respect to the cathode. In fig. 2 is presented a probe characteristic in hydrogen resulted from the experiment as well as the logarithmic characteristic of the electron current.

In tables 1, 2, 3 as well as in fig. 4 are represented the values of the average kinetic energy of the first electron group as a function of the probe distance from the cathode. It is to be remarked that this electron group enters the Crookes space with an average kinetic energy of 12—13 *eV*. This energy rapidly diminishes down to a few *e*V as we approach the negative boundary. Going along the Faraday space, with a weak field, these electrons gradually gain again energy to excite and ionise not reaching the value they had at the beginning of Crookes space.

TABLE 1

I = 2,72 mA p = 0,5— torr

d_{cm}	$T_i^- 0°K$	$W_i^- eV.$	N_i^-	$T_2^- 0°K$	$W_2^- eV.$	N_2^-
0,6	92 313	11,9	$6{,}8 \cdot 10^5$	117 000	14,9	$1{,}96 \cdot 10^6$
0,9	47 970	6,2	$1{,}05 \cdot 10^6$	31 941	4,1	$5{,}54 \cdot 10^6$
1,2	25 272	3,2	$1{,}8 \cdot 10^6$	39 312	5,08	$6{,}32 \cdot 10^6$
2,8	36 404	4,7	$2{,}14 \cdot 10^6$	36 000	4,6	$4{,}72 \cdot 10^6$
3,5	30 388	3,09	$2{,}06 \cdot 10^6$	29 700	3,8	$4{,}95 \cdot 10^6$
4,2	42 120	5,4	$9{,}2 \cdot 10^5$	19 656	2,5	$1{,}02 \cdot 10^7$
5,7	61 777	7,9	$6{,}7 \cdot 10^5$	19 890	2,5	$1{,}01 \cdot 10^7$
8	71 600	9,2	$8{,}45 \cdot 10^5$	26 511	3,5	$1{,}39 \cdot 10^7$
9	65 167	8,4	$1{,}4 \cdot 10^6$	21 177	2,7	$1{,}68 \cdot 10^7$
10	62 648	8,09	$9{,}85 \cdot 10^5$	31 590	4,08	$8{,}09 \cdot 10^6$
11	57 590	7,4	$3{,}36 \cdot 10^5$	53 000	6,8	$9{,}66 \cdot 10^6$
12	63 648	8,2	$5{,}43 \cdot 10^5$	34 400	4,4	$6 \cdot 10^6$
13	69 648	8,9	$7{,}48 \cdot 10^5$	37 018	4,7	$3{,}73 \cdot 10^6$
14	46 132	5,9	$1{,}37 \cdot 10^6$	43 758	5,5	$2{,}78 \cdot 10^6$

TABLE 2

I = 1,81 mA $p = 0,53$ torr

d_{cm}	$\overline{T}_i$ °K	$\overline{W}_i$ eV	$\overline{N}_i$	$\overline{T}_2$ °K	$\overline{W}_2$ eV	$\overline{N}_2$
0,6	92 150	11,9	$1,37 \cdot 10^6$	16 6078	20,1	$3,16 \cdot 10^6$
0,9	64 216	8,2	$8,09 \cdot 10^5$	36 500	4,7	$3,8 \cdot 10^6$
1,2	19 625	2,5	$2,6 \cdot 10^6$	28 080	3,6	$1,23 \cdot 10^7$
2,8	28 430	3,6	$2,04 \cdot 10^6$	56 160	7,2	$6,08 \cdot 10^6$
3,4	36 504	4,7	$2,06 \cdot 10^6$	50 544	6,5	$1,01 \cdot 10^7$
4,2	50 544	6,5	$8,8 \cdot 10^5$	19 656	3,5	$9,85 \cdot 10^6$
5,7	56 180	7,2	$1,03 \cdot 10^6$	16 848	2,1	$1,009 \cdot 10^7$
8	53 003	6,9	$7,16 \cdot 10^5$	26 559	3,4	$1,26 \cdot 10^7$
9	71 600	9,2	$8,45 \cdot 10^5$	24 102	3,1	$1,44 \cdot 10^7$
10	55 928	7,1	$1,08 \cdot 10^6$	32 450	4,3	$0,96 \cdot 10^6$
12	58 266	7,5	$8,6 \cdot 10^5$	27 144	4,4	$5,48 \cdot 10^6$
13	61628	7,9	$5,43 \cdot 10^5$	39 600	5,1	$2,93 \cdot 10^6$
14	38 610	4,9	$1,14 \cdot 0\ 1^6$	45 200	5,7	$1,05 \cdot 210^7$

TABLE 3

I = 0,90 mA $p = 0,53$ torr

d_{cm}	$\overline{T}_i$ °K	$\overline{W}_i$ eV	$\overline{N}_i$	T_2°K	$\overline{W}_2$ vV	$\overline{N}_2$
0,6	105 470	13,7	$1,007 \cdot 10^6$	140 400	18	$2,3 \cdot 10^6$
1,2	28 430	3,6	$2,06 \cdot 10^6$	42 120	5,4	$3,74 \cdot 10^6$
28	33 696	4,3	$4,9 \cdot 10^5$	42 705	5,5	$5,01 \cdot 10^6$
3,5	30 888	3,9	$6,9 \cdot 10^6$	61 776	7,9	$9,05 \cdot 10^6$
4,2	45 162	5,8	$1,69 \cdot 10^6$	22 464	2,9	$1,32 \cdot 10^7$
5,7	44 928	5,7	$6,54 \cdot 10^5$	22 500	2,8	$1,11 \cdot 10^7$
9	71 168	9,1	$8,45 \cdot 10^5$	31 824	4,1	$9,67 \cdot 10^6$
10	47 736	6,09	$9,47 \cdot 10^5$	34 394	4,4	$5,01 \cdot 10^6$
12	45 045	5,8	$8,48 \cdot 10^5$	63 648	8,2	$5,89 \cdot 10^6$
13	49 440	6,3	$1,01 \cdot 10^6$	44 460	5,7	$3,7 \cdot 10^6$
14	41 184	4,8	$1,7 \cdot 10^6$	74 000	9,5	$6,6 \cdot 10^6$

As far as the second electron group is concerned, their average kinetic energy calculated from the slope of the second straight segment of the electron current logarithmic characteristic is, at the beginning of Crookes space, higher that that of the first electron group but diminishes rapidly near the negative boundary to increase lightly along Faraday space.

In the negative boundary the average kinetic energy for both electron groups is minimum.

Under the same experimental conditions, the, temperature of the second electron group, is a little lower than half of the first one computed after eliminating the first electron group influence according to the indications of Acad. Th. V. Ionescu.

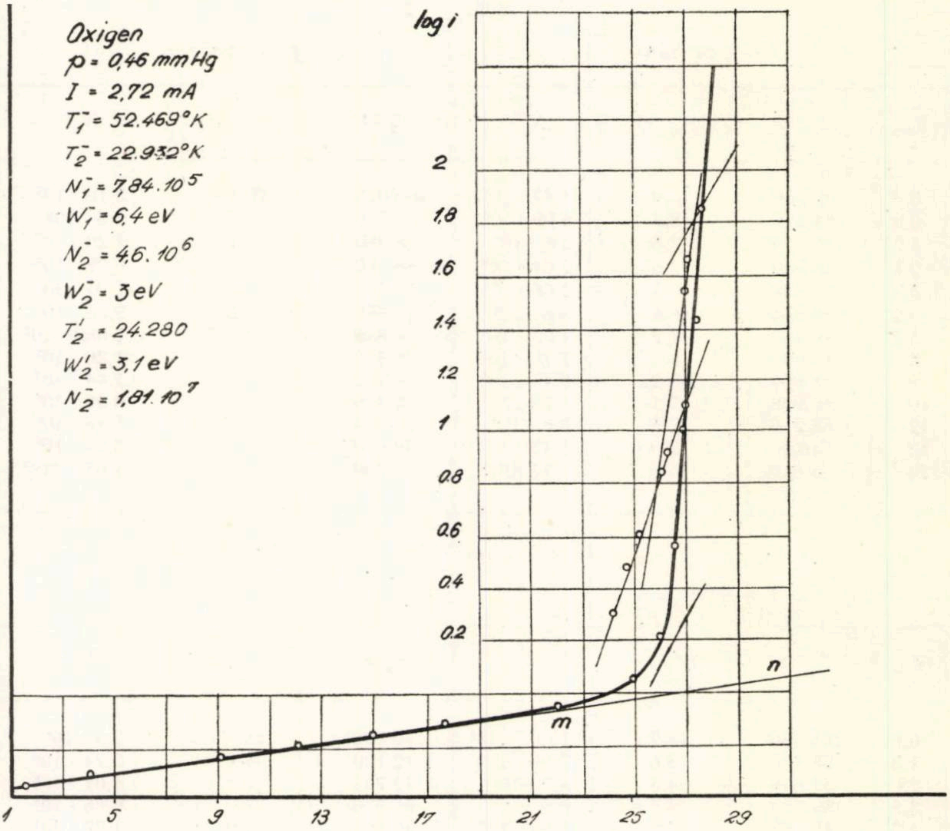

Fig. 4

Because the electron current densities were between 0.136 *mA/cm* and 0.045 mA/cm^2, and the pressure was allways 0.53 torr, the first electron group concentration did not exceed 2.6 × 10 in the negative boundary the concentration of the second electron group being about 5 times higher.

From fig. 5 and 6 it can be seen that at the beginning of Crookes space the temperature of both electron groups is maximum, whereas their concentration is minimum. This concentration raises rapidly up to the negative boundary where becomes about three times higher, to, remain along Faraday space about constant.

Because the distances from the cathode at which the first electron group concentration is maximum somehow coincide with the distances from the cathode, where the second electron group concentration is minimum, it seems that this last group should appear as a consequence of the inelastic collisions between the electrons of the first group against the neutral molecules.

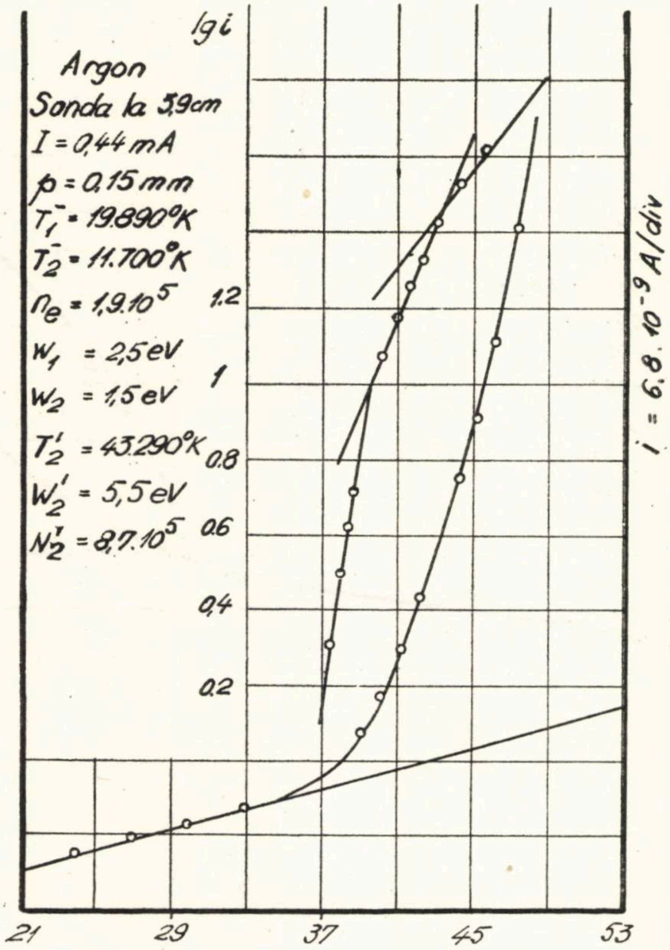

Fig. 5

Boyd, Thoson and Twidy admit that this electron group should contani electrons that lost a part of their energy in inelastic collisions and of those appearing from ionising collisions.

It can be assumed too that the negative ions entering the space wich is full of positive ions created by the probe, slow neutral molecules and free electrons.

Their free energy should be in this case the average energy with that they loose the molecules and, their temperatures should correspond to this energy.

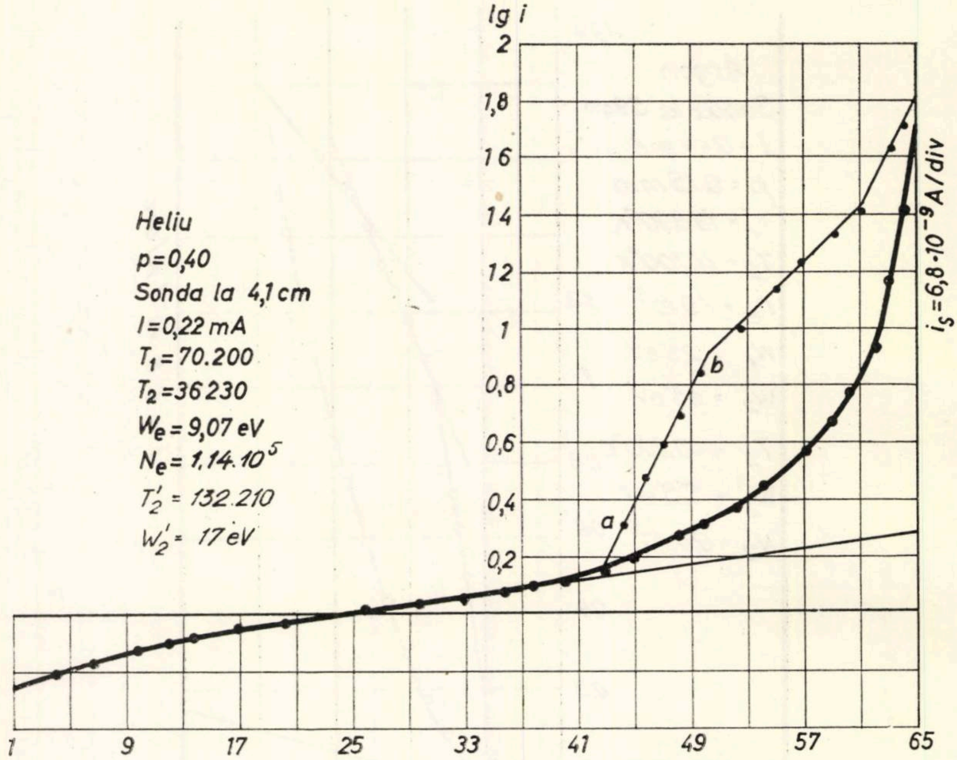

Fig. 6

2. OXYGEN

We worked at current intensities of 2.72 mA, 1.81 mA and 1.09 mA the gas pressure in tube being 0.46 torr.

In this case too, the electron current logarithmic characteristics were always straight lines, but with two bend points and it was considered that there are three electron group with maxwellian velocities distribution.

In fig. 4 is represented a probe characteristic resulted from experiment as well as the logarithmic characteristic of the electron current.

Although the same mobile cylindrical probe was placed at about the same distance for the cathode, as in the case of hydrogen, the plasma parameters as well as their variation along the negative column differ from those obtained under similar experimental conditions in hydrogen.

From tables 4, 5 and 6, as well as from fig. 7, where the kinetic average energy of the first electron group is represented as a function of the cathode

TABLE 4

I = 2,72 mA p = 0,46 torr

d_{cm}	T_i^- °K	W_i^- eV	N_i^-	T_2^- °K	W_2^- eV	N_2^-
0,7	26 670	3,5	$2{,}56 \cdot 10^6$	57 200	7,3	$3{,}2 \cdot 10^6$
1,5	34 537	4,4	$9{,}64 \cdot 10^5$	63 800	8,2	$2{,}1 \cdot 10^6$
1,8	38 142	4,9	$1{,}29 \cdot 10^6$	17 192	2,2	$7{,}02 \cdot 10^6$
2,2	42 280	5,4	$1{,}02 \cdot 10^6$	38 142	4,9	$1{,}01 \cdot 10^7$
3,1	49 604	5,9	$1{,}96 \cdot 10^6$	19 071	2,4	$1{,}7 \cdot 10^7$
4,1^{4}	52 469	6,4	$7{,}84 \cdot 10^5$	24 280	3,1	$1{,}81 \cdot 10^7$
6,2	45 864	5,9	$1{,}8 \cdot 10^6$	59 670	7,7	$1{,}08 \cdot 10^7$
7,2	53 400	6,9	$1{,}87 \cdot 10^6$	61 027	7,8	$7{,}24 \cdot 10^6$
8,2	53 460	6,94	$7k2 \cdot 10^6$	72 600	9,3	$1{,}06 \cdot 10^7$
9	61 190	7,8	$1{,}8 \cdot 10^6$	78 100	10,3	$2{,}28 \cdot 10^7$
10	68 796	8,8	$9{,}3 \cdot 10^5$	61 027	7,8	$7{,}68 \cdot 10^6$
11	76 401	9,8	$8{,}1 \cdot 10^5$	45 704	5,9	$3{,}55 \cdot 10^6$
12	80 262	10,3	$7{,}95 \cdot 10^5$	68 656	8,8	$8{,}2 \cdot 10^5$
13	87 984	12,6	$8{,}03 \cdot 10^5$	61 000	7,8	$2{,}9 \cdot 10^6$

TABLE 5

I = 1,81 *mA* p = 0,46 torr

d_{cm}	T_i^- °K	W_i^- eV	N_i^-	T_2^- °K	W_2^- eV	N_2^-
0,7	22 928	2,9	$1{,}81 \cdot 10^6$	95 355	12,3	$2 \cdot 10^6$
1,5	34 393	4,5	$1{,}28 \cdot 10^6$	24 032	3,1	$5{,}25 \cdot 10$
3,1	45 486	5,8	$8{,}36 \cdot 10^5$	36 800	4,6	$1{,}69 \cdot 10^7$
4,1	53 479	6,4	$1{,}30 \cdot 10^6$	35 864	4,6	$1{,}84 \cdot 10^7$
6,2	49 608	6,6	$3{,}43 \cdot 10^6$	54 814	7,08	$6{,}68 \cdot 10^6$
7,2	51 596	6,8	$9{,}45 \cdot 10^5$	61 600	7,7	$3{,}62 \cdot 10^6$
8,2	53 461	6,9	$4{,}27 \cdot 10^6$	76 200	9,8	$9{,}68 \cdot 10^6$
9	61 776	9	$1{,}99 \cdot 10^6$	30 351	3,9	$7{,}22 \cdot 10^6$
10	69 900	8	$2{,}89 \cdot 10^6$	53 400	6,8	$1 \cdot 10^7$
11	76 248	9,8	$1{,}22 \cdot 10^6$	91 280	11,7	$2{,}75 \cdot 10^6$
12	76 401	9,8	$1{,}55 \cdot 10^6$	76 248	9,8	$1{,}07 \cdot 10^7$
13	53 469	6,9	$1\ 24 \cdot 10$	68 656	9,8	$1{,}03 \cdot 10^7$
14	80 362	10,6	$1{,}74 \cdot 10^6$	72 600	9,3	$1{,}34 \cdot 10^7$

TABLE 6

I = 1,09 *mA* p = 0,46 torr

d_{cm}	T_i^- °K	W_i^- eV	N_i^-	T_2^- °K	W_2^- eV	N_2^-
0,7	30 537*M*	3,8	$1{,}18 \cdot 10^6$	47 300	6,1	$5{,}1 \cdot 10^6$
1,5	57 330	7,4	$1{,}73 \cdot 10^6$	88 500	11	$3 \cdot 10^6$
1,8	30 537	3,8	$3{,}36 \cdot 10^6$	38 600	4,9	$1{,}18 \cdot 10^7$
2,2	44 460	5,7	$1{,}13 \cdot 10^6$	64 900	8,3	$2{,}02 \cdot 10^6$
3,1	53 390	6,9	$9{,}7 \cdot 10^5$	38 102	4,9	$1{,}7 \cdot 10^7$
6,2	65 052	8,4	$9{,}32 \cdot 10^5$	42 380	5,4	$4{,}36 \cdot 10^6$
7,2	76 248	9,8	$7{,}45 \cdot 10^5$	68 756	8,8	$1{,}64 \cdot 10^7$
8,2	64 935	8,3	$1{,}4 \cdot 10^6$	76 280	9,9	$6{,}48 \cdot 10^6$
9	76 400	9,92	$8{,}1 \cdot 10^5$	99 069	12,7	$7{,}45 \cdot 10^6$
10	76 050	9,8	$6{,}48 \cdot 10^5$	57 213	7,3	$9{,}53 \cdot 10^6$
11	7 5933	9,8	$1{,}6 \cdot 10^7$	54 770	5,8	$4{,}4 \cdot 10^6$
12	64 735	8,3	$2{,}9 \cdot 10^6$	60 100	7,7	$9{,}33 \cdot 10^6$
13	61047	7,9	$9{,}54 \cdot 10^5$	72 600	9,2	$5{,}4 \cdot 10^6$

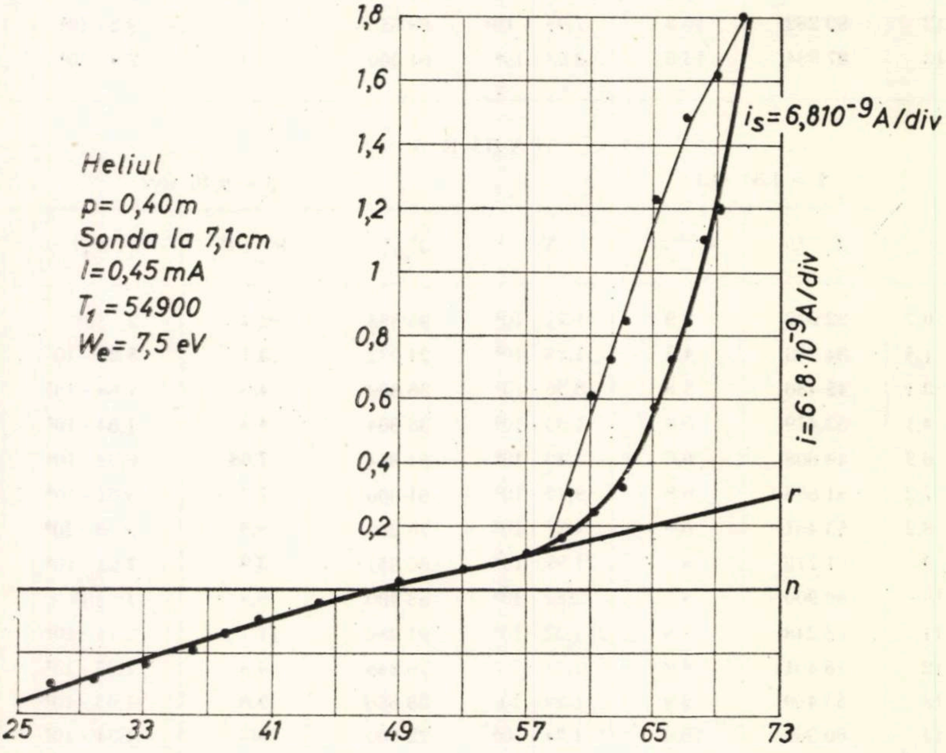

Fig. 7

distance, for the three current we worked at, the following facts were established:

This electron group enters the Crookes space with an average kinetic energy of about 3 *eV*, which continuously grows as the distance from the cathode increases, becoming about three times higher at the beginning of the positive column. To calculate the second electron group temperature both calculation methods were used.

In fig. 8 and 9 the average kinetic energy and the concentration of each electron group are represented as a function of the probe position from

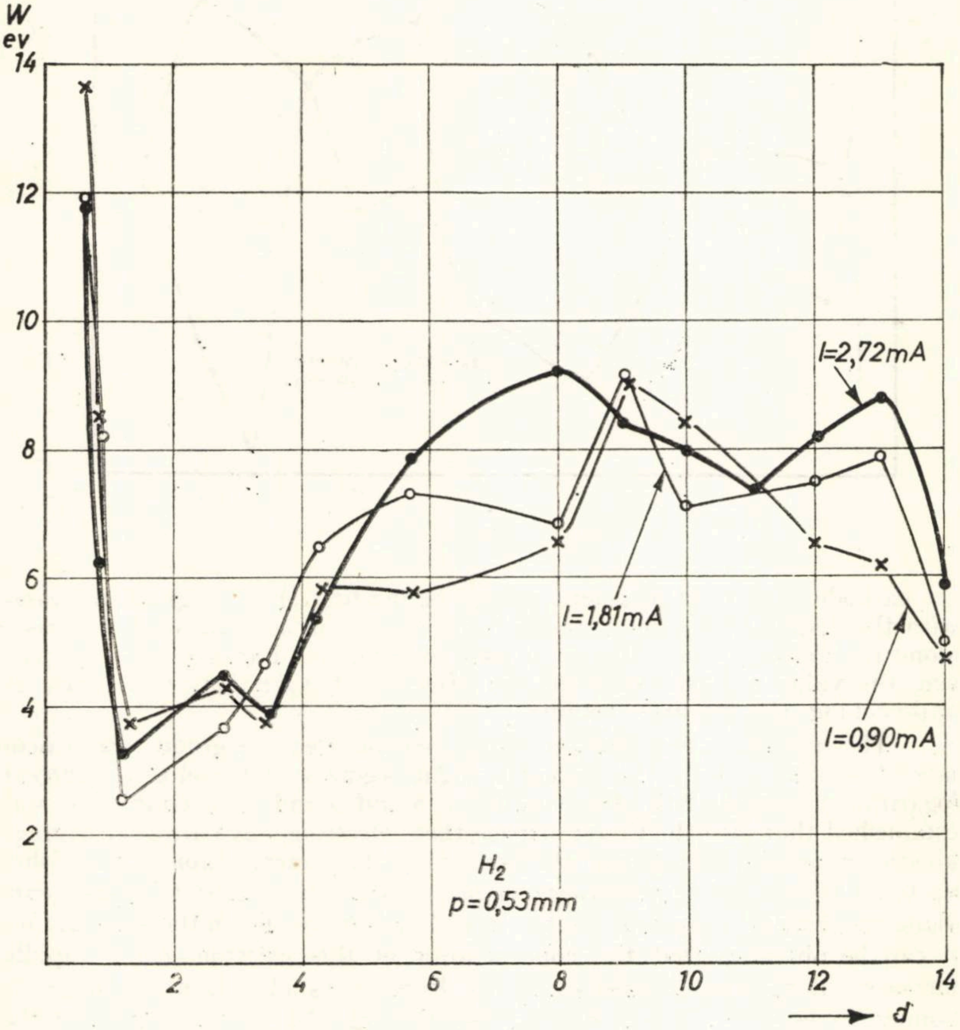

Fig. 8.

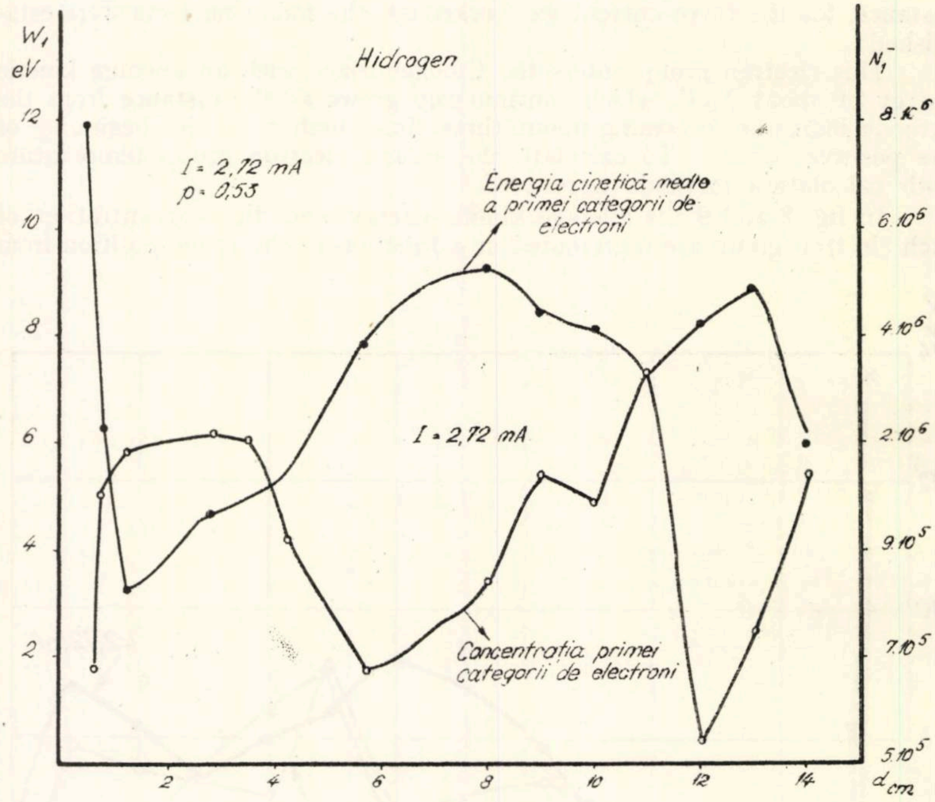

Fig. 9

the cathode. The average kinetic energy of the first electron group increases with the distance from the cathode but the electron concentration decreases along the Crookes space to grow briskly entering the Faraday space surpassing the value near the cathode and after slight variations to decrease as approaching the positive column.

The average kinetic energy of the second electron group, was calculated from the slope of the second straight segment of the electron current logarithmic characteristic. From tables 4, 5 and 6 and from Graph 9 it was established that into the Crookes space these electrons have a higher average kinetic energy then those from the first group. This energy rapidly diminishes up to *the immediate neighbourhood of the* negative boundary to grow again along the Faraday space for excitation and ionisations. From the same graphs it can be observed that the concentration of this electron group rapidly increases along the Crookes space, to decrease rapidly after the negative boundary, especially when the current through the tube is high and the distance from the positive column is short.

In this case too, it was established that the maximum concentration of the first electron group coincides with the position of the second electron group minimum.

3. ARGON

Since, for the same gas pressure the positive column of an electrical discharge in argon is much longer than in hydrogen or oxygen, in order to use the same discharge tube and the annex installations, the probe characteristics were taken at 0.15 and 0.2 torr, beginning immediately after the negative boundary up to the cathodic edge of the positive column.

The electron current logarithmic characteristics were always straight lines made of three straight segments and it was admitted the existence of three electron groups with maxwellian velocity distribution. The current through the tube was 0.22 *mA*, 0.44 *mA* or 0.66 *mA*, corresponding at 0.011 *mA*/cm², 0.022 *mA*/cm² and 0.033 *mA*/cm² current densities respectively.

In fig 5 is represented a probe characteristic picked up from experiment.

From tables 7, 8 and 9 and fig. 10 it was established that for the same gas pressure and discharge current, the average kinetic energy of the first electron group very rapidly increases when the probe is moving off from the cathode. So that when the current through the tube was 0.22 mA, the

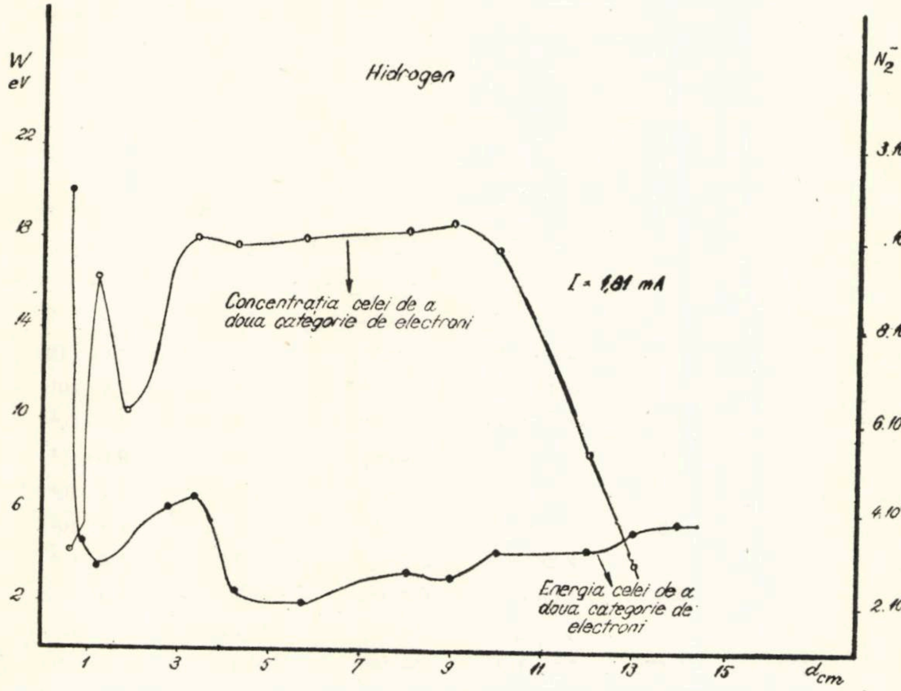

Fig. 10

TABLE 7

$I = 0{,}2$ *mA* $p = 0{,}15$ torr

d_{cm}	T_i^- °K	W_i^- eV	N_i^-	T_2^- °K	W_2^- eV	N_2^-
I	23 400	3	$3{,}7 \cdot 10^5$	73 700	9,52	$7{,}53 \cdot 10^5$
1,9	25 740	3,3	$,17 \cdot 10^5$	35 100	4,2	$5{,}94 \cdot 10^5$
2,9	31 590	4,2	$2{,}46 \cdot 10^5$	54 990	7,5	$7{,}44 \cdot 10^5$
3,9	39 078	5,05	$2{,}88 \cdot 10^5$	93 600	12	$7{,}5 \cdot 10^5$
5	50 661	6,5	$1{,}35 \cdot 10^5$	101 790	13	$2{,}95 \cdot 10^5$
5,8	62 680	8,08	$1{,}06 \cdot 10^5$	152 000	19	$2{,}24 \cdot 10^5$
6,8	78 039	10	$8{,}99 \cdot 10^4$	194 220	25	$2{,}3 \cdot 10^5$
7,8	84 310	10,9	$7{,}89 \cdot 10^4$	159 120	20,5	$2{,}26 \cdot 10^5$
9	96 910	12	$7 \cdot 10^4$	163 800	21	$2{,}1 \cdot 10^5$
10	97 110	12,5	$8{,}1 \cdot 10^4$	194 922	25,1	$2{,}8 \cdot 10^5$
11	70 200	9,07	$8{,}58 \cdot 10^4$	187 200	24	$2{,}7 \cdot 10^5$

TABLE 8

$I = 0{,}45$ *mA* $p = 0{,}15$ torr

d_{cm}	T_i^- °K	W_i^- eV	N_i^-	T_2^- °K	W_2^- eV	N_2^-
I	10 671	1,3	$3{,}38 \cdot 10^5$	33 010	4,4	$8{,}8 \cdot 01^5$
1,9	11 700	1,5	$4{,}3 \cdot 10^5$	19 870	2,5	$9{,}01 \cdot 10^5$
2,9	15 678	2	$2{,}44 \cdot 10^5$	35 100	4,5	$7{,}6 \cdot 10^5$
3,9	19 890	2,6	$1{,}9 \cdot 10^5$	43 290	5,5	$8{,}7 \cdot 10^5$
5	35 100	4,5	$3{,}4 \cdot 10^5$	78 039	10,8	$9{,}9 \cdot 10^5$
5,8	38 961	5	$1{,}76 \cdot 10^5$	90 090	11,6	$6{,}1 \cdot 10^5$
6,8	49 680	6,5	$1 \cdot 10^5$	132 210	17	$1{,}6 \cdot 10^5$
7,8	58 500	7,5	$8{,}28 \cdot 10^4$	137 400	17,7	$4{,}6 \cdot 10^5$
9	66 090	8,5	$1{,}08 \cdot 10^5$	145 300	18,7	$5{,}01 \cdot 10^5$
10	77 220	9,9	$1{,}4 \cdot 10^5$	194 700	25,1	$3{,}2 \cdot 10^5$
11	70 200	0,97	$7{,}2 \cdot 10^4$	128 700	16,6	$1{,}69 \cdot 10^5$

TABLE 9

I = 0,66 *mA* p = 0,15 torr

d_{cm}	T_i^- °K	W_i^- eV	N_i^-	T_2^- °K	W_2^- eV	N_2^-
I	7 722	0,99	$2{,}5 \cdot 10^5$	17 750	2,2	$5{,}2 \cdot 10^5$
1,9	9 691	1,2	$4{,}2 \cdot 10^5$	29 250	3,7	$8{,}1 \cdot 10^5$
2,9	11 700	1,5	$5{,}2 \cdot 10^5$	35 100	4,2	$1{,}44 \cdot 10^6$
3,9	14 040	1,8	$1{,}84 \cdot 10^5$	19 890	2,5	$7{,}4 \cdot 10^5$
5	25 940	3,3	$2{,}2 \cdot 10^5$	58 500	7,5	$1{,}04 \cdot 10^6$
6,8	46 800	6	$1{,}6 \cdot 10^5$	117 000	15,2	$2{,}92 \cdot 10^5$
7,8	58 500	7,5	$1{,}1 \cdot 10^5$	150 000	19	$1{,}79 \cdot 10^5$
9	70 200	9,07	$1{,}006 \cdot 10^5$	165 000	21,3	$2{,}6 \cdot 10^5$
10	70 200	9,07	$1{,}32 \cdot 10^5$	162 800	21	$6{,}9 \cdot 10^5$
11	77 970	10	$1{,}5 \cdot 10^5$	160 600	20,7	$4{,}9 \cdot 10^5$

electrons of the first group entered the Crookes space with an average energy of about 3 *eV*, to reach 12.5 *eV* at the beginning of the positive column.

The average kinetic energy of the second electron group, calculated from the slope of the second straight segment of the electron current logarithmic characteristic, is always higher than that of the first group. After a slight diminution at the beginning of Crookes space, increases with the probe distance from the cathode.

The minimum of the electron average kinetic energy corresponds with the position of the maximum concentration of this electron group.

In fig. 12 and 13 the concentration values of the two electron groups are presented as a function of the distance from the cathode for the three currents we worked at. It can be observed that for the same probe position from the cathode, the concentration of the first electron group grows as the discharge current increases. For the same current through the tube, at the beginning of the Faraday space the concentration of this electron group si almost constant, then diminishes with the distance from the cathode.

The concentration maxima of the first electron group coincide in this case too with the position of the second electron group minimum concentration.

4. HELIUM

The same installation was used. Hellium pressure was 0.4 torr. The probe characteristics were drawn up beginning from the negative boundary up to the cathodic edge of the positive column. The discharge currents of 0.22 *mA*, 0,45 *mA* and 0.68 *mA* we worked at, correspond to 0.0011 *mA* cm², 0.022 *mA*/ /cm² and 0.034 *mA*/cm² current densities respectively.

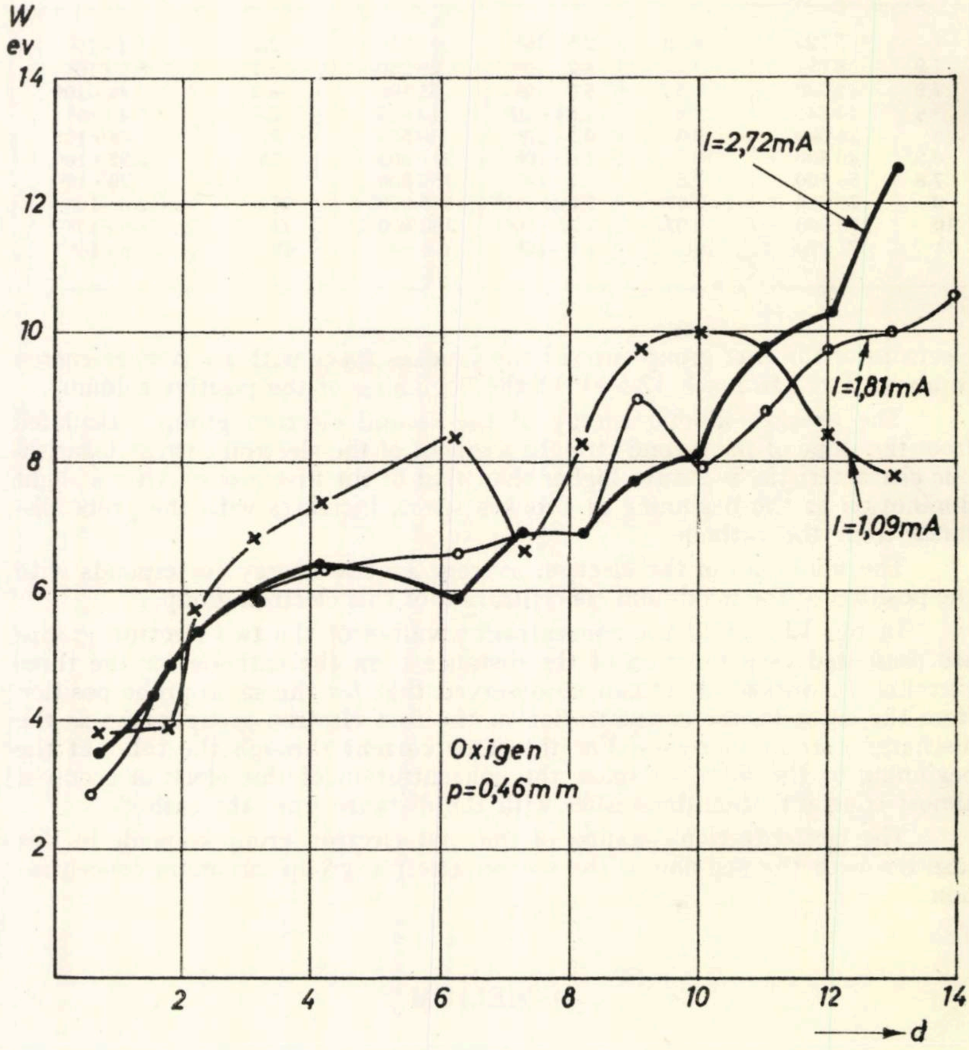
W
ev
14
12
10
8
6
4
2
2
4
6
8
10
12
14
d
I=2,72mA
I=1,81mA
I=1,09mA
Oxigen
p=0,46mm

Fig. 11

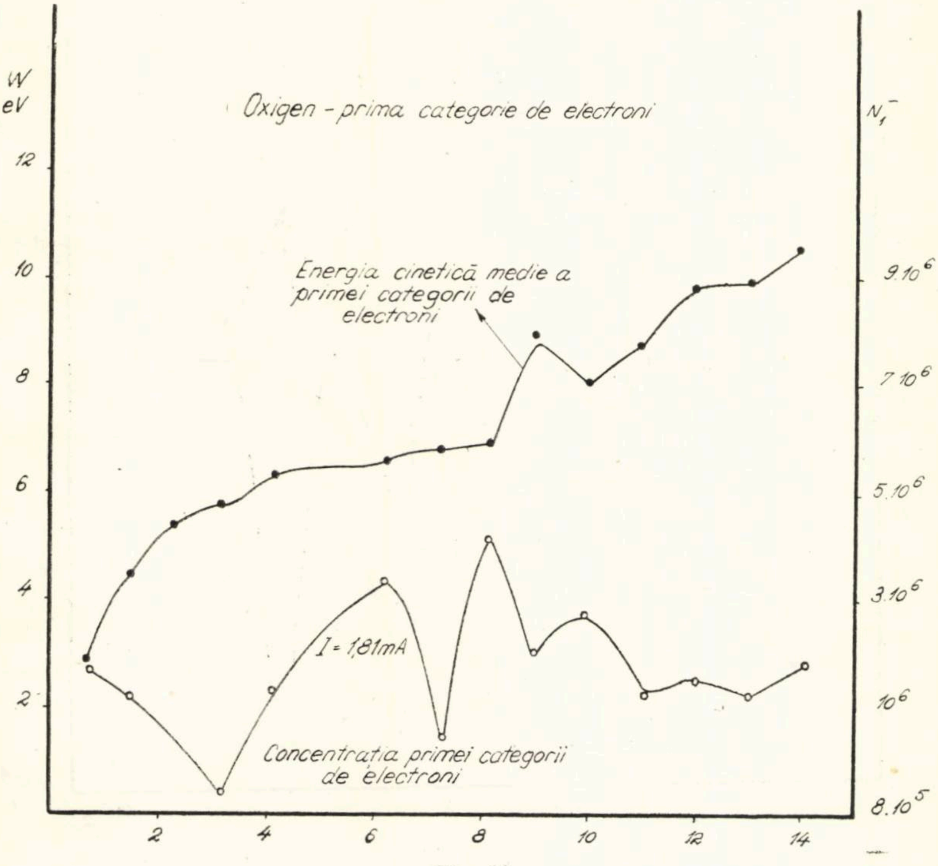
W
eV
Oxigen - prima categorie de electroni
N_1^-
12
10
8
6
4
2
Energia cinetică medie a primei categorii de electroni
9.10^6
7.10^6
5.10^6
3.10^6
10^6
8.10^5
I = 1,81mA
Concentrația primei categorii de electroni
2
4
6
8
10
12
14

Fig. 12

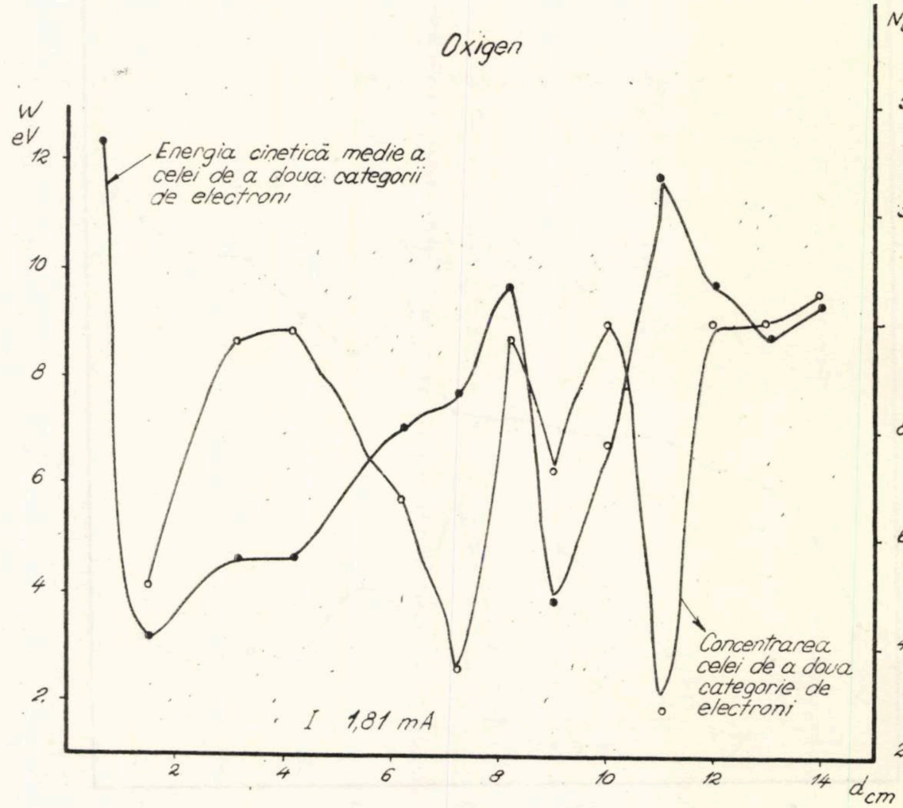
Oxigen
W eV
12
10
8
6
4
2.
Energia cinetică medie a celei de a doua categorii de electroni
N_e^-
5.10⁷
3.10⁷
10⁷
8.10⁶
6.10⁶
4.10⁶
2.10⁶
Concentrarea celei de a doua categorie de electroni
I 1,81 mA
2
4
6
8
10
12
14
d_{cm}

Fig. 13

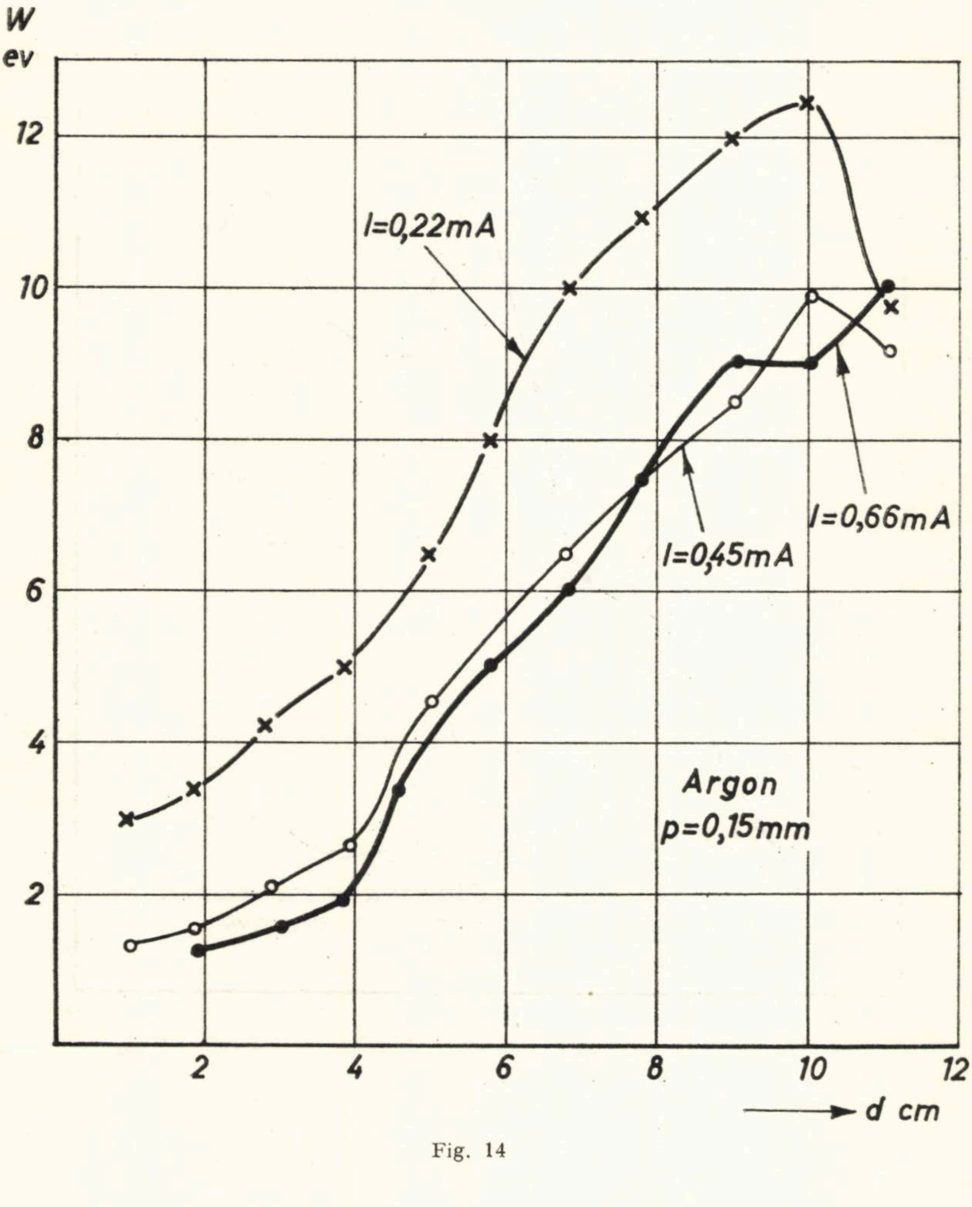
W
ev
12
10
8
6
4
2
2
4
6
8
10
12
d cm
I=0,22mA
I=0,45mA
I=0,66mA
Argon
p=0,15mm

Fig. 14

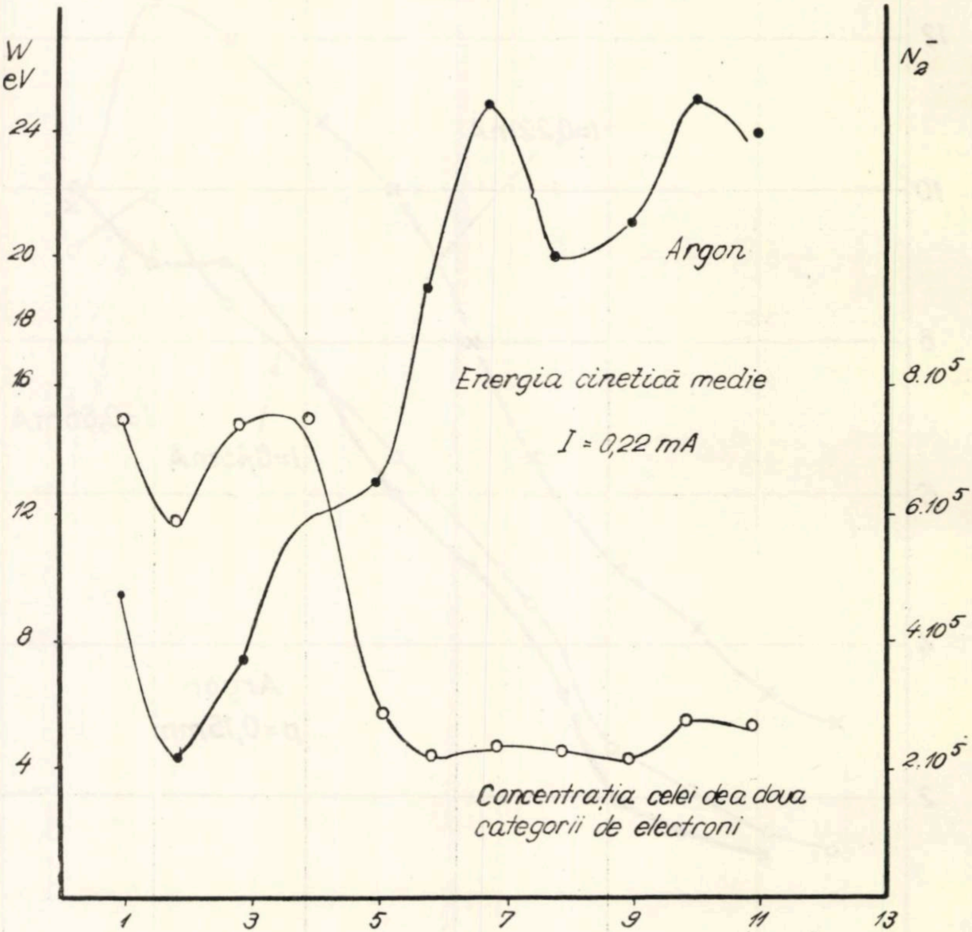
W
eV
24
20
18
16
12
8
4
N₂⁻
8.10⁵
6.10⁵
4.10⁵
2.10⁵
Argon
Energia cinetică medie
I = 0,22 mA
Concentrația celei de a doua categorii de electroni
1
3
5
7
9
11
13
d cm

Fig. 15

The electron current larithmic chogaracteristics were always straight lines with two bend points and it was admitted the existence of three electron groups in an about 1 cm interval situated at the beginning of the Faraday space.

In the rest of the space between the negative boundary and the negative part of the positive column these characteristics presented one bend point proving the existence of two electron groups only.

In fig. 6 and 7 two probe characteristics are presented as well as the electron current logarithmic one for the case when the probe was placed at 7.1 cm or 4.1 cm distance from the cathode.

Using Medicus graphic method, the probe experimental characteristic was twice differentiated for the case when the probe was at 1.2 cm from the cathode.

The current through the tube was 0.45 *mA* and a distribution like in fig. 8 was obtained, i.e. an electron group only.

The same method used to analyse the data corresponding to fig. 6i gves a distribution like in fig. 9, where the secondary and slow electron groups can be observed.

In tables 10, 11 and 12 are presented the values calculated according to Langmuir relations; electron temperatures, their average kinetic energy and their concentration.

In fig. 14 is represented the average kinetic energy as a function of the distance from the cathode for the three currents we worked at. It can be seen that the electrons reach the negative boundary with an average kinetic energy

TABLE 10

$I = 0{,}22\ mA$ $P = 0{,}40$ trorr

d_{cm}	T_1^- °K	W_i^- eV	N_i^-	T_2^- °K	W_2^- eV
1	85 410	11	$1{,}2 \cdot 10^5$	159 120	20,5
1,5	74 061	9,8	$8{,}48 \cdot 10^4$	132 200*M*	17
2,1	70 100	9	$1{,}5 \cdot 10^5$	117 000	15,1
3	67920	8,7	$1{,}83 \cdot 10^5$	152 100	19,6
4,1	70 200	9,07	$1{,}14 \cdot 10^5$	132 210	17
5,1	78 390	10	$1{,}8 \cdot 10^5$	93 600	12
7,1	54 990	7,1	$2{,}7 \cdot 10^5$	77 922	10
8,1	52 261	7,7	$8{,}7 \cdot 10^5$	95 600	12,3
9,1	46 800	6	$5{,}2 \cdot 10^5$	85 410	11
10	50 720	6,5	$6{,}36 \cdot 10^5$	109 161	14
11	54 990	7,8	$2{,}97 \cdot 10^5$	97 461	12,5
12	54 070	7,1	$5{,}23 \cdot 10^5$	124 190	16,4
13	42 120	5,4	$4{,}02 \cdot 10^5$	108 110	13,9
14,1	53 000	6,9	$2{,}4 \cdot 10^5$	101 790	13,1
15	59 610	7,7	$3{,}5 \cdot 10^5$	132 561	17,1
16	62 010	8,01	$2{,}7 \cdot 10^5$	155 610	20
17	86 590	11	$2{,}07 \cdot 01^5$	187 200	24,3

TABLE 11

I = 0,45 *mA* $p = 0{,}40$ torr

d_{cm}	T_i^- °K	W_i^- eV	N_i^-	T_2^- °K	W_2^- eV
I	90 090	11,6	$9{,}67 \cdot 10^4$	163 800	21,1
1,5	78 030	10	$1 \cdot 10^5$	117 000	15,1
2,1	62 361	8,05	$2{,}4 \cdot 10^5$	124 020	16
3	54 222	7,04	$2{,}24 \cdot 10^5$	125 190	16,1
4,1	56 160	7,25	$1{,}39 \cdot 10^5$	108 810	14
4,8	58 500	7,5	$1{,}8 \cdot 10^5$	107 110	13,7
5,1	62 600	8,02	$1{,}7 \cdot 10^5$	148 590	19,1
7,1	54 900	7,09	$4{,}83 \cdot 10^5$	85 410	11
8,1	56 511	7,3	$3{,}29 \cdot 10^5$	70 200	9,03
9,1	50 778	6,5	$9{,}6 \cdot 10^5$	109 161	14
10	50 661	6,5	$9{,}84 \cdot 10^5$	100 620	13
11	54 990	7,1	$9{,}85 \cdot 10^5$	107 810	13,9
12	58 500	7,5	$9{,}9 \cdot 10^5$	128 700	16,6
13	46 800	6,04	$1{,}06 \cdot 10^6$	132 210	17
14	47 000	6,1	$6{,}6 \cdot 10^5$	108 810	14
15	50 310	6,5	$7{,}7 \cdot 10^5$	101 434	13
16	52 650	6,8	$9{,}5 \cdot 10^5$	125 190	16,1
17	54 990	7	$3{,}7 \cdot 10^5$	117 200	15,1
18	62 080	8,01	$3{,}8 \cdot 10^5$	140 040	18

TABLE 12

I = 0,68 *mA* p = 0,40 torr

d_{cm}	T_i^- °K	W_i^- eV	N_i^-	T_2^- °K	W_2^- eV
1	85 450	11,03	$1{,}95 \cdot 10^5$	128 700	16,6
1,5	81 900	10,6	$2{,}1 \cdot 10^5$	140 000	18,1
2,1	78 039	10	$2 \cdot 10^5$	152 210	19,6
3	54 490	7,04	$2{,}05 \cdot 10^5$	179 010	23,1
4,1	50 661	6,5	$2{,}8 \cdot 10^5$	101 322	13
4,8	55 000	7,1	$1{,}86 \cdot 10^5$	101 300	13
5,1	54 639	7,05	$2{,}05 \cdot 10^5$	132 210	17
7,1	46 800	6,04	$2{,}01 \cdot 10^5$	70 200	9,07
8,1	49 140	6,3	$8{,}3 \cdot 10^5$	62 478	8,07
9,1	54 900	7,1	$1{,}24 \cdot 10^5$	70 200	9,07
10	58 500	7,5	$3{,}6 \cdot 10^5$	78 039	10,8
11	50 100	6,4	$7{,}8 \cdot 10^5$	73 710	9,4
12	62 000	8	$3{,}35 \cdot 10^5$	72 540	9,3
13	62 360	8,05	$8{,}7 \cdot 10^7$	125 190	16,1
14	60 840	7,8	$8{,}8 \cdot 10^5$	101 320	13
15	55 000	7,1	$6{,}8 \cdot 10^5$	93 600	12,09
16	58 500	7,5	$7{,}5 \cdot 10^5$	102 960	13,3
17	59 100	7,6	$7{,}2 \cdot 10^5$	105 300	13,6
18	64 390	8,3	$5{,}1 \cdot 10^5$	101 740	13,1

of 11 *eV*. This energy diminishes up to about 7 eV at the beginning of the Faraday space because of the inelastic collisions. In the interval where the other electron group appeared a kinetic energy growth of about 1 eV was observed after which the energy briskly diminishes directly with the diminishing of the electric current through the tube.

The energy of the second electron group calculated from the slope of the second straight segment of the electron current characteristic is always higher than the average kinetic energy of the first electron group.

In fig. 15 is presented the average kinetic energy and concentration of the first electron group as a function of the distance from the cathode for a 0.68 mA discharge current.

It can be observed that if into the Crookes space the electron density is about constant, the electron average energy rapidly diminishes to remain about constant along the Faraday space whereas the concentration presents very pointed maxima and minima.

The second electron group energy rapidly increases into the Crookes space, presents a maximum in the negative boundary to diminish briskly at the beginning of Faraday space.

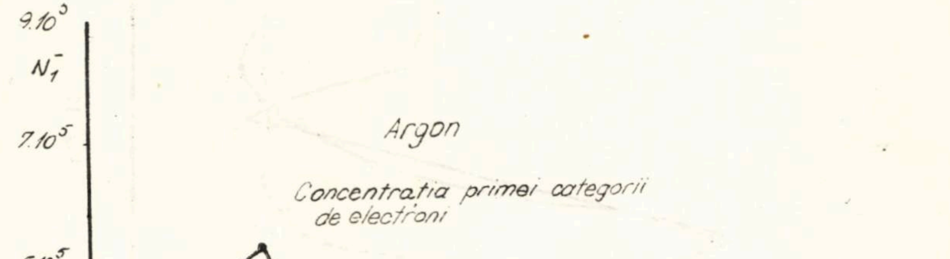

Fig. 16

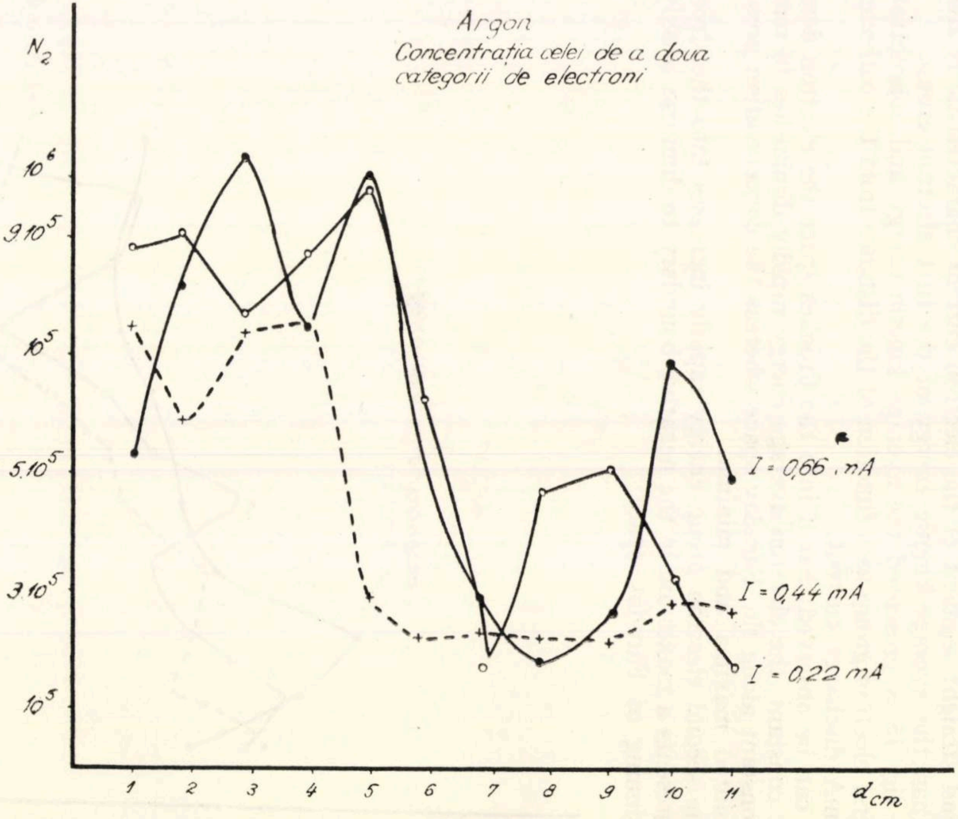
Argon
Concentrația celei de a doua categorii de electroni
N₂
10⁶
9.10⁵
10⁵
5.10⁵
3.10⁵
10⁵
I = 0,66 mA
I = 0,44 mA
I = 0,22 mA
1
2
3
4
5
6
7
8
9
10
11
d cm

Fig. 17

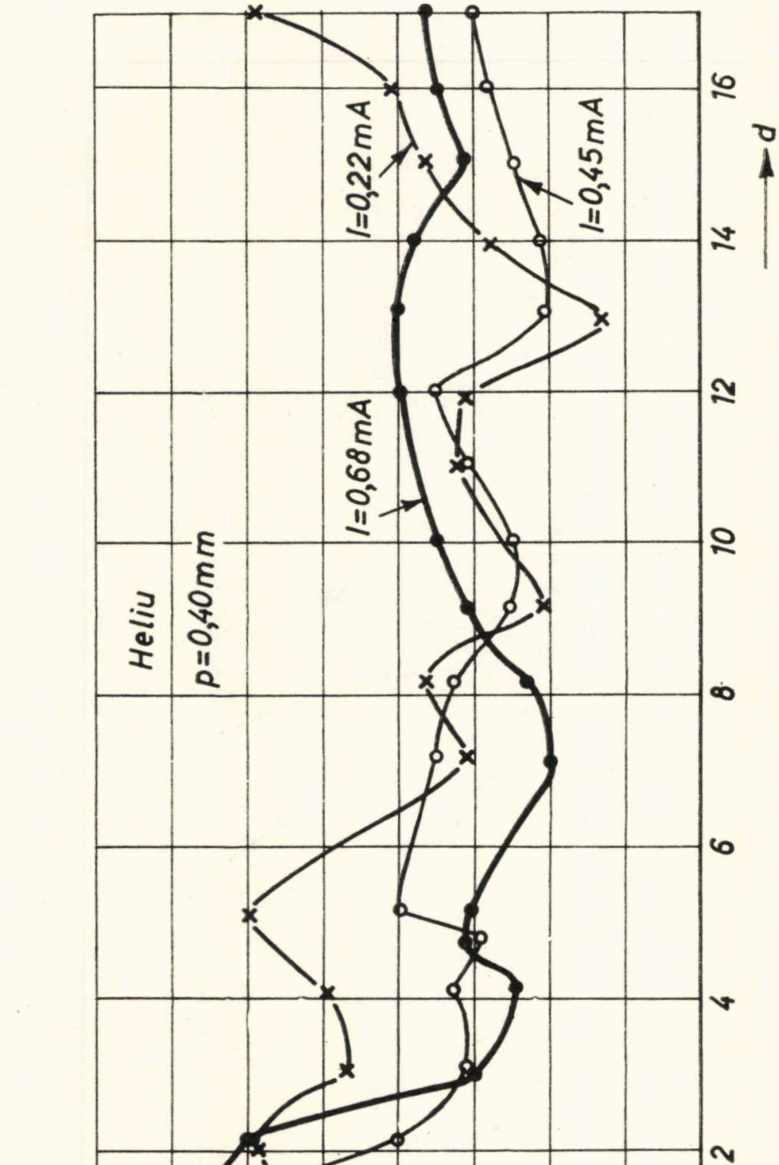
W
ev
11
9
7
5
2
4
6
8
10
12
14
16
d
Heliu
p=0,40mm
I=0,68mA
I=0,22mA
I=0,45mA

Fig. 18

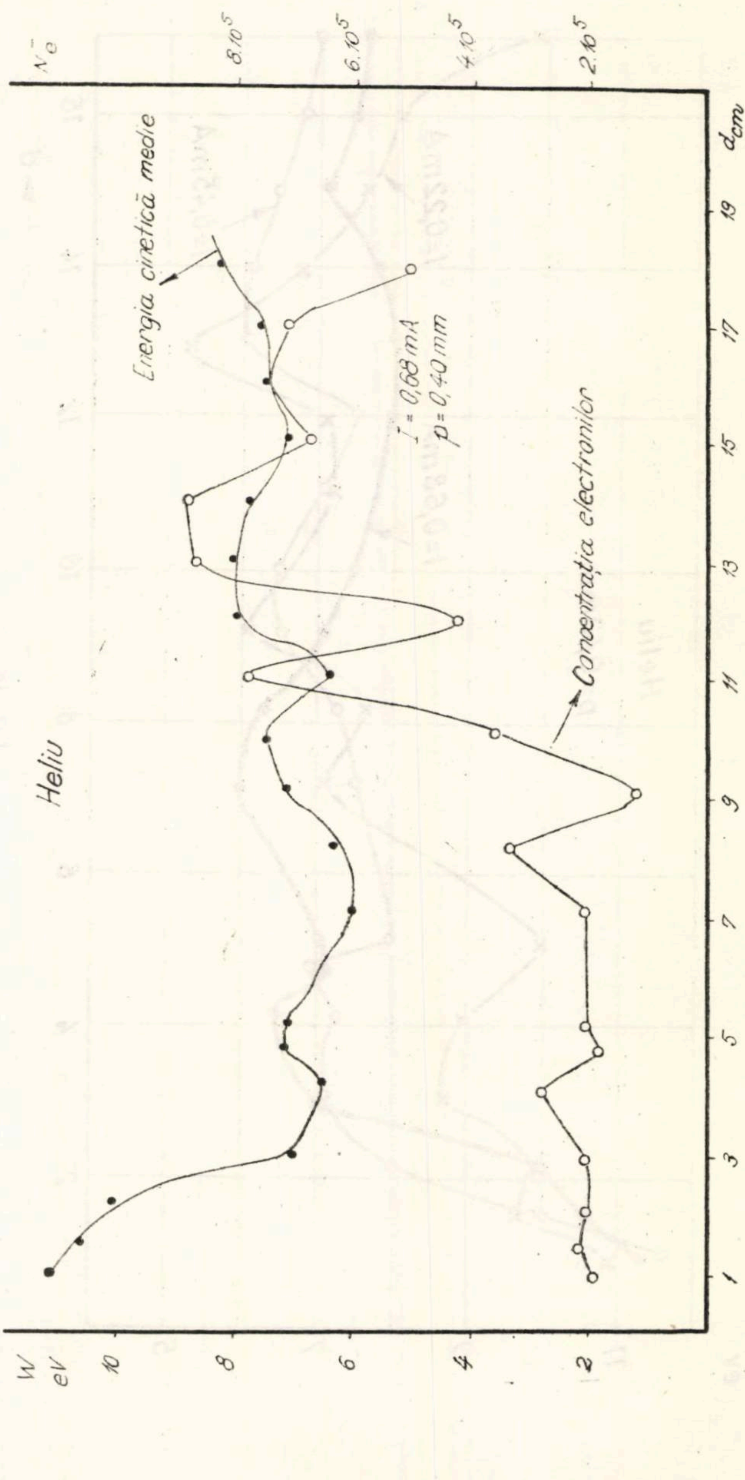
Heliu
Energia cinetică medie
Concentrația electronilor
I = 0,68 mA
p = 0,40 mm
W
eV
10
8
6
4
2
N_e^-
8.10⁵
6.10⁵
4.10⁵
2.10⁵
d_{cm}
1
3
5
7
9
11
13
15
17
19

Fig. 19

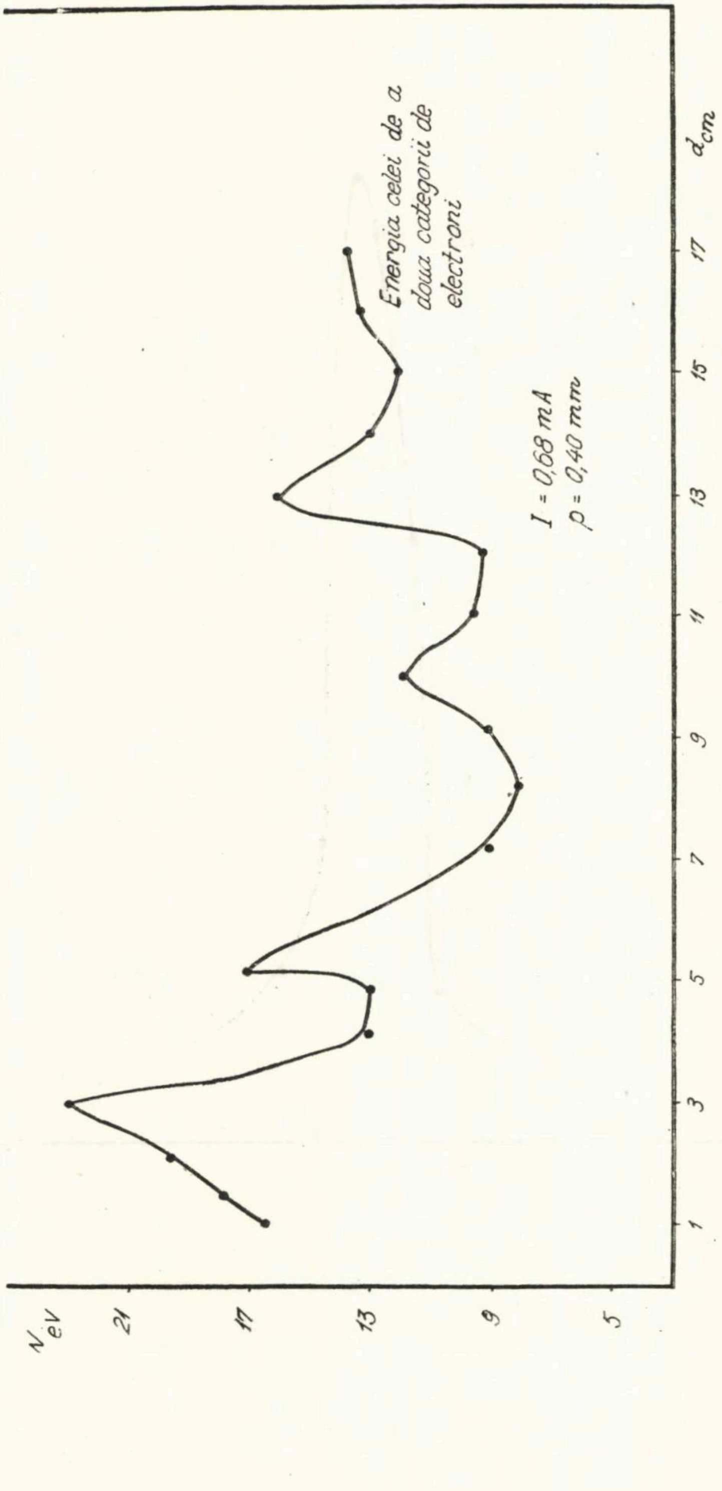
V_{eV}
21
17
13
9
5
d_{cm}
1
3
5
7
9
11
13
15
17
Energia celei de a doua categorii de electroni
I = 0,68 mA
p = 0,40 mm

Fig 20

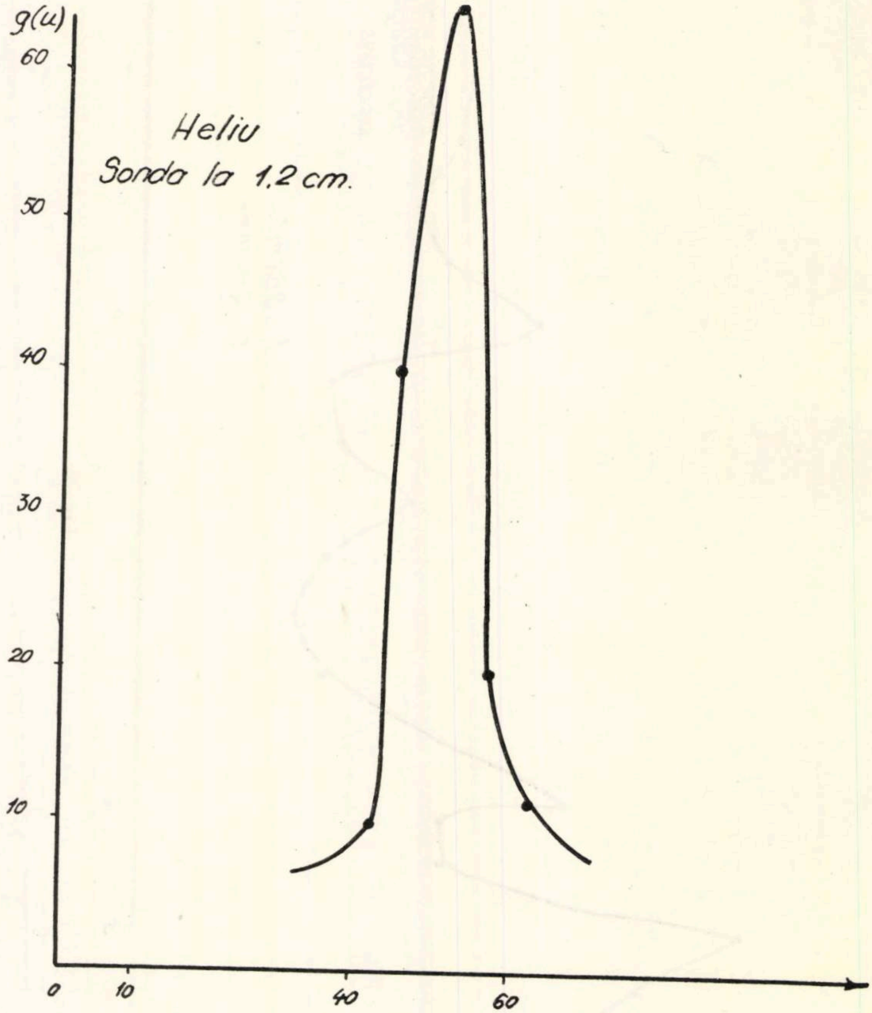

Fig. 21

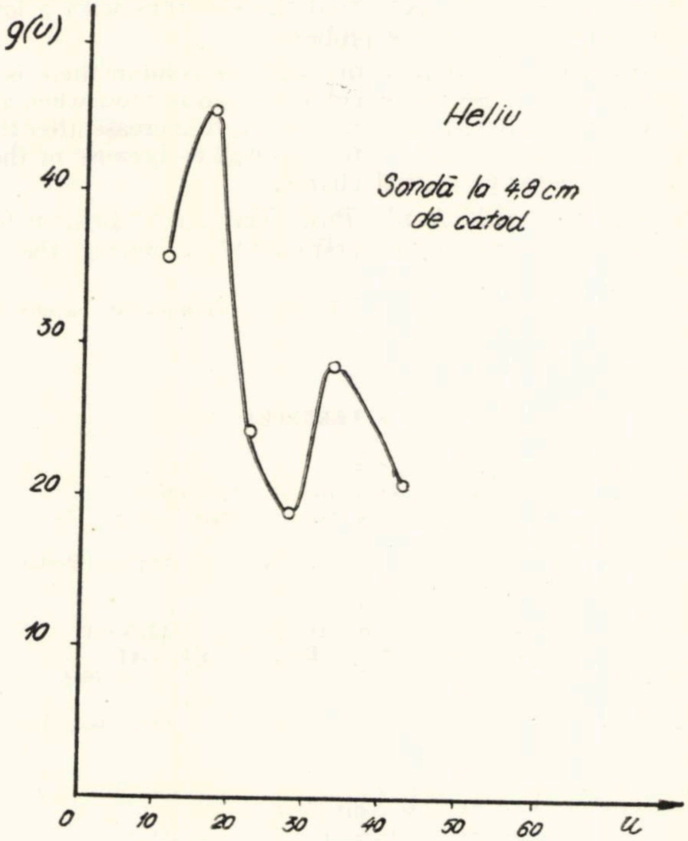

SUMMARY AND CONCLUSIONS

The measurements with Langmuir probe in the space from the cathode and positive column of a normal discharge at low pressure in hydrogen, oxygen, argon and in a certain interval in Helium too, have shown a deviation of the electron velocities distribution from the simple maxwellian distribution.

The observed distribution can be interpreted as a product of three electron maxwellian distributions with different temperatures.

The intensit yof the electron current is given by the product of the electron densities corresponding to these groups.

The calculated temperature of the two groups mainly depends on the gas nature.

At high probe negative potentials, the probe electron current is produced by high energy electrons (first group). By increasing the probe potential (for certain values of this potential) the electrons with a lower energy (second group) begin to reach the probe.

It was established too that in the negative column there is a negative gradient of potential, because the potential instead to grow when approaching the anode is decreasing along a certain interval, to increase after that because the electrons move under the field action, as well as because of the diffusion, thus forming so a negative spatial charge.

I would like to thank Acad. Prof. Theodor V. Ionescu for the help granted, for the discussions and suggestions given during the experiment

University of Bucarest, Faculty of Physics

REFERENCES

I. Langmuir, Phys. Rev. 26. 585, (1925)
I. Langmuir, H. Mott-Smith. Phys. Rev. 28. 727. 1926
K. Compton a. J. Langmuir, Electrical discharges in Gases. Rev. of. Mod. Phys. t. II. p. 221 1930
Engel u. Steenbeck, Elektrisce Gasentladungen, J. Springer, Berlin, 1933
G. Medicus, J. Appl. Phys. 27. 10, 1956
M. J. Druyvestein Z. Phys. 64. 790. 1930
F. W. Crawford a. Freeston VI Conf. Int. D. Ion. Gas. I. 1963 461
Schonhuber M. J. Z. Angew. Physic. Rev. 55. 1939. 1161
I. Paulus und I. Schott. Ann. d. Physick. 7. B. 17. H. 5–6. 1966
R. L. F. Boyd, proc. Phys. Soc. (London) B64, 795 (1951)
J. E. Allen, R. L. F. Boyd, and Reynolds, Proc. Phys. Soc. (London) B70, 297 (1955)
J. F. Waymouth, phys. Fluids 7, 1843 (1964)
I. Langmuir, phys. Rev. 33, 954 (1929)
J. F. Waymouth, J. Appl. Phys. 30, 1404 (1959)
F. P. Chen Electric Probes, Plasma diagnostic techniques (1965).
W. Stern, Rev. Roum. d. Phys. 13. 2. (1968)
Emeleus Phyl. Mag. 17. 146. 1934
P. Stiubei, Bul. Științ. Sec. St. Mat. Fiz. T. VII. 2. 1955
R. N. Pârvan Studii și Cercet. de Fizică. 5. Tom. 21. (1969)
Th. V. Ionescu, Ann. Sci. Univ. Iassy, 26. Fasc. I. 225. (1940)

LA LOI DE PROPAGATION DE LA FONCTION DE COHERENCE MUTUELLE GENERALISEE

G. G. BRĂTESCU et T. TUDOR

On montre que la cohérence mutuelle généraliseée, caracterisée par la fonction de corelation de Fischer suit une propagation de type ondulatoire. Les équations de propagation trouvées sont des genéralisations naturelles de celles établies par Wolf pour la fonction $\Gamma_{12}(\tau)$

1. INTRODUCTION

En mettant en discution l'interférence mobile dans le cadre de la théorie de la cohérence partielle, F. Fischer [1] élargit la notion de cohérence, par une généralisation de la fonction de cohérence de Wolf [2]. Vraiment, la fonction de cohérence mutuelle généralisée introduite par Fischer:

$$\Gamma_{12}(\tau, \sigma) = < V_1\left(t + \frac{\tau}{2}\right) V_2^*\left(t - \frac{\tau}{2}\right) e^{2\pi i\sigma t} > \tag{1}$$

à la différence de la fonction de cohérence mutuelle de Wolf

$$\Gamma_{12}(\tau) = < V_1\left(t + \frac{\tau}{2}\right) V_2^*\left(t - \frac{\tau}{2}\right) >. \tag{2}$$

est capable d'indiquer aussi la corrélation des fréquences différentes qui peut être evidenciée par les franges d'interférence mobile — ce qu'on peut voir immédiatement en comparant les valeurs fournies par (1) et (2) dans le cas simple de deux vibrations monochromatiques de fréquence différente.

L'utilité de la définition d'une telle fonction se fait sentir en liaison avec les champs optiques ayant une structure spectrale à part, obtenus, par exemple, par la modulation d'un faisceau lumineux [1,3, 4, 5, etc.]

Utilisant le développement spectral du signal analytique complexe *)

$$V_T(t) = \int_{-\infty}^{\infty} v_T(v)\, e^{-2\pi i \nu t}\, \mathrm{d}\nu \tag{3}$$

Fischer donne le développement spectral de la fonction de cohérence généralise:

$$\begin{aligned}\Gamma_{12}(\tau, \sigma) &= \lim_{T\to\infty} \frac{1}{T} \int_{-\infty}^{\infty} V_{1T}\left(t + \frac{\tau}{2}\right) V_{2T}^{*}\left(t - \frac{\tau}{2}\right) e^{-2\pi i \sigma t}\, dt = \\ &= \lim_{T\to\infty} \frac{1}{T} \int_{-\infty}^{\infty} \left[\int_{-\infty}^{\infty} v_{1T}\left(\nu + \frac{\sigma}{2}\right) e^{-2\pi i\left(\nu + \frac{\sigma}{2}\right)\left(t + \frac{\tau}{2}\right)} d\nu\right] V_{2T}^{*}\left(t - \frac{\tau}{2}\right) e^{-2\pi i \sigma t}\, dt = \\ &= \lim_{T\to\infty} \frac{1}{T} \int_{-\infty}^{\infty} \left[\int_{-\infty}^{\infty} V_{2T}^{*}\left(t - \frac{\tau}{2}\right) e^{-2\pi i\left(\nu - \frac{\sigma}{2}\right)\left(t - \frac{\tau}{2}\right)} d\nu\right] v_{1T}\left(\nu + \frac{\sigma}{2}\right) e^{-2\pi i \nu \tau}\, dt = \\ &= \lim_{T\to\infty} \frac{1}{T} \int_{-\infty}^{\infty} v_{1T}\left(\nu + \frac{\sigma}{2}\right) v_{2T}^{*}\left(\nu - \frac{\sigma}{2}\right) e^{-2\pi i \nu \tau}\, d\nu\end{aligned} \tag{4}$$

Intervertisant la limite avec l'intégrale et faisant la notation:

$$\lim_{T\to\infty} \frac{v_{1T}\left(\nu + \frac{\sigma}{2}\right) v_{2T}^{*}\left(\nu - \frac{\sigma}{2}\right)}{T} = G_{12}(\nu, \sigma), \tag{5}$$

on obtient:

$$\Gamma_{12}(\tau, \sigma) = \int_{-\infty}^{\infty} G_{12}(\nu, \sigma)\, e^{-2\pi i \nu \tau}\, d\nu \tag{6}$$

La densité spectrale de cohérence mutuelle généralisée, $G_{12}(\nu, \sigma)$ montre pour quelles différences de fréquence, σ, existe la corrélation aux deux points du champ optique et comment est distribuée spectralement cette corrélation par les paires de vibrations monochromatiques cohérentes avec les frequences différent par une telle valeur, σ.

Dans ce qui suit, on va montrer que la fonction de cohérence mutuelle généralisée intoduite par Fischer satisfait à des équations de propagation similaires à celles établies par Wolf pour la fonction $\Gamma_{12}(\tau)$.

---

* l'intégrale est élargie par raison de simétrie formelle dans la zone des valeurs négatives de la variable; au fond $v_T(\nu) = 0$ pour < 0

2. LA FORME APPROXIMATIVE DE LA LOI DE PROPAGATION

Dans le développement spectral (4) du signal analytique complexe associé à la perturbation d'un point du champ optique, $v_T(\nu)$ représente l'amplitude complexe du composant monochromatique de fréquence ν du signal. Conformement au principe Huygens-Fresnel, la valeur de celui-ci dans un point quelconque, Q, du champ (fig. 1) s'exprime en fonctione de ses valeurs dans tous les points d'une surface, A, traversée antérieurement par le front d'onde; dans l'énonce de Khirchhoff [6]:

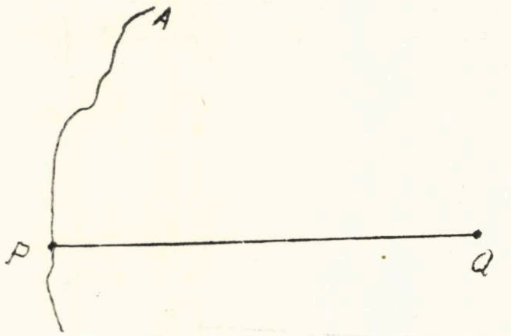

Fig. 1

$$v_T(\nu, Q) = \int_A v_T(\nu, P) \frac{e^{-i\frac{2\pi\nu}{c}\cdot r}}{r} \Lambda(\nu)\, dP. \tag{7}$$

avec: r — distance entre le point Q et le point courant, P, de la surface A

$\Lambda(\nu)$ — le facteur d'inclination, au point P

dP — l'élément de la surface, sur A

La loi de propagation (7) de l'amplitude complexe détermine une loi de propagation correspondante pour la fonction de cohérence mutuelle généralisée:
Soit

$$\Gamma(Q_1, Q_2, \tau, \sigma) = \int_{-\infty}^{\infty} \lim_{T\to\infty} \frac{v_T\left(Q_1, \nu + \frac{\sigma}{2}\right) v_T^*\left(Q_2, \nu - \frac{\sigma}{2}\right)}{T} e^{-2\pi i\nu\tau}\, d\nu \tag{8}$$

la fonction de corrélation de Fischer des perturbations optique de deux points Q_1 et Q_2 (fig. 2). P' et P'' étant deux points courants d'une surface,

A, traversée antérieurement par la lumière, on obtient, en conformité avec (7):

$$v_T\left(\nu+\frac{\sigma}{2},\ Q_1\right)=\int_A v_T\left(\nu+\frac{\sigma}{2},\ P'\right)\frac{e^{-i\cdot\frac{2\pi\left(\nu+\frac{\sigma}{2}\right)}{c}\cdot r'}}{r'}\Lambda'\left(\nu+\frac{\sigma}{2}\right)dP'$$

$$v_T\left(\nu-\frac{\sigma}{2},\ Q_2\right)=\int_A v_T\left(\nu-\frac{\sigma}{2},\ P''\right)\frac{e^{-i\,\frac{2\pi\left(\nu-\frac{\sigma}{2}\right)}{c}\,r''}}{r''}\Lambda''\left(\nu-\frac{\sigma}{2}\right)dP'',$$

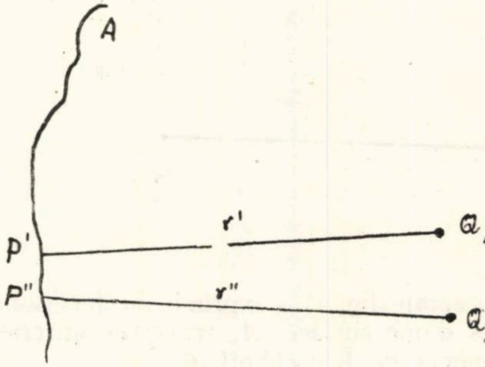

Fig. 2

dont (8) on devient:

$$\Gamma(Q_1,\ Q_2,\ \tau,\ \sigma)=\int_{-\infty}^{\infty}\lim_{T\to\infty}\frac{1}{T}\int_A v_T\left(\nu+\frac{\sigma}{2},\ P'\right)\frac{e^{-i\cdot\frac{2\pi}{c}\left(\nu+\frac{\sigma}{2}\right)r'}}{r'}\cdot{}'\Lambda\left(\nu+\frac{\sigma}{2}\right)dP'\times$$

$$\times\int_A v_T^*\left(\nu-\frac{\sigma}{2},\ P''\right)\cdot\frac{e^{i\cdot\frac{2\pi}{c}\left(\nu-\frac{\sigma}{2}\right)r''}}{r''}\Lambda''^*\left(\nu-\frac{\sigma}{2}\right)dP''\cdot e^{-2\pi i\nu\sigma}d\nu=$$

$$=\int_A\int_A\left\{\lim_{T\to\infty}\frac{1}{T}\int_{-\infty}^{\infty}v_T\left(\nu+\frac{\sigma}{2},\ P'\right)\nu_T^*\left(v-\frac{\sigma}{2},\ P''\right)e^{-2\pi i\nu\left(\tau-\frac{r''-r'}{c}\right)}\times\right.$$

$$\left.\times\Lambda'\left(\nu+\frac{\sigma}{2}\right)\Lambda''^*\left(\nu-\frac{\sigma}{2}\right)d\nu\right\}\frac{e^{-\pi i\sigma\frac{r''+r'}{c}}}{r'r''}\,dP'dP''$$

Jusqu'aux facteurs Λ' et Λ''^*, l'intégrale suivant ν, passée à la limite $T\to\infty$ représente justement la fonction de corrélation $\Gamma\left(P',\ P'',\ \tau-\frac{r''-r'}{c}\sigma\right)$; extrayant ces facteurs en dehors de l'intégrale suivant ν, ($v\cdot$[2], pg. 251 subsidiaire), par des valeurs moyennes adéquates $\overline{\Lambda'}$, $\overline{\Lambda''}$ (conditionnées par la forme de la distribution spectrale de la lumière), on obtient, finalement:

$$\Gamma(Q_1, Q_2, \tau, \sigma) = \int_A \int_A \Gamma\left(P', P'', \tau - \frac{r' - r''}{c}, \sigma\right) \cdot \overline{\Lambda}' \overline{\Lambda}''^{*} \cdot \frac{e^{-2\pi i \sigma \frac{r'' + r'}{2c}}}{r' r''} \, dP' dP'', \tag{9}$$

forme approximative de la loi de propagation de la fonction $\Gamma_{12}(\tau, \sigma)$ qui diffère de la forme correspondante établie par Wolf [2] pour la fonction $\Gamma_{12}(\tau)$ par le facteur $e^{-2\pi i \sigma \frac{r'' + r'}{2c}}$ et satisfait à la correspondance de la dernière pour $\sigma = 0$.

3. LA LOI EXACTE DE PROPAGATION. (LA FORME DIFFERENTIELLE)

La propagation du signal analytique complexe suit rigoureusement l'équation des ondes et, par conséquent, la forme locale (différentielle) de la loi de propagation de l'amplitude complexe c'est une équation Helmholtz [6]:

$$\Delta v + \left(\frac{2\pi\nu}{c}\right)^2 v = O \tag{10}$$

La forme exacte de la loi de propagation de l'amplitude complexe conditionne la forme exacte de la loi de propagation de la fonction de cohérence généralisée.

Revenant au développement spectral de celle-ci (8) et appliquant dans les deux membres l'opérateur laplacien en rapport avec les coordonnées du point Q_1:

$$\Delta_1 = \frac{\partial^2}{\partial x_1^2} + \frac{\partial^2}{\partial y_2^2} + \frac{\partial^2}{\partial z_2^2},$$

on obtient, employant (10)

$$\begin{aligned}
\Delta_1 \Gamma(Q_1, Q_2, \tau, \sigma) &= \lim_{T \to \infty} \frac{1}{T} \int_{-\infty}^{\infty} \left[\Delta_1 v_T\left(Q_1, \nu + \frac{\sigma}{2}\right)\right] v_T^*\left(Q_2, \nu - \frac{\sigma}{2}\right) e^{-2\pi i \nu \tau} \, d\nu = \\
&= -\left(\frac{2\pi}{c}\right)^2 \lim_{T \to \infty} \frac{1}{T} \int_{-\infty}^{\infty} \left(\nu + \frac{\sigma}{2}\right)^2 v_T\left(Q_1, \nu + \frac{\sigma}{2}\right) \cdot v_T^*\left(Q_2, \nu - \frac{\sigma}{2}\right) e^{-2\pi i \nu \tau} \, d\nu = \\
&= -\left(\frac{2\pi}{c}\right)^2 \lim_{T \to \infty} \frac{1}{T} \int_{-\infty}^{\infty} \Big(\nu^2 v_T\left(Q_1, \nu + \frac{\sigma}{2}\right) \cdot v_T^*\left(Q_2, \nu - \frac{\sigma}{2}\right) e^{-2\pi i \nu \tau} \, d\nu - \qquad (11) \\
&\quad - \left(\frac{2\pi}{c}\right)^2 \sigma \lim_{T \to \infty} \frac{1}{T} \int_{-\infty}^{\infty} \nu \, v_T\left(Q_1, \nu + \frac{\sigma}{2}\right) v_T^*\left(Q_2, \nu - \frac{\sigma}{2}\right) e^{-2\pi i \nu \tau} \, d\nu - \\
&\quad - \left(\frac{2\pi}{c}\right)^2 \frac{\sigma^2}{4} \lim_{T \to \infty} \frac{1}{T} \int_{-\infty}^{\infty} v_T\left(Q_1, \nu + \frac{\sigma}{2}\right) v_T^*\left(Q_2, \nu - \frac{\sigma}{2}\right) e^{-2\pi i \nu \tau} \, d\nu.
\end{aligned}$$

Toujours du développement spectral (8) de la fonction de cohérence mutuelle généralisée,

$$\frac{\partial\Gamma}{\partial\tau} = -\, 2\pi i \lim_{T\to\infty} \frac{1}{T}\int_{-\infty}^{\infty} \nu\, v_T\left(Q_1, \nu + \frac{\sigma}{2}\right) v_T^*\left(Q_2, \nu - \frac{\sigma}{2}\right) e^{-2\pi i\nu\tau}\, d\nu \quad (12)$$

$$\frac{\partial^2\Gamma}{\partial\tau} = -\,(2\pi)^2 \lim_{T\to\infty} \frac{1}{T}\int_{-\infty}^{\infty} \nu^2\, v_T\left(Q_2, \nu + \frac{\sigma}{2}\right) v_T^*\left(Q_2, \nu - \frac{\sigma}{2}\right) e^{-2\pi i\nu\tau}\, d\nu \quad (13)$$

Comparant (8) avec (11), (12), (13), résulte:

$$\Delta_1\Gamma = \frac{1}{c^2}\left[\frac{\partial^2\Gamma}{\partial\tau^2} - i2\pi\sigma\frac{\partial\Gamma}{\partial\tau} - \pi^2\sigma^2\Gamma\right] \quad (14)$$

Par un calcul similaire,

$$\Delta_2\Gamma = \frac{1}{c^2}\left[\frac{\partial^2\Gamma}{\partial\tau^2} + i2\pi\sigma\frac{\partial\Gamma}{\partial\tau} - \pi^2\sigma^2\Gamma\right] \quad (15)$$

Université de Bucarest, Faculté de Physique

BIBLIOGRAPHIE

[1] F. Fischer, Z. Phys., 1967, v. 199, nr. 5, pg. 541
[2] E. Wolf; Proc. Roy. Soc., A. 1955, v. 230, pg. 246
[3] E. Rupp, Z. Pyhs., 1928, v. 47 pg. 72
[4] P. Connes, Duong Hong Tuan, J. Pinard, Journ. Phys. Rad., 1962, t. 23, pg. 173
[5] B. Schmidt, J. Williams, D. Williams, J.O.S.A., 1963, v. 51, nr. 4
[6] M· Born, E. Wolf, Principles of Optics, Pergamon Pres, 1959
[7] M. Beran, G. B. Parrent, Theory of Partial Coherence, Englewood Cliffs, N. Y., Prentice-Hall, Inc. 1964

SUR LES ABERRATIONS DE TROISIÈME ORDRE DES SYSTÈMES OPTIQUES CENTRÉS

G. G. BRĂTESCU

En utilisant la méthode de Flügge [1] les coefficients partiels des aberrations de troisième ordre ont été calculés en fonction des distances ayant l'origine les centres des dioptres sphériques centrés d'un système optique. L'introduction des grandeurs convenables a permis la déduction des relations entre les coefficients des aberrations.

1. INTRODUCTION

Dans son traité Flügge [1] dévelloppe une théorie sur les aberrations de troisième ordre pour des systèmes optiques des dioptres centrés. Il calcule es grandeurs caractéristiques d'un système optique en fonction des distances *s* de l'objet et des images ayant l'origine les surfaces des dioptres.

Dans cet ouvrage on donne brièvement quelques calculs et les résultats obtenus sur les mêmes grandeurs caractéristiques, mais par l'emploi des distances x de l'objet, respectivement des images ayant l'origine les centres C_ν des dioptres sphériques de rayons $R_\nu \neq \infty$ qui constituent le système optique forme par k dioptres sphériques centrés.

2. LE SCHÉMA DE BASE. NOTATIONS. SIGNES CONVENTIONNELS

Pour le dioptre ν, les notations et les signes conventionnels sont rendus par la figure 1. Pour distinguer les signes des opérations algébriques (+ et —) et les signes conventionnels,comme signes conventionnels pour les distances et pour les angles on a choisi un point (.) et une ligne (—) pour les valeurs positives, respectivement pour les valeurs négatives, écrits sur la grandeur respective ($\dot{x} \equiv + x$, $\overline{R} \equiv - R$, $\overline{\varphi} \equiv - \varphi$, etc).

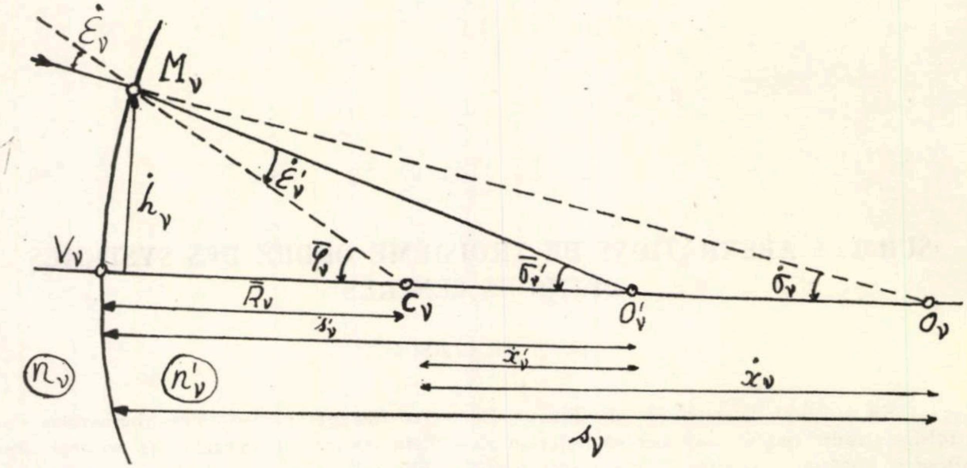
$\dot{\varepsilon}_\nu$
M_ν
$\dot{\varepsilon}'_\nu$
$\dot{h}_\nu$
V_ν
$\bar{\varphi}_\nu$
$\bar{\sigma}'_\nu$
$\dot{\sigma}_\nu$
$\bar{R}_\nu$
C_ν
O'_ν
O_ν
s'_ν
$\dot{x}'_\nu$
$\dot{x}_\nu$
n_ν
n'_ν
s_ν

Fig. 1

Une analyse très simple nous montre que pour les grandeurs de l'espace objet et de l'espace image, il resulte des valeurs positives ou négatives couplées de ces grandeurs.

3. LES RELATIONS FONDAMENTALES D'UN SYSTÈME DE K DIOPTRES SPHÉRIQUES CENTRÉS

3.1. Pour le dioptre ν nous avons:

$$\frac{n'_\nu \sin \varepsilon'_\nu}{n_\nu \sin \varepsilon_\nu} = +1 \tag{1}$$

$$\frac{n'_\nu\, x'_\nu \sin \sigma'_\nu}{n_\nu\, x_\nu \sin \sigma_\nu} = +1 \tag{2}$$

3.2. Dans le système formé par k dioptres sphériques centrés nous avons les relations:

$$n'_{\nu-1} = n_\nu \tag{3}$$

$$\sigma'_{\nu-1} = \sigma_\nu \tag{4}$$

$$n'_{\nu-1} \sin \sigma'_{\nu-1} = n_\nu \sin \sigma_\nu \tag{5}$$

dont on obtient la relation:

$$\frac{n'_k \sin \sigma'_k}{n_1 \sin \sigma_1}\, \frac{x'_1\, x'_2 \ldots\ldots\ldots x'_k}{x_1\, x_2 \ldots\ldots\ldots x_k} = +1 \tag{6}$$

4. L'OPTIQUE PARAXIALE DE GAUSS (NOTATION G), POUR LES PETITS ANGLES

4.1. Les relations 1, 2 et 6 deviennent:

$$\frac{n'_\nu\,\varepsilon'_\nu}{n_\nu\,\varepsilon_\nu} = +1 \tag{7}$$

$$\frac{n'_\nu\,x'_\nu\,\sigma'_\nu}{n_\nu\,x_\nu\,\sigma_\nu} = +1 \tag{8}$$

$$\frac{n'_k\,\sigma'_k}{n_1\,\sigma_1}\,\frac{x'_{1G}\,x'_{2G}\cdots\cdots\sigma'_{kG}}{x_{2G}\,x_{2G}\cdots\cdots x_{kG}} = +1 \tag{9}$$

4.2. On obtient un invariant de type Abbe:

$$\underset{\sim}{Q}{}^B_\nu = \frac{1}{n_\nu}\left(\frac{1}{R_\nu} - \frac{1}{x_{\nu G}}\right) = \frac{1}{n'_\nu}\left(\frac{1}{R_\nu} - \frac{1}{x'_{\nu G}}\right) \tag{10}$$

4.3. On introduit la grandeur Ω. Parceque (voir la figure 2):

$$y'_{(\nu-1)G} = y_{\nu G} \tag{11}$$

nous avons:

$$\Omega_1 = \frac{\operatorname{tg}\alpha_1}{\operatorname{tg}\alpha_1} = 1\,; \qquad \Omega_2 = \frac{\operatorname{tg}\alpha_2}{\operatorname{tg}\alpha_1} = \frac{\dfrac{y_{2G}}{x_{2G}}}{\dfrac{y'_{1G}}{x'_{1G}}} = \frac{x'_{1G}}{x_{2G}}\,; \ldots\ldots;$$

$$\Omega_\nu = \frac{\operatorname{tg}\alpha_\nu}{\operatorname{tg}\alpha_1} \approx \frac{\alpha_\nu}{\alpha_1} = \frac{x'_{1G}\,x'_{2G}\,x'_{3G}\cdots x'_{(\nu-1)G}}{x_{2G}\,x_{3G}\cdots x_{(\nu-1)G}\,x_{\nu G}} \tag{12}$$

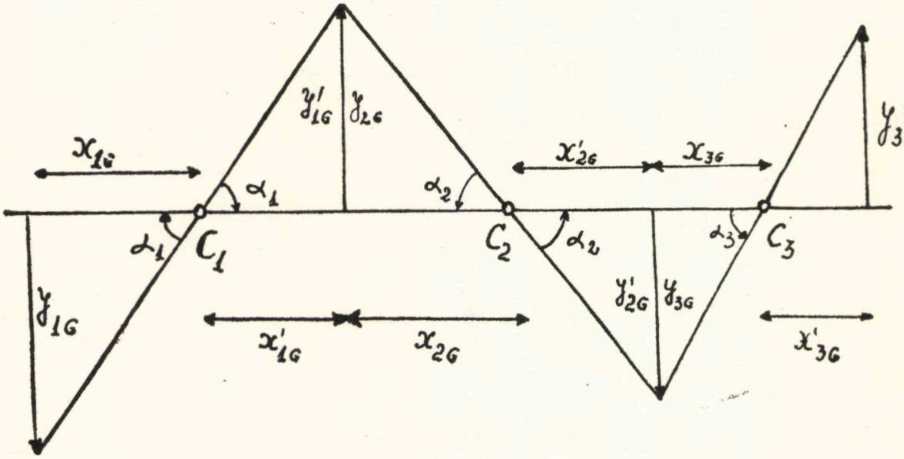

Fig. 2

En utilisant les relations 3, 11 et 13

$$y_{\nu G} = x_{\nu G} \operatorname{tg} \alpha_\nu \quad y'_{(\nu-1)G} = x'_{(\nu-1)G} \operatorname{tg} \alpha_{\nu-1} \tag{13}$$

on obtient la relation 14:

$$x'_{(\nu-1)G} \operatorname{tg} \alpha_{\nu-1} = x_{\nu G} \operatorname{tg} \alpha_\nu; \quad x'_{(\nu-1)G}\Omega_{\nu-1} = x_{,G}\Omega_\nu \tag{14}$$

et aussi la relation 15:

$$n'_{\nu-1}x'_{(\nu-1)G}\Omega_{\nu-1} = n_\nu x_\nu \Omega_\nu \tag{15}$$

4.4. Le grandissement (transversal) β' est donné par 16:

$$\beta'_1 = \frac{y'_{1G}}{y_{1G}} = \frac{x'_{1G}}{x_{1G}}; \ldots; \beta'_\nu = \frac{y'_{\nu G}}{y_{\nu G}} = \frac{x'_{\nu G}}{x_{\nu G}} \tag{16}$$

et par la relation 17, en fonction des $x_{\nu G}$ et Ω_k:

$$\beta' = \beta'_1\beta'_2 \ldots \beta'_\nu \ldots \beta'_k = \frac{y'_{1G}y'_{2G} \cdots y'_{kG}}{y_{1G}y_{2G} \cdots y_{kG}} = \frac{y'_{kG}}{y_{1G}} = \frac{x'_{1G}x'_{2G} \cdots x'_{kG}}{x_{1G}x_{2G} \cdots x_{kG}} = \frac{x'_{kG}}{x_{1G}}\,\Omega_k \tag{17}$$

De l'invariant de Lagrange-Helmholtz:

$$y_{1G}n_1 \operatorname{tg} \sigma_{1G} = y'_{1G}n'_1 \operatorname{tg} \sigma'_{1G} = \ldots = y_{kG}n_k \operatorname{tg} \sigma_{kG} = y'_{kG}n'_k \operatorname{tg} \sigma'_{kG}$$

il resulte 17a:

$$\beta' = \frac{y'_{kG}}{y_{1G}} = \frac{n_1 \operatorname{tg} \sigma_{1G}}{n'_k \operatorname{tg} \sigma'_{kG}} \approx \frac{n_1\sigma_{1G}}{n'_k\sigma'_{kG}} \tag{17 a}$$

c'est-à-dire:

$$n_1 x_{1G} \operatorname{tg} \sigma_{1G} \operatorname{tg} \alpha_{1G} = n'_k x'_{kG} \operatorname{tg} \sigma'_{kG} \operatorname{tg} \alpha'_{kG} \tag{18 a}$$

ou:

$$n_1 x_{1G}\sigma_{1G}\alpha_{1G} = n'_k x'_{kG}\sigma'_{kG}\alpha'_{kG} \tag{18 b}$$

Flügge [1] a introduit la grandeur ω_ν:

$$\omega_\nu = \frac{h_{\nu G}}{h_{1G}}$$

qui est liée de β' par la relation 19:

$$\beta' = \frac{s'_{kG}}{n'_k}\,\frac{n_1}{s_{1G}}\,\frac{1}{\omega_k} \tag{19}$$

De 17 et 19 résulte:

$$\frac{n_1 x_{1G}}{s_{1G}}\,\frac{s'_{kG}}{n'_k x'_{kG}} = \omega_k\Omega_k \tag{20}$$

4.5. La distance focale f. De la relation 10 on obtient 21:

$$\frac{n'_\nu}{x_{\nu G}} - \frac{n_\nu}{x'_{\nu G}} = \frac{n'_\nu - n_\nu}{R_\nu} = \frac{1}{f_\nu} \tag{21}$$

Notons avec le signe = les grandeurs qui sont obtenues dans le cas d'utilisation des faisceaux parallèles à l'axe optique du système, c'est-à-dire, par exemple:

$$x_{1G} \to \infty \quad x'_{1G} \to \underline{\underline{x}}'_{1G}$$

Nous avons:

$$x_\nu = \infty \quad \underline{\underline{x}}'_{\nu G} = -\frac{n_\nu R_\nu}{n'_\nu - n_\nu} = -n_\nu f_\nu \tag{22 a}$$

et aussi:

$$x'_\nu = \infty \quad \underline{\underline{x}}_{\nu G} = +\frac{n'_\nu R_\nu}{n'_\nu - n_\nu} = +n'_\nu f_\nu \tag{22 b}$$

Pour *k* dioptres sphériques centrés, en fonction des distances s_ν on obtient [1] pour $s_{1G} = \infty$ la relation 23:

$$f_{(1-k)} \equiv f = \frac{\frac{\underline{\underline{s}}'_{1G}}{n'_1}\,\frac{\underline{\underline{s}}'_{2G}}{n'_2}\,\frac{\underline{\underline{s}}'_{3G}}{n'_3}\cdots\frac{\underline{\underline{s}}'_{kG}}{n'_k}}{\frac{\underline{\underline{s}}_{2G}}{n_2}\,\frac{\underline{\underline{s}}_{3G}}{n_3}\cdots\frac{\underline{\underline{s}}_{kG}}{n_k}} \tag{23}$$

Il resulte de la figure 1 et de la relation 8:

$$\frac{\sigma_{\nu G}}{\sigma'_{\nu G}} = \frac{s'_{\nu G}}{s_{\nu G}} = \frac{n'_\nu x'_{\nu G}}{n_\nu x_{\nu G}}$$

et à l'aide des relations 23 et 22a on obtient:

$$f = \frac{\underline{\underline{x}}'_{1G} + R_1}{n'_1}\,\frac{\underline{\underline{x}}'_{2G}\underline{\underline{x}}'_{3G}\cdots\underline{\underline{x}}'_{kG}}{\underline{\underline{x}}_{2G}\underline{\underline{x}}_{3G}\cdots\underline{\underline{x}}_{kG}} = \frac{n'_1 - 2n_1}{n'_1(n'_1 - n_1)}\,R_1\,\frac{\underline{\underline{x}}'_{2G}\underline{\underline{x}}'_{3G}\cdots\underline{\underline{x}}'_{kG}}{\underline{\underline{x}}_{2G}\underline{\underline{x}}_{3G}\cdots\underline{\underline{x}}_{kG}} \tag{24}$$

5. L'ABERRATION DE LA SPHÉRICITÉ

5.1. Les relations générales exactes pour un dioptre sphérique résultent de la figure 1 d'où nous pouvons obtenir les relations:

$$\frac{x}{\sin\varepsilon}n = \frac{R}{\sin\sigma}n; \quad \frac{1}{nx} = \frac{\sin\sigma}{Rn\sin\varepsilon}; \quad \frac{1}{n'x'} = \ldots \tag{25}$$

et

$$\frac{1}{n'x'} = \frac{1}{nx} + \frac{\sin\sigma' - \sin\sigma}{Rn\sin\varepsilon} \tag{26}$$

Dans le domaine de Gauss, de la relation 10, on obtient 27:

$$\frac{1}{n'x'_G} = \frac{1}{nx_G} + \frac{1}{nR} - \frac{1}{n'R} \tag{10, 27}$$

5.2. **L'aberration de sphéricité principale. L'invariant B [2] [3].** Pour les rayons incidente parallèles à l'axe d'un dioptre sphérique nous avons:

$$x = \infty \qquad \sigma = 0 \qquad \sigma' = \varepsilon - \varepsilon' \qquad \varphi = \varepsilon$$

et les relations 25 et 27 deviennent:

$$\frac{1}{n'\underline{\underline{x}}'} = \frac{\sin(\varepsilon - \varepsilon')}{Rn\sin\varepsilon} \qquad \frac{1}{n'\underline{\underline{x}}'_G} = \frac{n' - n}{nn'R}$$

On fait le rapport $\frac{\underline{\underline{x}}'}{\underline{\underline{x}}'_G}$:

$$\frac{\underline{\underline{x}}'}{\underline{\underline{x}}'_G} = \frac{n' - n}{n'}\,\frac{\sin\varepsilon}{\sin(\varepsilon - \varepsilon')} = \left(1 - \frac{\sin\varepsilon'}{\sin\varepsilon}\right)\frac{\sin\varepsilon}{\sin(\varepsilon - \varepsilon')} = \frac{\sin\varepsilon - \sin\varepsilon'}{\sin\frac{2(\varepsilon - \varepsilon')}{2}} = \frac{\cos\frac{\varepsilon + \varepsilon'}{2}}{\cos\frac{\varepsilon - \varepsilon'}{2}}$$

ou:

$$\mathbf{x}'\,\frac{\cos\frac{\varepsilon - \varepsilon'}{2}}{\cos\frac{\varepsilon - \varepsilon'}{2}} = \underline{\underline{x}}'_G = -\frac{nR}{n' - n} = -nf = B \tag{28}$$

5.3. **L~~a~~e calcul[redacted] exacte de l'aberration de sphéricité pour un dioptre sphérique**. Par la soustraction de la relation 27 de 26 et avec la relation 29

$$\sigma + \varepsilon = \sigma' + \varepsilon' \tag{29}$$

on obtient 30:

$$\frac{1}{n'}\left(\frac{1}{x'} - \frac{1}{x'_G}\right) = \frac{1}{n}\left(\frac{1}{x} - \frac{1}{x_G}\right) - 4\,\frac{\sin\left(\frac{\sigma + \varepsilon}{2}\right)\sin\left(\frac{\sigma - \varepsilon'}{2}\right)\sin\left(\frac{\varepsilon - \varepsilon'}{2}\right)}{Rn\sin\varepsilon} \tag{30}$$

qui, par l'utilisation des relations 2 et 25, peut prendre aussi les formes:

$$(x' - x'_G) = \frac{n'x'x'_G}{nxx_G}(x - x_G) + 4\,\frac{n'x'x'_G}{Rn\sin\varepsilon}\sin\left(\frac{\sigma + \varepsilon}{2}\right)\sin\left(\frac{\sigma - \varepsilon'}{2}\right)\sin\left(\frac{\varepsilon - \varepsilon'}{2}\right) \tag{31}$$

ou:

$$\left(\frac{x' - x'_G}{x'_G}\right) \sin \sigma' = \left(\frac{x - x_G}{x_G}\right) \sin \sigma + 4 \sin\left(\frac{\sigma + \varepsilon}{2}\right) \sin\left(\frac{\sigma - \varepsilon'}{2}\right) \sin\left(\frac{\varepsilon - \varepsilon'}{2}\right) \tag{32}$$

5.4. **Les cas des rayons situés (tout) près de l'axe optique, le cas de Flügge [1].**

De 16, 25 et 33:

$$h = R \sin \varphi = R \sin (\sigma + \varepsilon) \tag{33}$$

resulte 34:

$$x'_G = \frac{h\varepsilon'}{(\sigma + \varepsilon)\, \sigma'} \tag{34}$$

et de 32 on obtient les aberrations longitudinales de sphéricité données par 35:

$$(x' - x'_G)\, \sigma' = \beta'(x - x_G) + \frac{1}{2}\, h\, \frac{\varepsilon'(\sigma - \varepsilon')(\varepsilon - \varepsilon')}{\sigma'} \tag{35}$$

et aussi les aberrations transversales de sphéricité Δy:

$$(x - x_G)\, \sigma = \Delta y \quad \text{et} \quad (x' - x'_G)\, \sigma' = \Delta y' \tag{36}$$

c'est-à-dire:

$$\Delta y' = \beta' \Delta y - \frac{h}{2}\, \frac{\varepsilon'(\sigma - \varepsilon')(\varepsilon - \varepsilon')}{\sigma'} \tag{37}$$

ou, tenant compte de 34 et de 16:

$$\Delta y' = \beta' \Delta y + \frac{1}{2}\, x'_G (\sigma + \varepsilon)(\sigma - \varepsilon')(\varepsilon - \varepsilon') \tag{38}$$

ou:

$$\Delta y' = \beta' \left[\Delta y + \frac{1}{2}\, x_G (\sigma + \varepsilon)(\sigma - \varepsilon')(\varepsilon - \varepsilon')\right] \tag{39}$$

5.5. **La somme des coefficients partiels.** Parceque:

$$\underset{\nu - 1}{\Delta y'} = \underset{\nu}{\Delta y} \tag{40}$$

nous avons, avec la relation 38:

$$\begin{aligned}
&\underset{2}{\Delta y'} = \beta'_2\, \underset{1}{\Delta y'} + \frac{1}{2}\, x'_{2G} (\sigma_2 + \varepsilon_2)(\sigma_2 - \varepsilon'_2)(\varepsilon_2 - \varepsilon'_2) \\
&\underset{3}{\Delta x'} = \ldots \\
&\vdots \\
&\underset{k}{\Delta y'} = \ldots
\end{aligned}$$

En calculant les parenthèses et en utilisant les relations 12 et 17, on obtient:

$$\underset{k}{\Delta y'} = \beta' \underset{1}{\Delta y} + \frac{1}{2} x'_{kG} \Omega_k \sum_{1}^{k} \frac{1}{\Omega_k} (\sigma_\nu - \varepsilon_\nu)(\sigma_\nu - \varepsilon'_\nu)(\varepsilon_\nu - \varepsilon'_\nu) \tag{41}$$

Par la multiplication avec le facteur $\left(\frac{h_1}{f}\right)^3 \left(\frac{f}{h_1}\right)^3$ dans le deuxième terme on obtient:

$$\underset{k}{\Delta y'} = \beta' \underset{1}{\Delta y} + \frac{1}{2} x'_{kG} \Omega_k \left(\frac{h_1}{f}\right)^3 \sum_{1}^{k} \mathcal{H}_\nu \tag{42}$$

avec:

$$\mathcal{H}_\nu = \left(\frac{f}{h_1}\right)^3 \frac{1}{\Omega_\nu} (\sigma_\nu + \varepsilon_\nu)(\sigma_\nu - \varepsilon'_\nu)(\varepsilon_\nu - \varepsilon'_\nu) \tag{43}$$

6. L'ABERRATION DE LA COMA

6.1. Le calcul de l'aberration présentée par une seule surface.

Les rayons couplés qui proviennent des points $B_{v,h}$ et $D_{v\,h}$ qui appartiennent au contour de l'ouverture-diaphragme Σ forment les images ponctuelles O'_{SB}, respectivement O'_D, et non pas l'image O' de l'objet O situé sur le rayon principal H, figure 3. O_G et O'_G sont les points conjugués dans l'approxima-

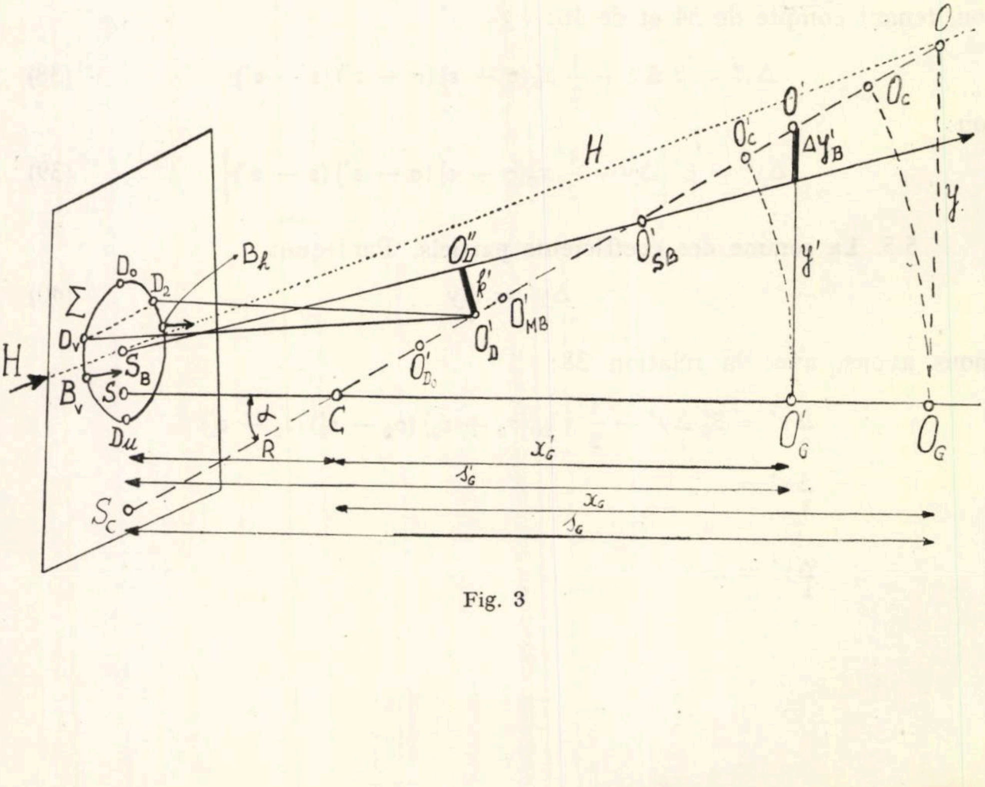

Fig. 3

tion de Gauss pour l'objet y $(= 0)$ et son image y' $(= 0)$. Le segment k' $(\perp S_B O'_{SB})$ est la mesure de la coma. Avec les notations de la figure 4 on obtient pour k' [1] la valeur donnée par 44:

$$k' = b\,\frac{a(2qb + h^2)}{(R + x'_G)} \tag{44}$$

où a est le facteur de proportionalité dans le domaine de Seidel (du troisième ordre) pour l'aberration de sphéricité.

6.2. **Le système des surfaces sphériques centrés.**

Pour un objet dépourvu des aberrations on obtient pour les k surfaces les valeurs:

$$\begin{aligned} k' &= k'_1 \\ k' &= \beta'_2 k'_1 + k'_2 \\ &\vdots \\ k' &= (\beta'_2\beta'_3\ldots\beta'_k)\,k'_1 + \\ &\quad + (\beta'_3\beta'_4\ldots\beta'_k)\,k'_2 + \ldots + \beta'_k k'_{k-1} + k'_k \end{aligned} \tag{45}$$

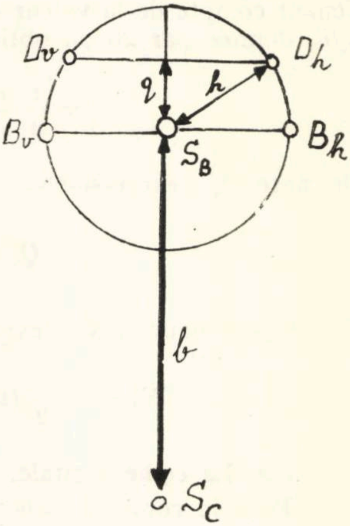

Fig. 4

Tenant compte de 17a, la relation 45 peut être écrite:

$$k' = \frac{n'_1\sigma'_{1G}}{n'_k\sigma'_{kG}}\,k'_1 + \frac{n'_2\sigma'_{2G}}{n'_k\sigma'_{kG}}\,k'_2 + \ldots + \frac{n'_{(k-1)}\sigma'_{(k-1(G}}{n'_k\sigma'_{kG}}\,k'_{(k-1)} + k'_k \tag{46}$$

La contribution (CK) de la surface ν dans la valeur de k' est donnée par 47:

$$(CK) = \frac{n'_\nu\sigma'_{\nu G}}{n'_k\sigma'_{kG}}\,k'_\nu \tag{47}$$

En utilisant les relations 17, 17a et 44 on obtient 48:

$$(CK) = \frac{x'_{kG}}{x'_{\nu G}}\,\frac{\Omega_k}{\Omega_\nu}\,b_\nu a_\nu\,\frac{(2q_\nu b_\nu + h_\nu^2)}{(R_\nu + x'_{\nu G})} \tag{48}$$

Le facteur a_ν de Seidel est donné par la relation 49:

$$(x - x'_G) = ah_1^2 + a'h_1^4 + \ldots \approx ah_1^2 \tag{49}$$

En utilisant les relations 36, 39, 49 et ayant en vue que:

$$(x - x_G) = 0 \qquad \text{et} \qquad \sigma'_\nu = \frac{h_\nu}{R_\nu + x_{\nu G}}$$

on obtient pour a_ν la valeur donnée par 50:

$$a_\nu = \frac{x'_\nu - x'_{\nu G}}{h_\nu^2} = +\,\frac{1}{2}\,\frac{x'_{\nu G}}{h_\nu^2\sigma'_\nu}\,(\varepsilon_\nu - \varepsilon'_\nu)\,(\sigma_\nu + \varepsilon_\nu)\,(\sigma_\nu - \varepsilon'_\nu) \tag{50}$$

Tenant compte de la valeur de $\mathcal{H}$ donnée par 43 et de la valeur du rapport h_ν/h_1 donnée par 20 on obtient pour a_ν l'expression 51:

$$a_\nu = \frac{1}{2}\,\frac{x'^4_{\nu G}}{x^3_{1G}}\,\Omega^4_\nu \left(\frac{n'_\nu}{n_1}\right)^3 \frac{(R_1 + x_{1G})^3}{(R_\nu + x'_{\nu G})^2}\left(\frac{1}{f}\right)^3 \mathcal{H}_\nu \tag{51}$$

On note Q_ν l'expression:

$$Q_\nu = \frac{n_\nu\, x_{\nu G}}{R_\nu + x_{\nu G}} = \frac{n'_\nu\, x'_{\nu G}}{R_\nu + x'_{\nu G}} \tag{52}$$

On obtient pour (CK) l'expression finale 53:

$$(CK) = +\,\frac{1}{2}\,(\Omega_k\, x'_{kG})\,\Omega^3_\nu \left(\frac{Q_\nu}{Q_1}\right)^3 \left(\frac{1}{f}\right)^3 b_\nu\,\mathcal{H}_\nu(2q_\nu b_\nu + h^2_\nu) \tag{53}$$

6.3. **La come sagitale. Le coefficient partiel de la come.**

Pour la come sagitale, $q_\nu = 0$ et la contribution (CKs) donnée par la surface ν est exprimée par la relation 54:

$$(CKs) = +\,\frac{1}{2}\,(\Omega_k\, x'_{kG})\left(\frac{b_\nu}{h_\nu}\right)\left(\frac{h_1}{f}\right)^3 \mathcal{H}_\nu \tag{54}$$

En utilisant les grandeurs caractéristiques de la pupille d'entrée

$$n_1 \qquad \sigma_{P1} \qquad \omega_{PE} = \frac{y_{PE}}{h_1} = \frac{h_{PE}}{h_1}$$

alors

$$h_\nu = (R_\nu + x'_{\nu G})\,\sigma'_\nu = (R_\nu + x'_{\nu G})\,\varepsilon'_\nu\,\frac{R_\nu}{x'_{\nu G}} \tag{55}$$

$$b_\nu = (R_\nu + x'_{\nu G})\,\sigma'_{B\nu} = (R_\nu + x'_{\nu G})\,\varepsilon'_{B\nu}\,\frac{R_\nu}{x'_{\nu G}} \tag{56}$$

et par multiplication et division par $(n_1\sigma_{B1}\omega_{PE})$ on obtient:

$$(CKs) = +\,\frac{1}{2}\,(\Omega_k x'_{kG})\left(\frac{h_1}{f}\right)^2 (n_1\sigma_{B1}\omega_{PE})\,\mathcal{C}_\nu \tag{57}$$

ou $\mathcal{C}_\nu$ est le coefficient partiel de la coma:

$$\mathcal{C}_\nu = p_\nu \mathcal{H}_\nu \tag{58}$$

avec:

$$p_\nu = -\left(\frac{\varepsilon'_{B\nu}}{\sigma_{B1}}\right)\left(\frac{h_1}{f\varepsilon'_\nu}\right)\left(\frac{1}{n_1\omega_{PE}}\right) \tag{59}$$

7. L'ASTIGMATISME. LE COEFFICIENT PARTIEL DE L'ASTIGMATISME

Comme mesure de l'astigmatisme on prend la variation de la distance entre le rayon principal et la position d'un point de la ligne de l'image caractéristique lorsqu'on passe de S' à M'_0, respectivement à M'_u, la figure 5. Dans la relation 53 on prend $q_\nu = h_\nu$ et utilisant les relations 20, 55, 56, 59, on obtient la contribution (CA) de la surface à l'astigmatisme sous la forme donnée par 60:

$$(CA) = (\Omega_k x'_{kG}) \left(\frac{b_\nu}{h_\nu}\right)^2 \left(\frac{h_1}{f}\right)^3 \mathcal{H}_\nu = (\Omega_k x'_{kG}) \left(\frac{h_1}{f}\right) (n_1 \sigma_{B1} \omega_{PE})^2 \mathcal{A}_\nu \tag{60}$$

ou A_ν est le coefficient partiel de l'astigmatisme:

$$\mathcal{A}_\nu = p_\nu^2 \mathcal{H}_\nu = p_\nu \mathcal{C}_\nu \tag{61}$$

8. LA DISTORSION

8.1. Comme mesure de la distorsion on prend l'écart $\Delta y'_B$, la figure 3. $O'_G O' = y'$ est l'image dépourvue des aberrations de l'objet $O_G O = y$. Avec les notations contenues dans les figures 3 et 4, $\Delta y'_B$ est donnée par [1] par la relation 62:

$$\Delta y'_B = \Delta y'_{\mathrm{I}} + \Delta y'_{\mathrm{II}} \tag{62}$$

ou:

$$\Delta y'_{\mathrm{I}} = \frac{a}{R + x'_G} b^3 \tag{63}$$

$$\Delta y'_{\mathrm{II}} = \frac{y'^2 n'}{2(R + x'_G)} b \left(\frac{n - n'}{nn'R}\right) \tag{64}$$

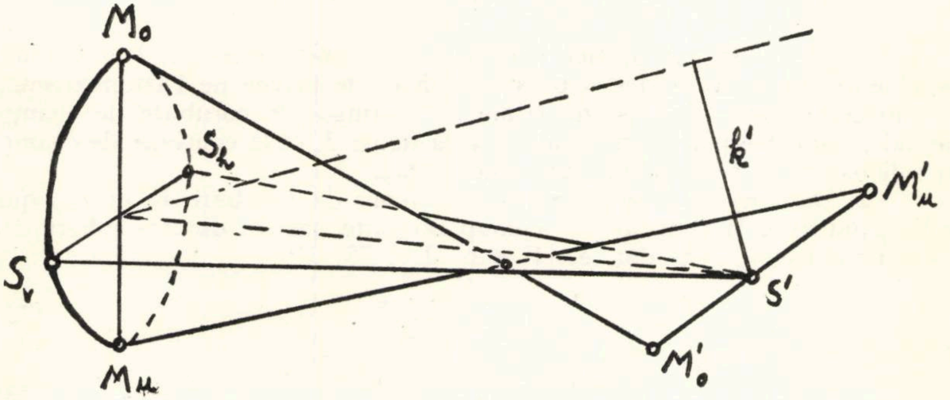

Fig. 5

8.2. La contribution (CD) de la surface ν à la distorsion s'obtient pour un objet depourvu des aberrations, par le même procédé utilisé pour la coma:

$$(CD)_{\mathrm{I}} = -\frac{1}{2}\,(\Omega_k x'_{kG})\,(n_1\sigma_{B1}\omega_{PE})^3\, p_\nu^3\mathcal{H}_\nu \tag{65}$$

$$(CD)_{\mathrm{II}} = +\frac{1}{2}\,(\Omega_k x'_{kG})\,\frac{1}{Q_1}\,(n_1\sigma_{B1}\omega_{PE})^3\, p_\nu P_\nu =$$

$$= -\frac{1}{2}\,(\Omega_k x'_{kG})\,(n_1\sigma_{B1}\omega_{PE})^3 p_\nu \mathcal{P}_\nu \tag{66}$$

ou Q_1 est exprimé par la relation 52 et P_ν est la coefficient partiel de Petzval donné par 67:

$$P_\nu = \frac{n'_\nu - n_\nu}{n_\nu n'_\nu}\,\frac{f}{R_\nu} \tag{67}$$

et en conséquence:

$$\mathcal{P}_\nu = -\frac{P_\nu}{Q_1} \tag{68}$$

On obtient pour (CD) l'expression 69:

$$(CD) = -\frac{1}{2}\,(\Omega_k x'_{kG})\,(n_1\sigma_{B1}\omega_{PE})^3\,\mathcal{D}_\nu \tag{69}$$

où $\mathcal{D}_\nu$ est le coefficient partiel pour la distorsion redonné par 70 et 71:

$$\mathcal{D}_\nu = p_\nu^3\mathcal{H}_\nu + p_\nu\mathcal{P}_\nu^1 = p_\nu\mathcal{S}_\nu \tag{70}$$

$$\mathcal{S}_\nu = p_\nu^2\mathcal{H}_\nu + \mathcal{P}_\nu = \mathcal{A}_\nu + \mathcal{P}_\nu \tag{71}$$

9. LA CORUBURE DE CHAMP

9.1. Le coefficient partiel Petzval P_ν est une mesure de la courbure de champ due à la surface ν pour une imagerie privée de l'astigmatisme. A l'imagerie douée de l'astigmatisme on distingue la corubure de champ sagitale, qui correspond aux points O'_{SB}, la figure 3, et la courbure de champ méridionale qui correspond aux points O'_{MB}.

9.2. Dans le domaine de Seidel les rayons de courbure r'_S et r'_M, qui correspondent à la courbure de champ produite par un dioptre sphérique, les figures 3 et 4, sont donnés [1] par 72 et 73:

$$\frac{1}{r'_S} = \frac{2ab^2}{y'^2} + \frac{n - n'}{nR} \tag{72}$$

$$\frac{1}{r'_M} = \frac{6ab^2}{y'^2} + \frac{n - n'}{nR} \tag{73}$$

et la contribution de la surface ν est donnée par 74:

$$\left(\frac{1}{r'_S}\right)_\nu = n'_k \left(\frac{2a_\nu b_\nu^2}{n'_\nu y'^2_\nu} + \frac{n_\nu - n'_\nu}{n_\nu n'_\nu R_\nu}\right) \tag{74}$$

et 75:

$$\left(\frac{1}{r'_M}\right)_\nu = n'_k \left(\frac{6a_\nu b_\nu^2}{n'_\nu y'^2_\nu} + \frac{n_\nu - n'_\nu}{n_\nu n'_\nu R_\nu}\right) \tag{75}$$

9.3. Comme mesure de la corubure des images sagitales et méridionales on prend les grandeurs:

$$-\frac{f}{n'_k r'_S} \quad \text{et} \quad -\frac{f}{n'_k r'_M} \tag{76}$$

9.4. Les contributions de la surface ν pour ces courbures sont exprimées par les coefficients partiels de la corubure sagitale S_ν et S_ν et meridionale $\mathcal{M}_\nu$ et M_ν donnés par les expressions 77, 78, 79 et 80:

$$S_\nu = \left(-\frac{f}{n'_k r'_S}\right)_\nu = -f\left(\frac{2a_\nu b_\nu^2}{n'_\nu y'^2_\nu} + \frac{n_\nu - n'_\nu}{n_\nu n'_\nu R_\nu}\right) = -p_\nu^2 Q_1 \mathcal{H}_\nu + P_\nu \tag{77}$$

$$\mathcal{S}_\nu = \frac{S_\nu}{-Q_1} = +p_\nu^2 \mathcal{H}_\nu + \mathcal{P}_\nu = \mathcal{A}_\nu + \mathcal{P}_\nu \tag{78}$$

$$M_\nu = \left(-\frac{f}{n'_k r'_M}\right)_\nu = -f\left(\frac{6a_\nu b_\nu^2}{n'_\nu y'^2_\nu} + \frac{n_\nu - n'_\nu}{n_\nu n'_\nu R_\nu}\right) = 3p_\nu^2 Q_1 \mathcal{H}_\nu + P_\nu \tag{79}$$

$$\mathcal{M}_\nu = \frac{M_\nu}{-Q_1} = 3p_\nu^2 \mathcal{H}_\nu + \mathcal{P}_\nu = 3\mathcal{A}_\nu + \mathcal{P}_\nu \tag{80}$$

9.5. Pour la courbure moyenne de champ on introduit un autre coefficient partiel donné par la relation 81:

$$W_\nu = \left(-\frac{f}{n'_k r'_W}\right)_\nu = \frac{1}{2}\left(M_\nu + S_\nu\right) \tag{81}$$

ou par 82:

$$\mathcal{W}_\nu = \frac{W}{-Q_1} = \frac{1}{2}\left(\mathcal{M}_\nu + \mathcal{P}_\nu\right) = 2\mathcal{A}_\nu + \mathcal{P}_\nu \tag{82}$$

10. LES VALEURS DES ABERRATIONS D'UN SYSTÈME OPTIQUE

Ces valeurs des aberrations d'un système optique formé de k dioptres sphériques ($R_\nu \neq \infty$) pour un objet plan depourvu des aberrations sont données par les relations générales suivantes:

10.1. L'aberration de sphéricité:

$$\Delta y' = +\frac{1}{2}\left(\frac{h_1}{f}\right)^3 (\Omega_k x'_{kG}) \sum_{\nu=1}^{k} \mathcal{H}_\nu \tag{83}$$

10.2. La coma:

$$k' = + \frac{1}{2} (n_1 \sigma_{B1} \omega_{PE}) \left(\frac{h_1}{f} \right)^2 (\Omega_k x'_{kG}) \sum_{\nu=1}^{k} \mathcal{C}_\nu \tag{84}$$

10.3. L'astigmatisme:

$$\frac{1}{2} \left[\left(\frac{f}{n'_k r'_S} \right) - \left(\frac{f}{n'_k r'_M} \right) \right] = (-Q_1) \sum_{\nu=1}^{k} \mathcal{A}_\nu \tag{85}$$

10.4. La somme de Petzval:

$$P = \sum_{\nu=1}^{k} P_\nu \quad \text{ou} \quad \mathcal{P} = \sum_{\nu=1}^{k} \mathcal{P}_\nu \tag{86}$$

10.5. La courbure de champ de l'image sagitale:

$$\left(\frac{f}{n'_k r'_S} \right) = + Q_1 \sum_{\nu=1}^{k} \mathcal{S}_\nu \tag{87}$$

10.6. La courbure de champ de l'image méridionale:

$$\left(\frac{f}{n'_k r'_M} \right) = + Q_1 \sum_{\nu=1}^{k} \mathcal{M}_\nu \tag{88}$$

10.7. La courbure moyenne de champ:

$$\left(\frac{f}{n'_k r'_W} \right) = + Q_1 \sum_{\nu=1}^{k} \mathcal{W}_\nu \tag{89}$$

10.8. La distorsion:

$$\Delta y'_B = - \frac{1}{2} (n_1 \, \sigma_{B1} \, \omega_{PE}) \, (\Omega_k \, x'_{kG}) \sum_{\nu=1}^{k} \mathcal{D}_\nu \tag{90}$$

11. L'ABERRATION CROMATIQUE. LE COEFFICIENT PARTIEL DE LA SURFACE

De l'invariant Q_ν^B donné par la relation 10, on prend la dérivée $\frac{dQ_\nu^B}{d\lambda}$ et tenant compte de la relation 14 qui nous donne:

$$n_\nu \, x_\nu^2 \, \Omega_\nu^2 = n'_{\nu-1} \, x'^2_{\nu-1} \, \Omega_{\nu-1} \tag{91}$$

et des relations:

$$n_\nu = n'_{\nu 1} \qquad\qquad \mathrm{d} x_\nu = dx'_{\nu-1} \tag{92}$$

on obtient pour les différentes surfaces sphériques:

$$\frac{dx'_1}{n'_1 x'^2_1} - \frac{dx_1}{n_1 x_1^2} = - \frac{Q_1^B dn_1}{n_1} + \frac{Q_1^B dn'_1}{n'_1} = - Q_1^B \underset{1}{\Delta'} \left(\frac{dn}{n}\right)$$

$$\frac{dx'_2}{n'_2 x_2^2 \, \Omega_2^2} - \frac{dx_2}{n_2 x_2^2 \, \Omega_2^2} = - \frac{Q_2^B}{\Omega_2^2} \underset{2}{\Delta'} \left(\frac{dn}{n}\right) \tag{93}$$

où:

$$\Delta' \left(\frac{dn}{n}\right) = \frac{dn'}{n'} - \frac{dn}{n}$$

En faisant la somme des relations 93, on obtient pour un objet sans aberrations, $dx_1 = 0$;

$$\frac{dx'_k}{n'_k \, x'^2_k \, \Omega_k^2} = - \sum_{\nu=1}^{k} \frac{Q_\nu^B}{\Omega_\nu^2} \underset{\nu}{\Delta'} \left(\frac{dn}{n}\right) \tag{94}$$

De la figure 6 et utilisant aussi les relations:

$$Q_\nu^B = \frac{1}{n_\nu}\left(\frac{x_\nu + R_\nu}{R_\nu \, n_\nu}\right); \quad \frac{Q_\nu^B dn_\nu}{n_\nu \operatorname{tg} \alpha_\nu} = \frac{dn_\nu}{n_\nu^2 R_\nu i_{\alpha\nu}}\,; \qquad \operatorname{tg} \alpha_\nu \approx \frac{h_{\alpha\nu}}{R_\nu};$$

$$\frac{x_\nu}{\varepsilon_{\alpha\nu}} \approx \frac{R_\nu}{\sigma_{\alpha\nu}}; \quad \operatorname{tg} \alpha_1 \approx \frac{h_{\alpha 1}}{R_1} \equiv \frac{h_1}{R_1}; \quad n_\nu \varepsilon_{\alpha_\nu} \approx n'_\nu \varepsilon'_{\alpha_\nu}$$

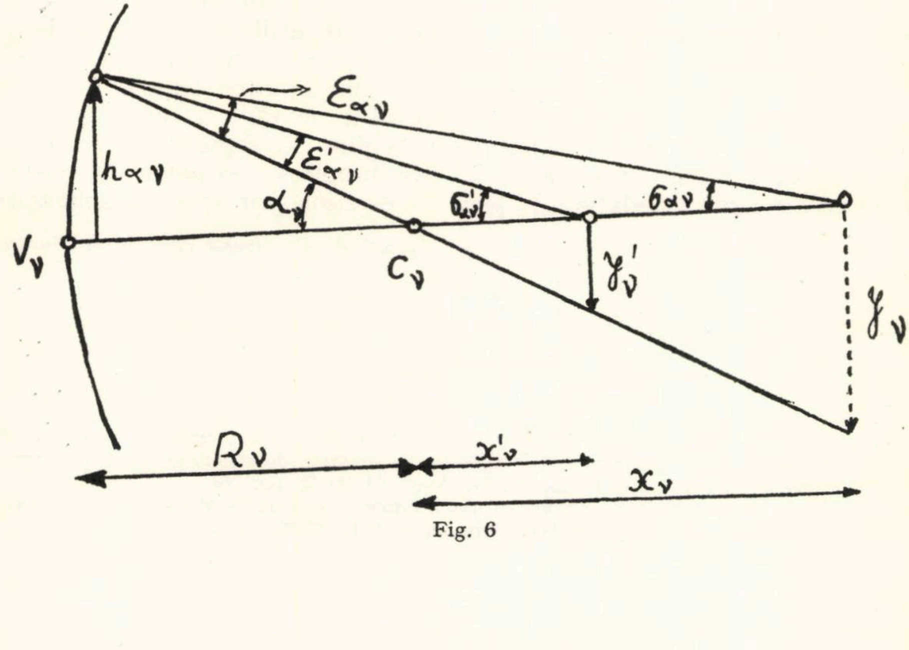

$\varepsilon_{\alpha\nu}$
$\varepsilon'_{\alpha\nu}$
$h_{\alpha\nu}$
α_ν
$\sigma'_{\alpha\nu}$
$\sigma_{\alpha\nu}$
V_ν
C_ν
y'_ν
y_ν
R_ν
x'_ν
x_ν

Fig. 6

qui sont introduites dans la relation 94, on obtient 95

$$\frac{n'_k dx'_k}{f} = -\left(\frac{1}{f}\right)^2 (n'_k x'_k \Omega_k)^2 \sum_{\nu=1}^{k} \left(\frac{fh_1}{R_1}\right)\left(\frac{1}{R_\nu \Omega_\nu}\right)\left(\frac{1}{n_\nu \varepsilon_{\alpha\nu}}\right) \underset{\nu}{\Delta'}\left(\frac{dn}{n}\right) \tag{95}$$

Designant par $\Lambda_\nu(x')$ le coefficient partiel de l'aberration cromatique donnée par la surface ν:

$$\Lambda_\nu(x') = \left(\frac{fh_1}{R_1 R_\nu \Omega_\nu n_\nu \varepsilon_{\alpha\nu}}\right) \underset{\nu}{\Delta'}\left(\frac{dn}{n}\right) \tag{96}$$

on obtient la relation finale:

$$\frac{n' dx'_k}{f} = -\left(\frac{1}{f}\right)^2 (n'_k x'_k \Omega_k)^2 \sum_{\nu=1}^{k} \Lambda_\nu(x') \tag{97}$$

ou:

$$\frac{n' dx'_k}{f} = -\left(\frac{1}{f}\right)^2 (n'_k x'_k \Omega_k)^2 \Lambda(x') \tag{98}$$

avec:

$$\Lambda(x') = \sum_{\nu=1}^{k} \Lambda_\nu(x') \tag{99}$$

12. CONCLUSIONS

Les résultats obtenus dans cet ouvrage nous montrent que la méthode donnée par Flügge dans l'ouvrage [1] peut être utilisée aussi dans le cas dans lequel les distances de l'objet et des images sont mesurées par rapport aux centres des dioptres sphériques du système optique centré.

La méthode développée dans le présent ouvrage a conduit aussi à la déduction des relations qui ont un sens plus physique, par exemple la relation 10 où l'on met en évidence le chemin optique, et aussi aux relation tout neuves comme la relation 28 pour l'aberration principale de sphéricité.

Faculté de Physique-Université de Bucarest

BIBLIOGRAPHIE

1. Johannes Flügge: „Das Photographische Objectiv", Wien, Springer Verlag, 1955.
2. G. G. Brătescu: „Contributions à l'étude de l'aberration de sphéricité du dioptre sphérique", Anal. Univ. București, 34, Anul XI (1962) pg. 291.
3. G. G. Brătescu: „Metoda prismei și aberațiunile principale de sfericitate și cromatice la dioptrul sferic", Rev. Fiz. Chim., A, Vol. I, (1964), pg. 287.

CALCULUS OF EFFICIENT CROSS-SECTIONS OF EXCITATION TRANSFER BY ATOMIC COLLISIONS. THE CASE OF ALKALINE ATOMS OF VARIOUS TYPES

ST. TUDORACHE

The paper deals with the dntermination of various cross-section leading to the excitation transfer due to collisions betweeen excited alkaline atoms and alkaline atoms of another type which are in the ground state. The particular case is analysed of collisions between optically excitnd K atoms on the resonance levels and the Rb atoms in the ground state. The discussion holds also when no trapping of the resonance radiations occurs.

1. INTRODUCTION

Numerous authors have been concerned with the transfer of electronic excitation between the two levels $^2P_{1/2}$ and $^2P_{3/2}$ of the resonance doublet of alkaline atoms, as a result of the interaction with a heavy particle (atom or molecule). Various works have tackled the collisions among alkaline atoms of the same kind [1—3], between alkaline atoms and atoms of noble gases [4, 5], between alkaline atoms and molecules [6—8]. There are, however, few works which have studied the collisions between two alkaline atoms of various kinds [9—11].

The present paper points to the determination of various efficient excitation transfer cross-sections due to binary collisions between two alkaline atoms of various kind, under consideration of the most probably occuring processes. For the sake of exemplification, we shall analyse the collision between an excited K atom on one of its resonance levels and a Rb atom in the ground state.

2. DISCUSSION OF INTERVENING PROCESSES

If the mixture of K and Rb vapours, at low pressure, is illuminated by a component of the K doublet resonance, then the resulting fluorescence includes the component present in the incident light (resonance fluorescence) but also other components which appear as a result of the excitation transfer by collision (sensitive fluorescence).

The fluorescence radiation includes both the *K* and the *Rb* resonance doublets. The presence of spectral lines others than those used for the optical excitation, is due to inelastic collisions between excited and non-excited *K* atoms, between excited *K* atoms and *Rb* atoms in the ground state, collisions which bring about the excitation transfer from *K* atoms to *Rb* atoms as well as the mixing of the resonance levels of *K* and *Rb* atoms.

Processes which become apparent when the mixture of *K* and *Rb* vapours is steadily illuminated by the D_2 component of the *K* resonance doublet, are represented in fig. 1.

The process of the mixture of $4^2P_{1/2}$ and $4^2P_{3/2}$ *K* states by the collision of excited *K* atoms with *K* atoms in the ground state may be represented as:

$$K(4^2P_{3/2}) + K(4^2S_{1/2}) \rightleftarrows K(4^2P_{1/2}) + K(4^2S_{1/2}) + \Delta E \tag{1}$$

where ΔE stands for the energetic difference between the two states $2P_{3/2,\,1/2}$ which are converted into kinetic energy of the relative motion of colliding atoms.

The process of the mixture of $5^2P_{1/2}$ and $5^2P_{3/2}$ states *Rb* atoms is represented by an analogous relation.

The transfer of excitation energy from the *K* atoms to the *Rb* atoms may be represented by the relations

$$K(4^2P_{3/2,\,1/2}) + Rb(5^2S_{1/2}) \rightarrow K(4^2S_{1/2}) + Rb(5^2P_{3/2,\,1/2}) + \Delta E \tag{2}$$

where ΔE bears the same physical significance as in relation (1).

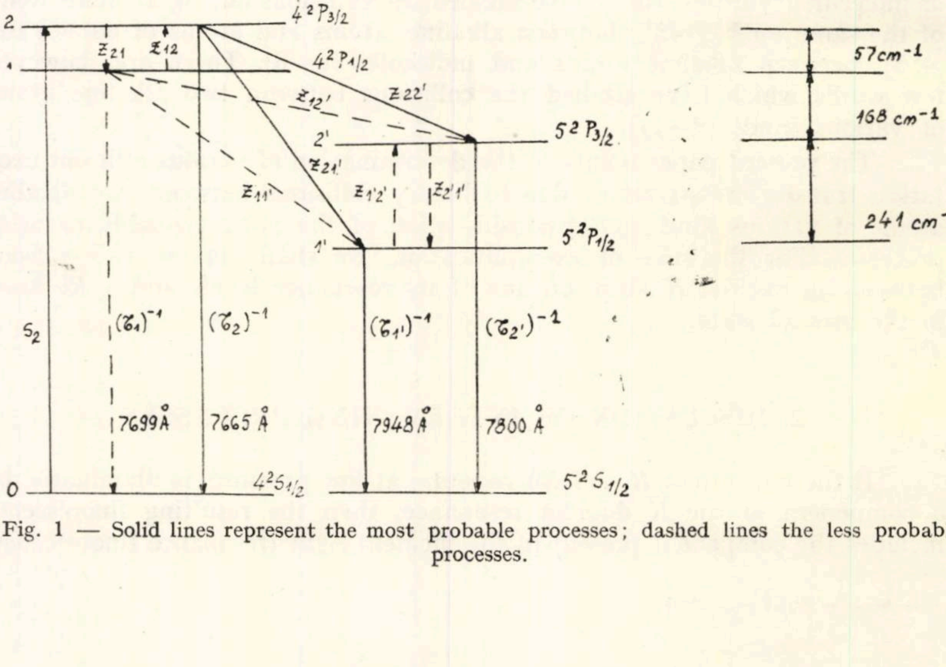

Fig. 1 — Solid lines represent the most probable processes; dashed lines the less probable processes.

Generally we may consider that the ΔE values are separated quite wel în order to enable a clear distinction among the various efficient cros-sections.

By the optical excitation with component D_2 ($\lambda = 7665$ Å) of K the various processes may be represented by the following relations

$$K(4^2S_{1/2}) + h\nu_2 \xrightarrow{S_2} K(4^2P_{3/2}) \tag{3}$$

$$K(4^2P_{3/2}) + Rb(5^2S_{1/2}) \xrightarrow{Z_{22'}} K(4^2S_{1/2}) + Rb(5^2P_{3/2}) \tag{4}$$

$$K(4^2P_{3/2}) + Rb(5^2S_{1/2}) \xrightarrow{Z_{21'}} K(4^2S_{1/2}) + Rb(5^2P_{1/2}) \tag{5}$$

$$K(4^2P_{1/2}) + Rb(5^2S_{1/2}) \xrightarrow{Z_{12'}} K(4^2S_{1/2}) + Rb(5^2P_{3/2}) \tag{6}$$

$$K(4^2P_{1/2}) + Rb(5^2S_{1/2}) \xrightarrow{Z_{11'}} K(4^2S_{1/2}) + Rb(5^2P_{1/2}) \tag{7}$$

$$K(4^2P_{1/2}) \xrightarrow{(\tau_1)^{-1}} K(4^2S_{1/2}) + h\nu_1 \tag{8}$$

$$K(4^2P_{3/2}) \xrightarrow{(\tau_2)^{-1}} K(4^2S_{1/2}) + h\nu_2 \tag{9}$$

$$K(4^2P_{3/2}) + M(^2S_{1/2}) \xrightarrow{Z_{21}} K(4^2P_{1/2}) + M(^2S_{1/2}) \tag{10}$$

$$Rb(5^2P_{1/2}) \xrightarrow{(\tau_{1'})^{-1}} Rb(5^2S_{1/2}) + h\nu_{1'} \tag{11}$$

$$Rb(5^2P_{3/2}) \xrightarrow{(\tau_{2'})^{-1}} Rb(5^2S_{1/2}) + h\nu_{2'} \tag{12}$$

Where S_2 = density of excited K atoms/sec from the $4^2S_{1/2}$ in the $4^2P_{3/2}$ state; Z with various indices stands for the number of collisions per second undergone by a K atom related to the energy transfer without radiation; τ_1; τ_2; $\tau_{1'}$ and $\tau_{2'}$ mean life time of the excited states $4^2P_{1/2}$, $4^2P_{3/2}$, $5^2P_{1/2}$, $5^2P_{3/2}$ of K resp. Rb.

3. THEORETICAL STUDY

At the dynamic equilibrium of the mixture of K and Rb atoms, implying the steady optical excitation of the $4^2P_{1/2}$ (or $4^2P_{3/2}$) state of K, spontaneous transitions and primary collision processes, we may write the evolution in time of the population of atomic levels.

By the steady excitation with D_1 radiation (7699 Å) of K we obtain

$$\frac{dN(4^2P_{1/2})}{dt} = S_1 + Z_{21} \cdot N(4^2P_{3/2}) - N(4^2P_{1/2}) \cdot [(\tau_1)^{-1} + Z_{12} + Z_{12'} + Z_{11'}] = 0 \tag{13}$$

$$\frac{dN(4^2P_{3/2})}{dt} = Z_{12} \cdot N(4^2P_{1/2}) - N(4^2P_{3/2}) \cdot [(\tau_2)^{-1} + Z_{21} + Z_{22'} + Z_{21'}] = 0 \tag{14}$$

where $N(4^2P_{1/2})$ and $N(4^2P_{3/2})$ represents the densities of K atoms in the respective states and the remaining magnitudes have the same significance as above.

By the steady excitation with D_2 (7665 Å) radiation, of K, we obtain:

$$\frac{dN(4^2P_{3/2})}{dt} = S_2 + Z_{12} \cdot N(4^2P_{1/2}) - N(4^2P_{3/2})\,[(\tau_2)^{-1} + \\ + Z_{21} + Z_{22'} + Z_{21'}] = 0 \tag{15}$$

$$\frac{dN(4^2P_{1/2})}{dt} = Z_{21} \cdot N(4^2P_{3/2}) - N(4^2P_{1/2}) \cdot [(\tau_1)^{-1} + \\ + Z_{12} + Z_{12'} + Z_{11'}] = 0 \tag{16}$$

Let us follow now the variation in time of the population of the levels $5^2P_{1/2,\,3/2}$ *Rb* on excitation of K atoms with the D_1 or D_2 radiation, and during collision processes of the II kind when the respective levels will be populated, in accordance with figure 1.

On excitation with the D_1 (7699 Å) radiation of K we obtain

$$\frac{dN(5^2P_{3/2})}{dt} = N(4^2P_{1/2}) \cdot Z_{12'} + N(5^2P_{1/2}) \cdot Z_{1'2'} - \\ - N(S^2P_{3\,2}) \cdot [Z_{2'1'} + (\tau_2')^{-1}] = 0 \tag{17}$$

$$\frac{dN(5^2P_{1/2})}{dt} = N(4^2P_{1/2}) \cdot Z_{11'} + N(5^2P_{3/2}) \cdot Z_{2'1'} - \\ - N(5^2P_{1/2}) \cdot [Z_{1'2'} + (\tau_1')^{-1}] = 0 \tag{18}$$

while on excitation with the D_2 (7665 Å) of K:

$$\frac{dN(5^2P_{3/2})}{dt} = N(4^2P_{3/2}) \cdot Z_{22'} + N(5^2P_{1/2}) \cdot Z_{11'} - \\ - N(5^2P_{3/2})[(\tau_2')^{-1} + Z_{2'1'}] = 0 \tag{19}$$

$$\frac{dN(5^2P_{1/2})}{dt} = N(4^2P_{3/2}) \cdot Z_{21'} + N(5^2P_{3/2}) \cdot Z_{2'1'} - \\ - N(5^2P_{1/2})\,[(\tau_1')^{-1} + Z_{1'2'}] = 0 \tag{20}$$

where $Z_{2'1'}$ and $Z_{1'2'}$ are the number of collisions/sec undergone by an excited *Rb* atom related to the excitation transfer between the two resonance levels, due to collisions both with *Rb* and K atoms in the ground state. When excited with $D_{1'}$ we neglect $Z_{22'}$ and $Z_{21'}$ and when excited with $D_{2'}$ then $Z_{12'}$ and $Z_{11'}$ are neglected as highly improbable. At dynamic equilibrium (under stationary conditions) the variation in time of the population of the resonance levels is null. From the system of equations we shall have to determine Z with various indices in order to possibly determine the efficient cross-sections attached to each nonradiative transfer process of the excited energy.

Z with various indices is related to the efficient excitation transfer cross-sections by the formula

$$Zab = N_0 \cdot Qab \cdot \bar{v}_r \tag{21}$$

where N_0 = density of Rb atoms in the ground state

$\bar{v}_r$ = mean relative velocity of the two colliding partners, determined in accordance with the kinetic theory of gases in relation:

$$\bar{v}_r = \sqrt{\frac{8RT}{\pi}\left(\frac{1}{M_1} + \frac{1}{M_2}\right)} \tag{22}$$

where M_1 and M_2 are the interacting molecular masses. Eq. (13)—(20) should contain experimentally measurable magnitudes or most accurate magnitudes from the literature. The life times of resonance levels are assumed as known and instead of the levels' populations we shall use intensities of the fluorescence radiations.

The intensities depend on the populations of the respective levels, according to relation

$$I_{ij} = A_{ij} \cdot N_i \tag{23}$$

In the particular case of resonance levels we have

$$\left.\begin{aligned} I(7665\,\text{Å}) &= (\tau_2)^{-1} \cdot N(4^2P_{3/2})\,; \quad I(7948\,\text{A}) = (\tau_1')^{-1} \cdot N(5^2P_{1/2}) \\ I(7699\,\text{Å}) &= (\tau_1)^{-1} \cdot N(4^2P_{1/2})\,; \quad I(7800\,\text{Å}) = (\tau_2')^{-1} \cdot N(5^2P_{3/2}) \end{aligned}\right\} \tag{24}$$

where I = intensity of the fluorescence with the respective wavelength

Using (24), relations (14) and (16) become

$$Z_{12} - \frac{(\tau_1)^{-1}}{(\tau_2)^{-1}} \cdot \eta_{12}[(\tau_2)^{-1} + Z_{21} + Z_{22'} + Z_{21'}] = 0 \tag{25}$$

$$Z_{21} - \frac{(\tau_2)^{-1}}{(\tau_1)^{-1}} \cdot \eta_{21}[(\tau_1)^{-1} + Z_{12} + Z_{12'} + Z_{11'}] = 0 \tag{26}$$

where we have denoted

$$\eta_{12} = \frac{I(7665\text{Å})}{I(7699\text{Å})} \quad \text{and} \quad \eta_{21} = \frac{I(7699\text{Å})}{I(7665\text{Å})} \tag{26'}$$

The magnitudes η represent the ratio of the sensitive fluorescence intensity to the resonance fluorescence. Therefore the radiation intensity of the numerator is that of the fluorescence radiation with the same wavelength as that of the excited radiation.

BUDAPESTI MŰSZAKI EGYETEM KÖZPONTI KÖNYVTÁRA 1848

From (17) and (18) we obtain analogously

$$Z_{12'} + \frac{(\tau_1)^{-1}}{(\tau_1')^{-1}} \cdot \eta_{11'} \cdot Z_{1'2'} - \frac{(\tau_1)^{-1}}{(\tau_2')^{-1}} \cdot \eta_{12'} \cdot [Z_{2'1'} + (\tau_2')^{-1}] = 0 \tag{27}$$

$$Z_{11'} + \frac{(\tau_1)^{-1}}{(\tau_2')^{-1}} \cdot \eta_{12'} \cdot Z_{2'1'} - \frac{(\tau_1)^{-1}}{(\tau_1')^{-1}} \cdot \eta_{11'} \cdot [Z_{1'2'} + (\tau_1')^{-1}] = 0 \tag{28}$$

with

$$\eta_{11'} = \frac{I(7948\ \text{Å})}{I(7699\ \text{Å})} \quad \text{and} \quad \eta_{12'} = \frac{I(7800\ \text{Å})}{I(7699\ \text{Å})} \tag{28'}$$

From eq. (19) and (20) it results

$$Z_{22'} + \frac{(\tau_2)^{-1}}{(\tau_1')^{-1}} \cdot \eta_{21'} \cdot Z_{1'2'} - \frac{(\tau_2)^{-1}}{(\tau_2')^{-1}} \cdot \eta_{22'} \cdot [Z_{2'1'} + (\tau_2')^{-1}] = 0 \tag{29}$$

$$Z_{21'} + \frac{(\tau_2)^{-1}}{(\tau_2')^{-1}} \cdot \eta_{22'} \cdot Z_{2'1'} - \frac{(\tau_2)^{-1}}{(\tau_1')^{-1}} \cdot \eta_{21'} \cdot [Z_{1'2'} + (\tau_1')^{-1}] = 0 \tag{30}$$

with

$$\eta_{21'} = \frac{I(7948\ \text{Å})}{I(7665\ \text{Å})} \quad \text{and} \quad \frac{I(7800\ \text{Å})}{I(7665\ \text{Å})} = \eta_{22'} \tag{30'}$$

From (13) and (15) result

$$1 + Z_{21} \cdot \frac{N(4^2P_{3/2})}{S_1} - \frac{N(4^2P_{1/2})}{S_1} \cdot [(\tau_1)^{-1} + Z_{12} + Z_{12'} + Z_{11'}] = 0 \tag{31}$$

$$1 + Z_{12} \cdot \frac{N(4^2P_{1/2})}{S_2} - \frac{N(4^2P_{3/2})}{S_2} \cdot [(\tau_2)^{-1} + Z_{21} + Z_{22'} + Z_{21'}] = 0 \tag{32}$$

The number of K atoms, optically excited/sec., from the ground state in the resonance states, is given by

$$S_1 = I_1 \sigma_1 N(4^2S_{1/2}) \quad \text{and} \quad S_2 = I_2 \sigma_2 N(4^2S_{1/2}) \tag{33}$$

where I_1 and I_2 = intensity of the incident light D_1 and D_2;

σ_1 and σ_2 = efficient absorption cross-section of D_1 resp. D_2 with $\sigma_2 = 2\sigma_1$

The values of Z with various indices result from the experimental measurement of η ratios and of the intensity of the incident light, in accordance with eqs. (27)—(31). The efficient excitation transfer cross-sections are determined by a relation of the type (21). The above calculations also hold whenever the trapping of the resonance radiation is lacking.

4. PARTICULAR CASES

a) Due to the relatively small probability of the occurence of the mixture of *Rb* resonance levels, in eqs. (17)—(20), $Z_{1'2'}$ and $Z_{2'1'}$ may be neglected.

In the case of the excitation of the mixture of *K-Rb* vapours with the D_1 radiation of *K*, processes (4), (5) and (9) are highly improbable as compared to the other processes; similarly, when exciting the mixture with the D_2 radiation of *K*, processes (6)—(8) may be neglected as to the other processes.

These considerations enable the simplification of the calculus leading to the efficient excitation transfer cross-section from the *K* to the *Rb* atom.

Under this circumstances, eqs. (17)—(20) become

$$\left.\begin{aligned} N(4^2P_{1/2}) \cdot Z_{12'} - N(5^2P_{3/2}) \cdot (\tau_2')^{-1} &= 0 \\ N(4^2P_{1/2}) \cdot Z_{11'} - N(5^2P_{1/2}) \cdot (\tau_1^2)^{-1} &= 0 \\ N(4^2P_{3/2}) \cdot Z_{22'} - N(5^2P_{3/2}) \cdot (\tau_2')^{-1} &= 0 \\ N(4^2P_{3/2}) \cdot Z_{21'} - N(5^2P_{1/2}) \cdot (\tau_1')^{-1} &= 0 \end{aligned}\right\} \tag{34}$$

Using (24) these relations become:

$$\begin{aligned} Z_{12'} &= (\tau_1)^{-1} \cdot \eta_{12'} \quad \text{and} \quad Z_{11'} = (\tau_1)^{-1} \cdot \eta_{11'} \\ Z_{21'} &= (\tau_2)^{-1} \cdot \eta_{21'} \quad \text{and} \quad Z_{22'} = (\tau_2)^{-1} \cdot \eta_{22'} \end{aligned} \tag{35}$$

where $\eta_{11'}$; $\eta_{12'}$; $\eta_{21'}$ and $\eta_{22'}$ have the above significances. These relations, which Krause [10] has deduced, have been used by him to determine experimentally the efficient cross-sections of excitation transfer, from the excited *K* atoms, to the *Rb* atoms in the ground state.

b) In the experimental conditions where the number of collisions $Z_{11'}$; $Z_{12'}$; $Z_{21'}$; $Z_{22'}$; $Z_{1'2'}$ and $Z_{2'1'}$ have small, negligible values, as compared to $(\tau_1)^{-1}$ and $(\tau_2)^{-1}$ [11], eqs (14) and (16) become:

$$\left.\begin{aligned} Z_{12} \cdot N(4^2P_{1/2}) - N(4^2P_{3/2}) \cdot [(\tau_2)^{-1} + Z_{21}] &= 0 \\ Z_{21} \cdot N(4^2P_{3/2}) - N(4^2P_{1/2}) \cdot [(\tau_1)^{-1} + Z_{12}] &= 0 \end{aligned}\right\} \tag{36}$$

Besides by assuming that: $\tau_1 = \tau_2 = \tau$ these equations yield the following solutions for Z_{12} and Z_{21}

$$Z_{12} = \frac{1}{\tau} \frac{\eta_{12} + \eta_{12} \cdot \eta_{21}}{1 - \eta_{12} \cdot \eta_{21}}; \qquad Z_{21} = \frac{1}{\tau} \frac{\eta_{21} + \eta_{12}\eta_{21}}{1 - \eta_{12}\eta_{21}} \tag{37}$$

where η_{12} and η_{21} have the significance in (26′).

In addition, when η_{12} and η_{21} are very small, their product in negligible so that (37) becomes

$$Z_{12} = \frac{\eta_{12}}{\tau} \quad \text{and} \quad Z_{21} = \frac{\eta_{21}}{\tau} \tag{38}$$

Since Z_{12} and Z_{21} include contributions of the collisions, between K atoms and K and Rb atoms in their ground state, we may write:

$$\left.\begin{aligned} Z_{12} &= (Z_{12})' + (Z_{12})'' \\ Z_{21} &= (Z_{21})' + (Z_{21})'' \end{aligned}\right\} \tag{39}$$

Where $(Z_{12})'$ and $(Z_{21})''$ refer to the collisions between excited K atoms and K atoms in the ground state, and $(Z_{12})''$ and $(Z_{21})''$ refer to the collisions between excited K atoms and Rb atoms in the ground state.

When the experimental cell has only K atoms in the ground state and excited, then $(Z_{12})'$ and $(Z_{21})'$ may be found by rel. (39). Knowing the number of $(Z_{12})'$ and $(Z_{21})'$ collisions the corresponding efficient cross-sections may be found by a relation of the type (21). In the case of the mixture under consideration, if we know Z_{12} from (38) and $(Z_{12})'$, we may determine $(Z_{12})''$ from (39) and the corresponding efficient cross-section.

The principle of the detailed equilibrium states that the two efficient cross-sections Q_{12} and Q_{21} satisfy relation

$$\frac{Q_{12}}{Q_{21}} = \frac{g_2}{g_1} \cdot e^{-\frac{\Delta E}{kT}} \tag{40}$$

where g_1 and g_2 = statistical weights of the states $4^2P_{1/2}$ and $4^2P_{3/2}$, and ΔE = energetic difference among states.

Polytechnic Institute Bucharest
Laboratory of Physics

5. CONCLUSIONS

By the experimental measurement of the ratios of relative intensity of the sensitive fluorescence/resonance fluorescence, we may determine the efficient mixture cross-sections of resonance levels as well as those of excitation transfer from one alkaline atom to the other, by collisions. Collisions where the kinetic energy of the relative motion of colliding particles is converted into excitation energy have not been considered. The discussion has zaken into account only the most probable processes and in the case when the trapping of the resonance radiation is neglected. To fulfill this last condition one should use partial pressures of every vapour in the mixture, which should be smaller than 10^{-5} mm Hg. In some particular cases the relations are simplified by actually obtaining relations previously deduced by Krause.

Acknowledgement. The autor gratefully acknowledges the steady guidance and help of Professor I. Agârbiceanu and Professor G. Brătescu throughout this contributions.

LITERATURE

[1] J. Jordan, P. Franken, Phys. Rev. *142*, 20, 1966.
[2] A. Rae, L. Krause, Can. J. Phys. *43*, 1574, 1965.
[3] J. Pite, L. Krause, Can. J. Phys. *46*, 125, 1968.
[4] M. Czajkowski, L. Krause, Can. J. Phys. *44*, 752, 1966.
[5] G. Chapman, L. Krause, Can. J. Phys. *44*, 753, 1966.
[6] B. Kible, G. Koply, L. Krause, Phys. Rev. *159*, 11, 1967.
[7] M. Stupavsky, L. Krause, Can. J. Phys. *46*, 2127, 1968, *47*, 1249, 1969.
[8] D. Mc Gillis, L. Krause, Can. d. Phys. *46*, 1051, 1968.
[9] M. Czajkowski, D. McGillis, L. Krause, Can. J. Phys. *44*, 741, 1966
[10] E. Hrycyschin, L. Krause, Can. J. Phys. *47*, 215, 1969.
[11] E. Hrycyschin, L. Krause, Can. J. Phys. *47*, 223, 1969

A NON-DESTRUCTIVE THIN-FILM FERROMAGNETIC-HALL MEMORY

I. SPÎNULESCU CARNARU and C. STĂNESCU

In ferromagnetic thin film memories, the readout of the stored bits is made by means of a drive magnetic field produced by a current pulse having very sharp rise and fall fronts [1].

This magnetic field rotates the internal magnetic field of ferromagnetic thin film. When current pulse is ceased the internal magnetic field reaches the preferential direction of magnetization corresponding to the previously stored state.

These magnetic flux variations produces signals in the output wire which are amplified, standardized and interpreted as the stored bits.

In the memory described in this paper, a non-destructive readout is performed using a thin film Hall transducer. The Hall transducer [2] was realised by vacuum deposition of the InSb semiconductor thin film and respective contacts on the ferromagnetic film. The ferromagnetic thin film was previously insulated with protected SiO_2 film. For the Hall transducer better efficiency the contacts collecting the Hall potential were deposited under and bellow the InSb thin films. The deposition of the semiconductor film was made in such a way that the preferential direction of magnetisation should be perpendicular to the direction of the current passing through transducer (Fig. 1).

The InSb thin films carriers mobility was sufficiently high, varring between 12 000 and 15 000 $cm^2/V.s$. The sensitivity of Hall transducer was 50—70 $\mu V/Oe$. The ferromagnetic thin film was 5 mm in diameter and the semiconductor thin film dimensions were 4×5 mm^2. A Hall transducer needs a current of about 5—10 mA.

The information readout from ferromagnetic film is made in the following way: when a current passes through the contacts A and B, the carriers are deflected by the internal magnetic field of the ferromagnetic film and the Hall potential appears between the contacts C and D. The sign of the Hall potential obviously depends on the magnetisation state 0 or 1. The organisation of non-destructive memory in matricial form is shown in figure 2.

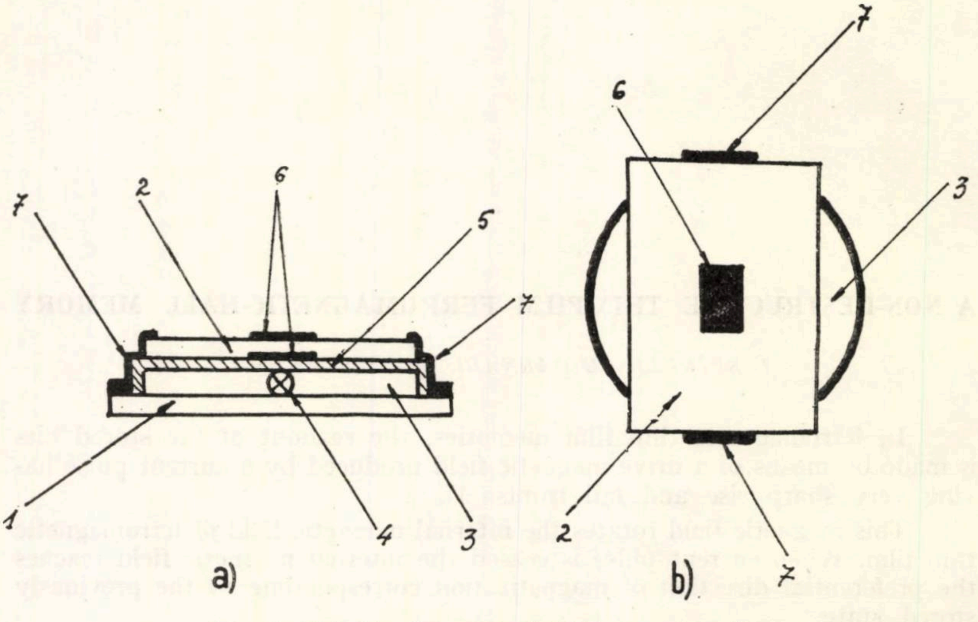

Fig. 1. Thin-film ferromagnetic-Hall memory cell.

a) Crossection view; b) View from above. 1 — Substrate; 2 — InSb thin-film; 3 — Ferromagnetic thin-film; 4 — The preferential direction of magnetisation; 5 — SiO_2 thin-film; 6 — Hall — voltage contacts; 7 — Hall current contacts.

The information writing into memory and the wiping are made in the classical way [1] and wasn't figured.

The contacts at which the current pulses are applied are parallely connected to the columns and the contacts if redout the Hall potential are connected also in parallel but on the lines. In figure 2 by dashed line was represented the Hall transducer bottom grounded contact.

One matrix contains 32 columns (corresponding to 32 bits a word) and 25 lines. For a 1024 words needs 41 such matrix.

Because the longitudinal resistance of InSb film was 250—300Ω, the column of one matrix is commanded by a current pulse of 0,3 A generated by a blocking generator of the kind described in [3]. These blocking oscillators could be commanded simultaneoulsy for every matrix when a column of the memory is interrogate. We have also used such blocking oscilators to write into memory and to wipe the memory.

For reading a memory cell on acts in the following way: on gives a current pulse in the column corresponding to the cell. Evidently, a Hall potential will appear on every cell of this column. For selection of desired line only readout amplifier corresponding to this line must be activited. In

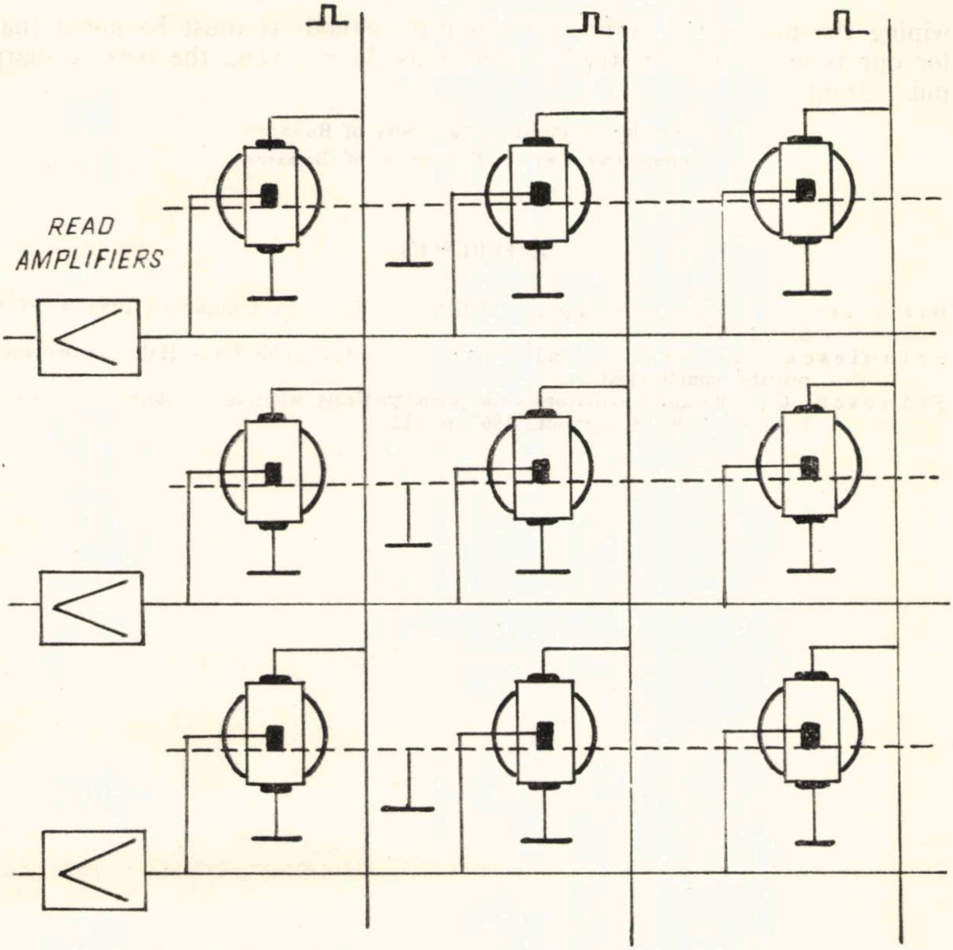

Fig. 2. Thin-Film ferromagnetic-Hall non-destructive memory matrix.

the readout amplifier the positive or negative pulses could appear according to magnetisation state (0 or 1) of the respective ferromagnetic film. At the amplifiers imputs we have obtained pulses of 400—500 μV amplitude.

For this non-destructive memory the parasite signals problem is not so critical. It must be noted that the readout occours in the same time as the current pulse is sent in the transducer. This decreases very much the memory acces time comparatively with the common ferromagnetic thin film memories where, at first, by a magnetisation process the perviously state must be achieved. Additionally, the current pulses for Hall generator must not be necessary rectangulars.

The Hall transducers could opperate at very high frequencies. The memory performancies are limited by time neaded to write the data or to wiping the memory according to classical method. It must be noted that for our type of memory these opperations do not need the perfect sharp pulse fronts.

Faculty of Physics, University of Buharest
Computrer Center, University of Buharest

REFERENCES

Bittmann, E.: „Thin-film memorias", IRE Trans. Electronic Computers, 1959, v. EC-8, p. 92–97.

Spînulescu Carnaru, I., and Stănescu, C.: „Thin-films Hall transduceres", private communication.

Stănescu, C.: „Blocking oscillators with premagnetizing winding", Automatica şi Electronica, *11*, No. 5, sept-oct., 1967, p. 232.

THREE VALUE LOGICAL CIRCUITS REALIZED WITH MOS-TRANSISTORS AND THIN-FILM TRANSISTORS

C. STĂNESCU and I. SPÎNULESCU-CARNARU

To realize three value logical circuits[1, 2, 3] may use either special MOS (metal-oxid-semiconductor) transistors[4], or thin film field-effect transistors (TFT) of the kind described by Weimer[5], Shallcross[6] and other authors[7, 8, 9].

These special transistors present pentode-like characteristics for negative, zero and positive bias on the gate electrode. A tipical family of such characteristics is shown in figure 1.

In trivalent luckasiewiczian logic the folowing logical variables are used: 0; 1/2 and 1 corresponding to the false, doubt and truth logical values respec-

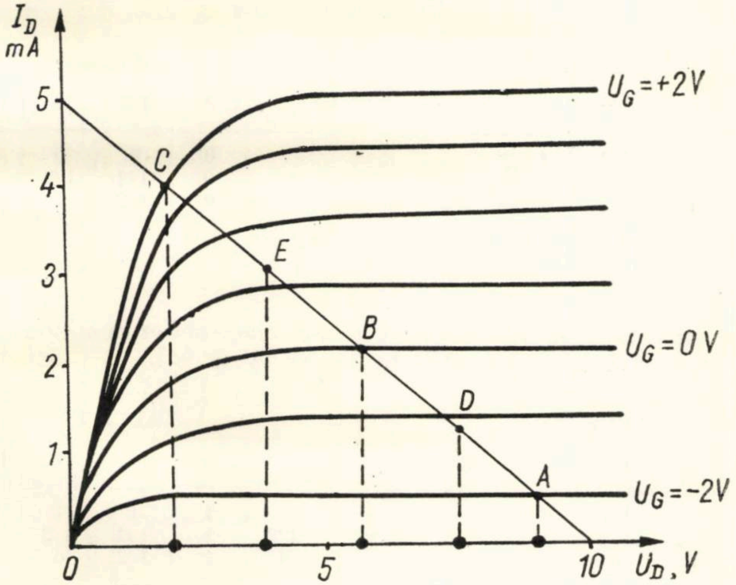

Fig. 1. The characteristics of special MOS and TFT transistors.

tively. To these logical variables the folowing values of gate bias are associated: negative potential (— 2V), zero potential and positive potential $(+2V)$. The functioning points will lay in A, B or C corresponding. For the logical variable 1, the transistor will be in conduction and on the drain electrode will appear a low potential; for the logical variable 0 the transistor will be practically blocked and on the drain electrode will be obtained a high — potential; for the logical variable 1/2 on the drain an intermediate potential will appear.

For the functions NOT and FOLLOWER the circuits from figures 2a, b are used. The clamping circuit attached to the drene electrode (Fig. 2a), and respectively to the source-electrode (Fig. 2b), has the role to change the intermediate outpout potential into the 0 potential point, and the low potential into a negative one, so that as the logical variables 0, 1/2 and 1 are obtained. These circuits work in pulses with respect to 0 potential. It is clearly sean that the NOT circuit of figure 2a, works according to table I:

TABLE I

Input	0	1/2	1
Output	1	1/2	0

and the circuit of figure 2b, repeats the input signal.

The functions OR and AND may be realized with the circuits of figures 2c and 2d. The behaviour of these circuits may be explained from tables II and III:

TABLE II

$\cup$	0	1/2	1	Input A
0	0	1/2	1	
1/2	1/2	1/2	1	
1	1	1	1	

Input
B

TABLE III

$\cap$	0	1/2	1	Input A
0	0	0	0	
1/2	0	1/2	1/2	
1	0	1/2	1	

Input
B

The circuits from figures 2 e, f realize the Sheffer functions NOR and NAND respectively the presented by tables IV (a, b):

TABLE IV-a

$A \top B$	0	1/2	1	Input A
0	1	1/2	0	
1/2	1/2	1/2	0	
1	0	0	0	

Input
B

TABLE IV-b

$A \perp B$	0	1/2	1	Input A
0	1	1	1	
1/2	1	1/2	1/2	
1	1	1/2	0	

Input
B

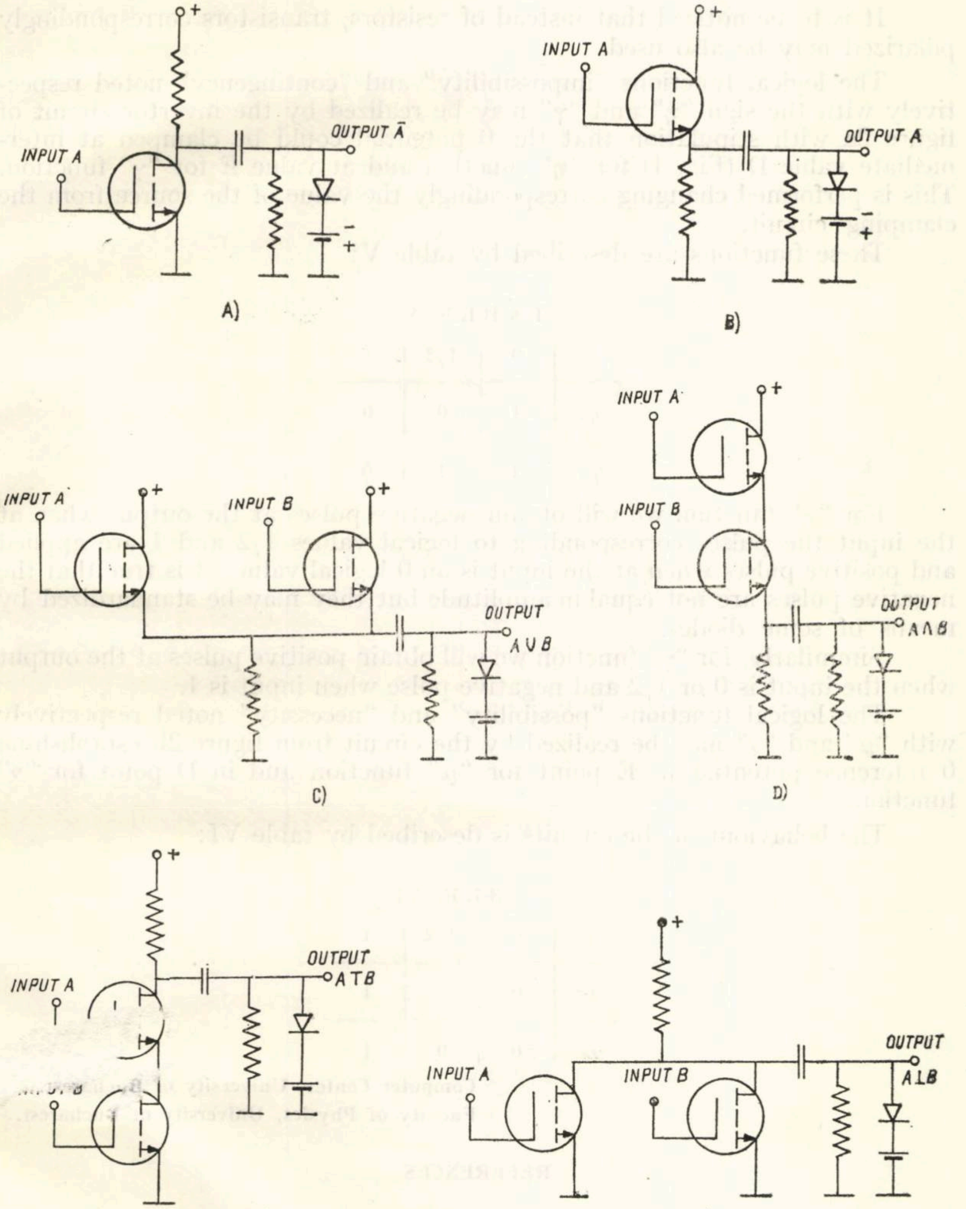
INPUT A
OUTPUT Ā
A)
INPUT A
OUTPUT A
B)
INPUT A
INPUT B
OUTPUT
A∨B
C)
INPUT A
INPUT B
OUTPUT
A∧B
D)
INPUT A
B
OUTPUT
ATB
E)
INPUT A
INPUT B
OUTPUT
A⊥B
F)

Fig. 2. Three value circuits:

a) NOT circuit; b) FOLLOWER circuit; c) OR circuit; d) AND circuit; e) NOR circuit f) NAND circuit

It is to be noticed that instead of resistors, transistors correspondingly polarized may be also used.

The logical functions "impossibility" and "contingency" noted respectively with the sign "η" and "γ" may be realized by the invertor circuit of figure 2a with stipulation that the 0 potential could be clamped at intermediate value D (Fig. 1) for "η" function and at value E for "γ" function. This is performed changing correspondingly the value of the source from the clamping circuit.

These functions are described by table V:

TABLE V

x	0	1/2	1
ηx	1	0	0
γx	1	1	0

For "η" function we will obtain negative pulses at the output when at the input the pulses corresponding to logical values 1/2 and 1 are applied and positive pulses when at the input is on 0 logical value. It is true that the negative pulses are not equal in amplitude but they may be standardized by means of some diodes.

Simmilarly, for "γ" function we will obtain positive pulses at the output when the input is 0 or 1/2 and negative pulse when input is 1.

The logical functions "possibility" and "necessity" noted respectively with "μ" and "ν" may be realized by the circuit from figure 2b establishing 0 reference potential in E point for "μ" function and in D point for "ν" function.

The behaviour of the circuits is described by table VI:

TABLE VI

x	0	1/2	1
μx	0	1	1
νx	0	0	1

Computer Center, University of Bucharest.
Faculty of Physics, University of Bucharest.

REFERENCES

Gr. C. Moisil: „Ancient and new trainings of unclassicaly logic" Ed. St. Buc. 1965.

Gr. C. Moisil: „Utilizing trivalent logics in theory of automatic mechanisms. III. Real contacts schemes. Communications of RSR Academy, March 1956 T. VI., nr. 3, p. 385.

Gr. C. Moisil: „Utilizing trivalent logics in theory of automatic mechanisms. VI. Polarized relays with instable neutro. Communications of RSR Academy, 1959, T. IX. p. 411.

R. H. Crawfort: „MOSFET in Circuit Design", Mc. Graw-Hill Company, 1967.

P. K. Weimer: „The TFT, a new thin-film-transistor". Proc. Inst. Radio Engrs., 1962, *50*, 1, 462.

F. V. Shallcross: „Evaluation of cadmium selenide films for use in the thin-film transistors", RCA Rev., 1963, *25*, p. 676–687.

*I. S*pînulescu-Carnaru and C. Stănescu: „The thin film transistors", Procedings of the General Romanian Military Academy, 7th and 8th Dec. 1966.

I. Spînulescu-Carnaru „ZnTe and InSb thin-film transistors", Electronics Letters, 1967, *3*, nr. 6, p. 268.

I. Spînulescu-Carnaru and C. Stănescu: „Transistors realized on thin film semiconductors", Automatics and Electronica, 1967, *11*, p. 225.

THE FUNDAMENTAL ABSORPTION EDGE OF THE ZINC SELENIDE

I. DIMA

INTRODUCTION

During the last ten years the optical properties of the $A^{II}B^{VI}$ type semiconductors have been studied in order to clarify their energetic structure [1—21]. Zinc selenide optical properties became also the subject of one of the most interesting study: amongst these properties the absorption coefficient being very important.

Zinc selenide absorption coefficient was determined in the monocrystal case from the reflection spectrum for a wide energy interval [3, 4] as well as for narrow one round the fundamental absorption edge [3, 4, 6, 13, 14, 15]. The determination of the monocrystal absorption coefficient is not possible in transmitted light, in the fundamental absorption domain, excepting a small energy interval near the edge. Even the edge structure of the fundamental could be studied, in the case of monocrystals, partially only in transmitted light, partially being studied in reflected one. The crystals of zinc selenide optically studied belonged to the cubic crystalline structure of sphalerite type and to the hexagonal one of wurtzite type [3, 4, 6].

The determination of the absorption coefficient, in transmitted light, both in a large and a narrow energy interval, in the fundamental absorption domain and in the fundamental absorption edge, became possible when the 0,05 μm and 0,5 μm thin films could be obtained. In transmitted light the optical absorption was obtained for layers of cubic crystalline structure up to 5,5 eV energies [16, 19]. For the same layers was obtained too, in transmitted light, the edge structure of the fundamental absorption [5, 20]. In the paper [20] the dependency of the edge structure upon the layers preparation conditions is studied. For the hexagonal crystalline structure thin films the optical absorption spectrum, in transmitted light, in the fundamental absorption domain, was obtained by us for the first time [19, 20].

In the present paper our aim is to study the edge structure dependence both upon the crystalline structure and the model temperature. The edge structure for cubic and hexagonal structure layers was studied both in transmitted and reflected light. We shall try to find the interpretation of the more significant data mentioned in this paper. It must be mentioned that a small part from the experimental data included in this paper were published in a short note [22].

EXPERIMENT

The obtaining metods of zinc selenide thin films with cubic or hexagonal structure (sphalerite or wurtzite type) are described in paper [19]. Cubic crystalline structure layers, without defects, were prepared on supports heated over 500°C (fig. 1c). The films used for the fundamental absorption edge study were generally heat treated in vacuum at 600°C for 20 minutes. The hexagonal crystalline structure films were prepared on supports heated at 340°C (fig. 1e). For studies in the fundamental absorption domain, thin films of 0.05 μm thickness set down on optical quartz were prepared. For the study of the fundamental absorption edge, 0.5 μm thick layers set down either on quartz or on glass were used.

Layers of 0.05 μm thickness allowed the absorption study, in transmitted light, towards the short wavelengths, up to 2000 Å. In fig. 2 is given the absorption spectrum, in transmitted light, for cubic (curve c) and hexagonal (curve e) crystalline structure layers: the arrows indicate the edges of the fundamental absorption. The curves were obtained by dint of quartz optics SF-4 spectrophotometer and Hitachi one.

The edge study of the fundamental absorption was made with a ISP-51 spectrograph with UF-84 chamber. The spectrograph dispersion at $\lambda = 4400$ Å was 10Å/mm. The light incident to the model was nonpolarised produced by a wolfram filament bulb. The model temperature optically studied could vary between 77°K (the liquid nitrogen boiling temperature) and that of the room. The spectrogramms were microphotometrated by dint of a MIF-4 microphotometer.

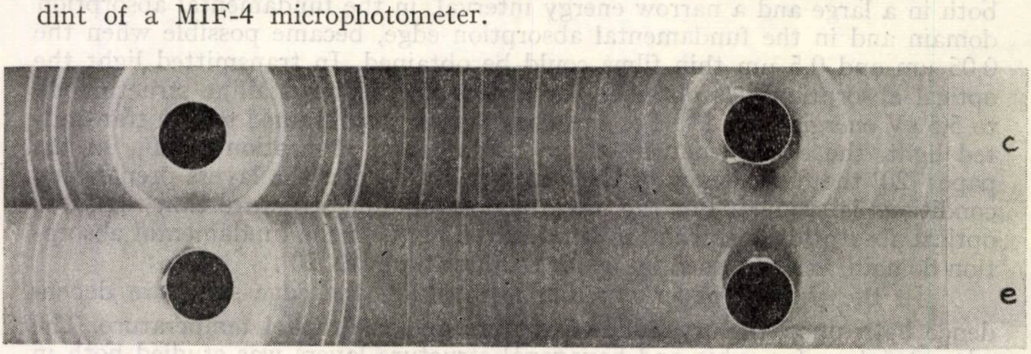

Fig. 1

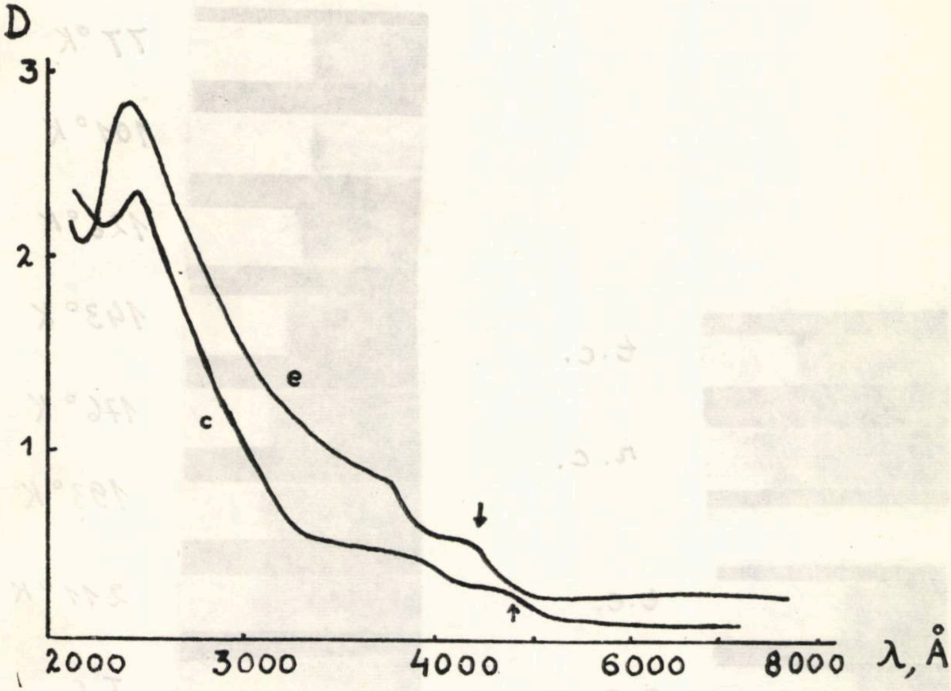

Fig. 2

RESULTS

The fundamental absorption edge, in the case of the cubic crystalline structure layers, presents at 77°K temperature, in transmitted light, a structure in which three peaks $\lambda_1 = 4427$Å, $\lambda_2 = 4408$Å, $\lambda_3 = 4360$Å can be distinguished. The three peaks can be observed on the spectrogram as well as on his microphotogram (fig. 3t.c., fig. 5t.). In reflected light, at the same model temperature, there are too three peaks displaced towards the longer wavelengths, $\lambda_1 = 4447$Å, $\lambda_2 = 4418$Å, $\lambda_3 = 4380$Å, compared with those observed in transmitted light (fig. 3r.c., fig. 5r.). The evolution of the edge absorption structure, in transmitted light, between 77°K and the room temperature (t.c.) can be followed on the spectrogramms from fig. 4 and on the microphotogramms from fig. 6. In transmited light, at 143°K, the peak from the long wavelengths side disappears and at the room temperature the absorption edge presents no more a structure. In both 4 and 6 figures, in transmitted light, it can be easily established the peaks displacement towards the long wavelengths side when the temperature raises. The middle peak (whose position can be more accurately determined), in 77°—110°K temperature range has a 0.1Å/grd displacement, and in 110°K-chamber temperature

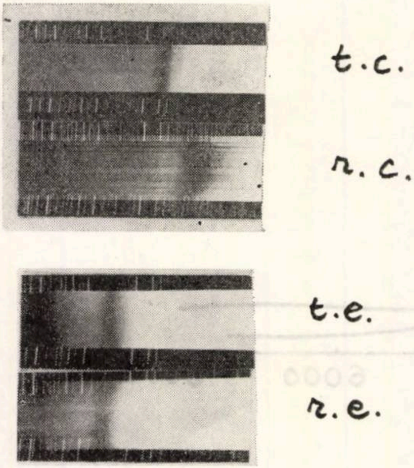

Fig. 3

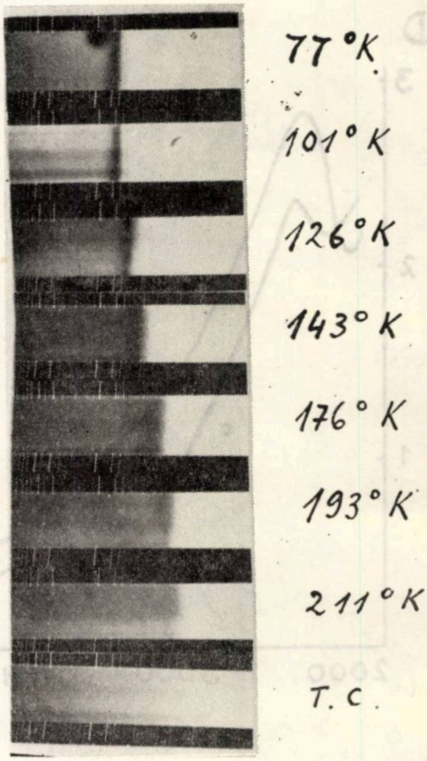
77 °K
101° K
126°K
143° K
176° K
193°K
211°K
T. C

Fig. 4

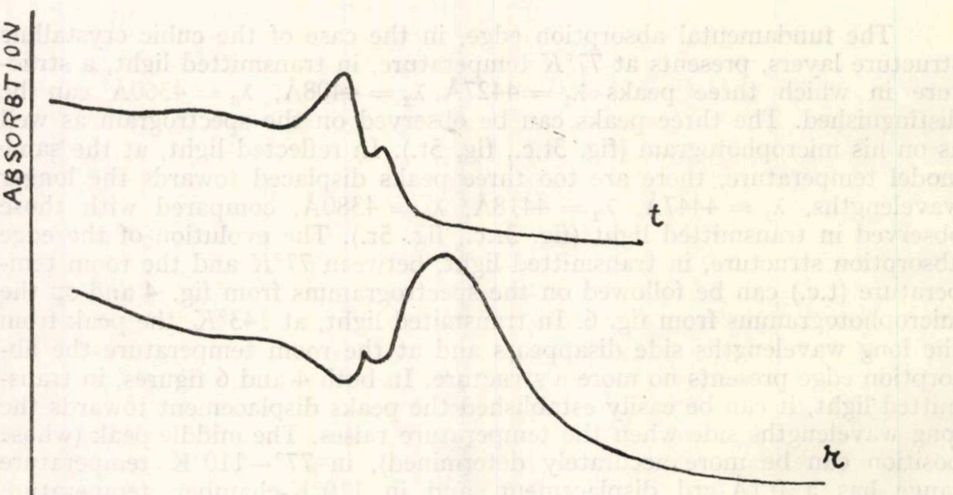

Fig. 5

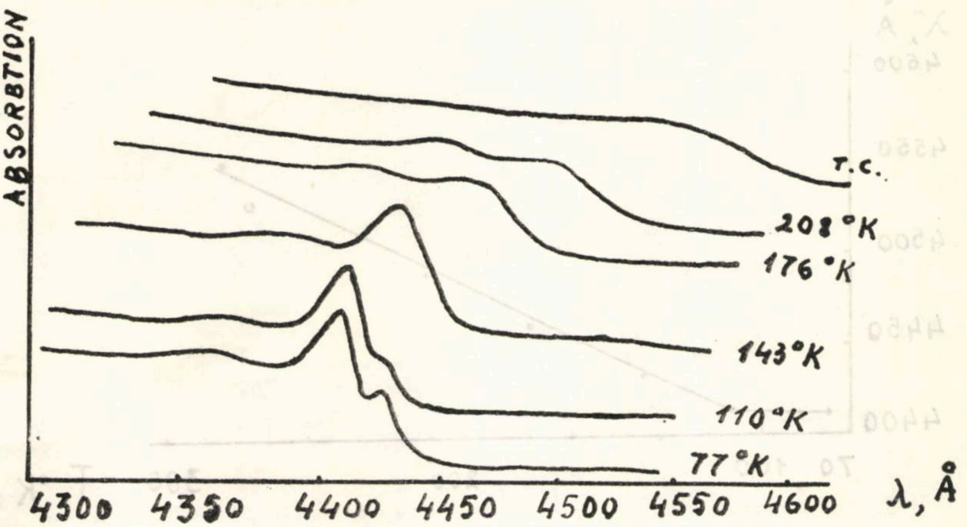

Fig. 6

range has a 0.8Å /grd one (fig. 7). In reflected light we established, apart from the transmitted light, that the middle peak disapears first and only at temperatures near the chamber one peak from the longer wavelengths side as well disapears (fig. 8 and 9). In reflected light, at chamber temperature, the fundamental absorption edge presents no more structure too. We noticed the same rule also for the peak displacement with the temperature towards the long wavelengths side, in reflected light.

In the case of the hexagonal crystalline structure thin films the fundamental absorption edge, at 77°*K* temperature, presents a structure both in transmitted and reflected light. In transmitted light the fundamental absorption edge shows two peaks $\lambda_1 = 4357$Å, $\lambda_2 = 4283$Å (fig. 3t.e., fig. 10t). In reflected light we established the existence of two peaks slightly displaced towards short wavelengths side compared with the peaks observed in transmitted light (fig. 3r,e., fig. 10r). Watching the edge structure dependenceu pon the temperature, in transmitted light, in the case of the hexagonal crystalline structure we see that at the same time with their displacement towards the long wavelengths side the two peaks are gradually diminishing when the model temperature raises (fig. 11 and 12). Nevertheless the two peaks can be observed near up to the chamber temperature. The peaks displacement between 77°K and 120°K is 0.25Å/grd and between 120°K and chamber temperature is 0.83Å/grd (fig. 13). In reflected light, the edge structure shows the same rule as the structure observed in transmitted light (fig. 14 and 15).

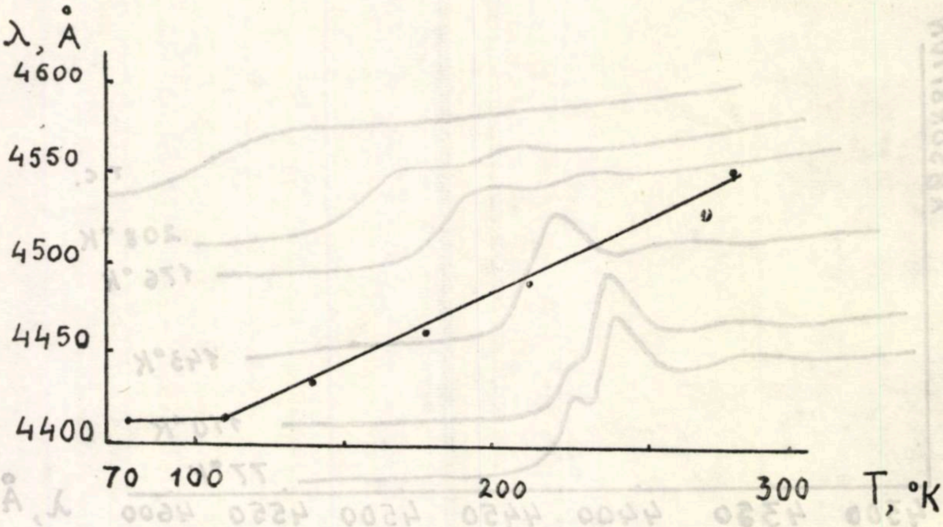
λ, Å
4600
4550
4500
4450
4400
70
100
200
300
T, °K

Fig. 7

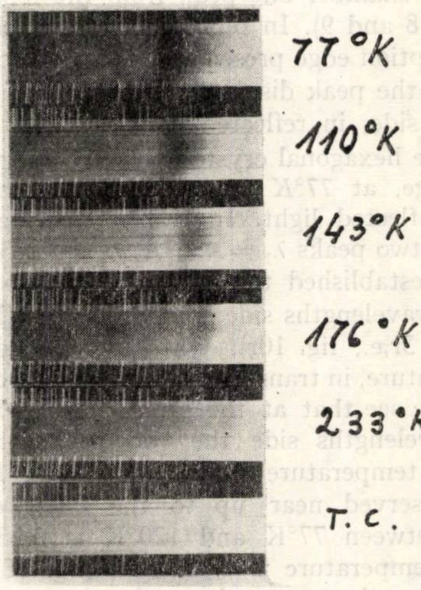
77°K
110°K
143°K
176°K
233°K
T. C.

Fig. 8

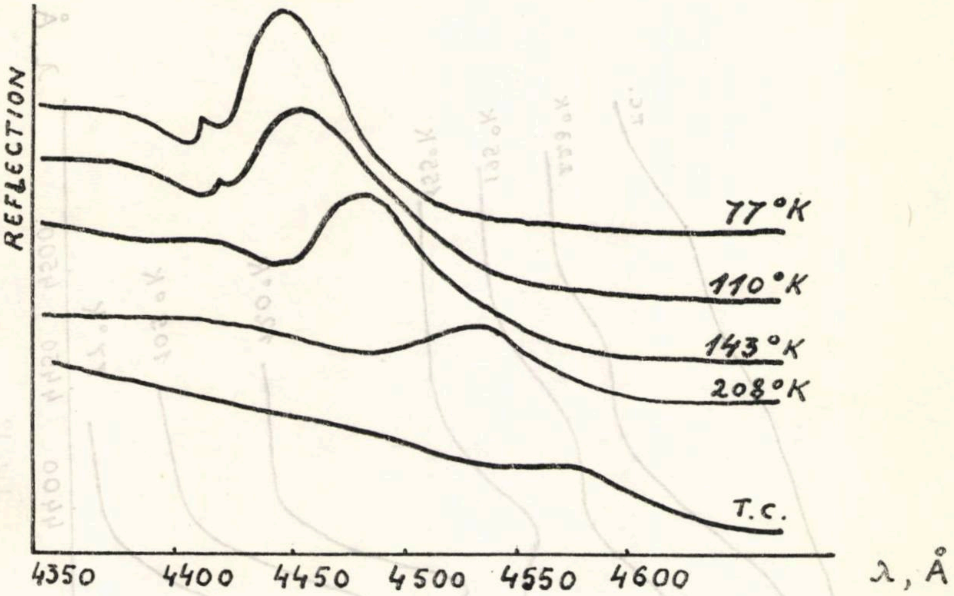
REFLECTION
77°K
110°K
143°K
208°K
T.c.
4350
4400
4450
4500
4550
4600
λ, Å

Fig. 9

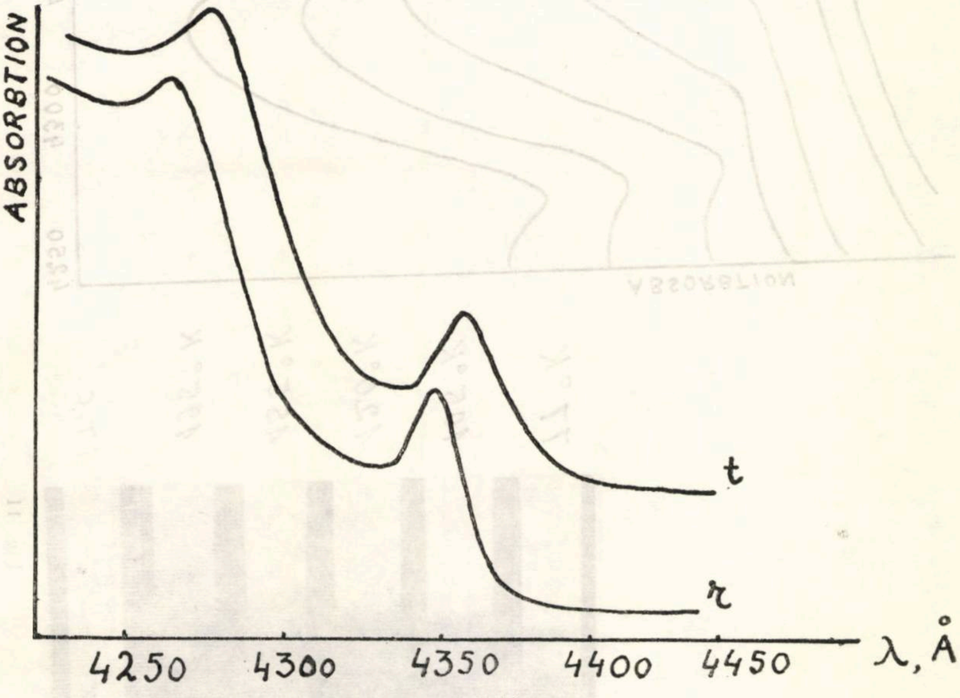
ABSORBTION
t
r
4250
4300
4350
4400
4450
λ, Å

Fig. 10

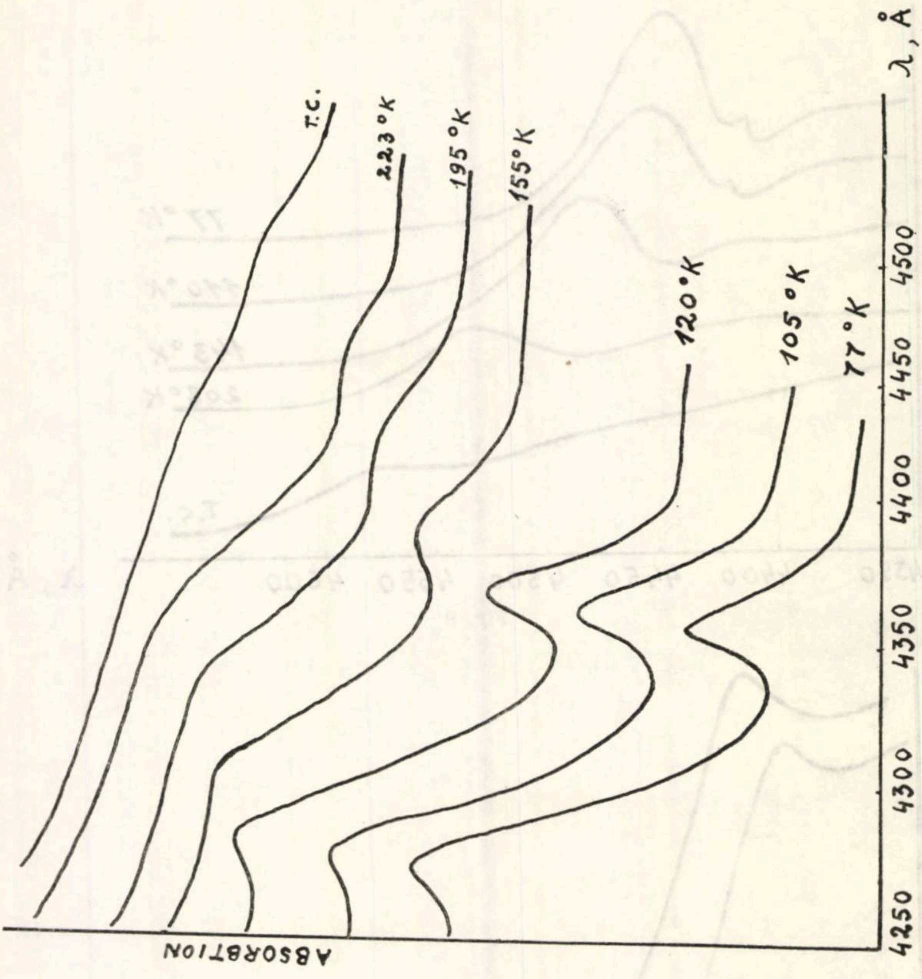
ABSORBTION
T.C.
223 °K
195 °K
155 °K
120 °K
105 °K
77 °K
4250
4300
4350
4400
4450
4500
λ, Å

Fig. 12

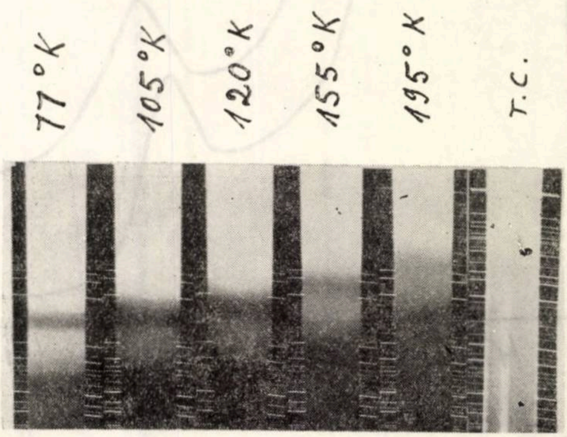
77 °K
105 °K
120 °K
155 °K
195 °K
T.C.

Fig. 11

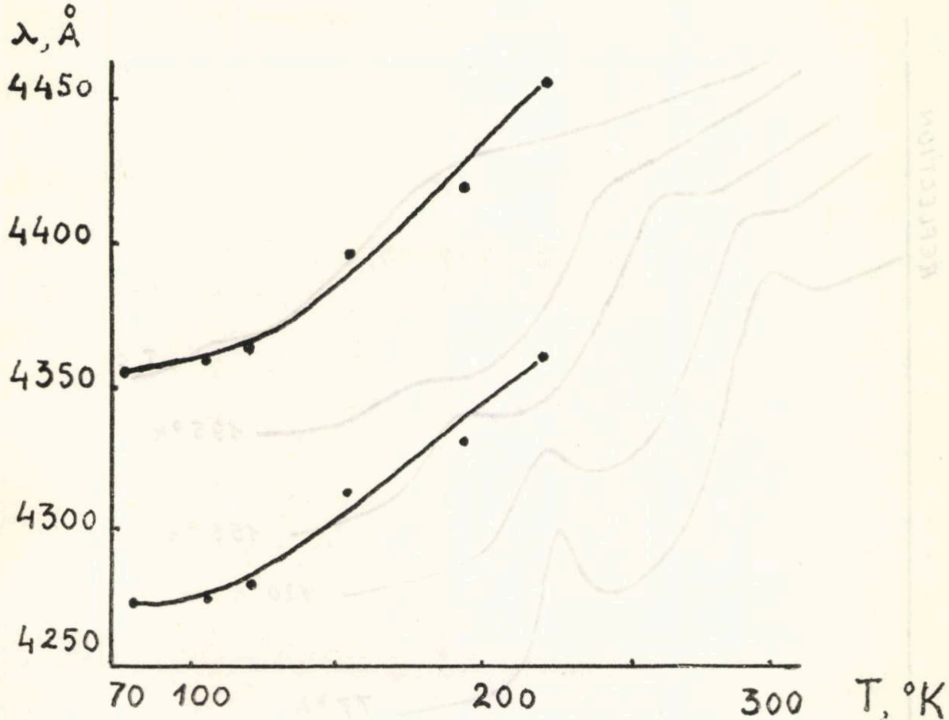
λ, Å
4450
4400
4350
4300
4250
70
100
200
300
T, °K

Fig. 13

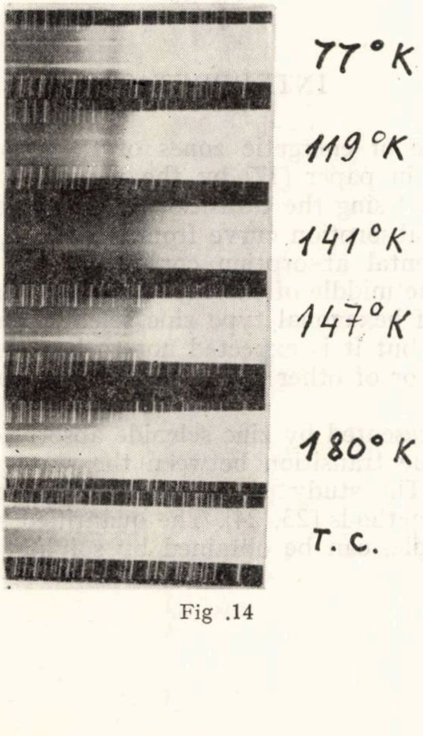
77°K
119°K
141°K
147°K
180°K
T.C.

Fig .14

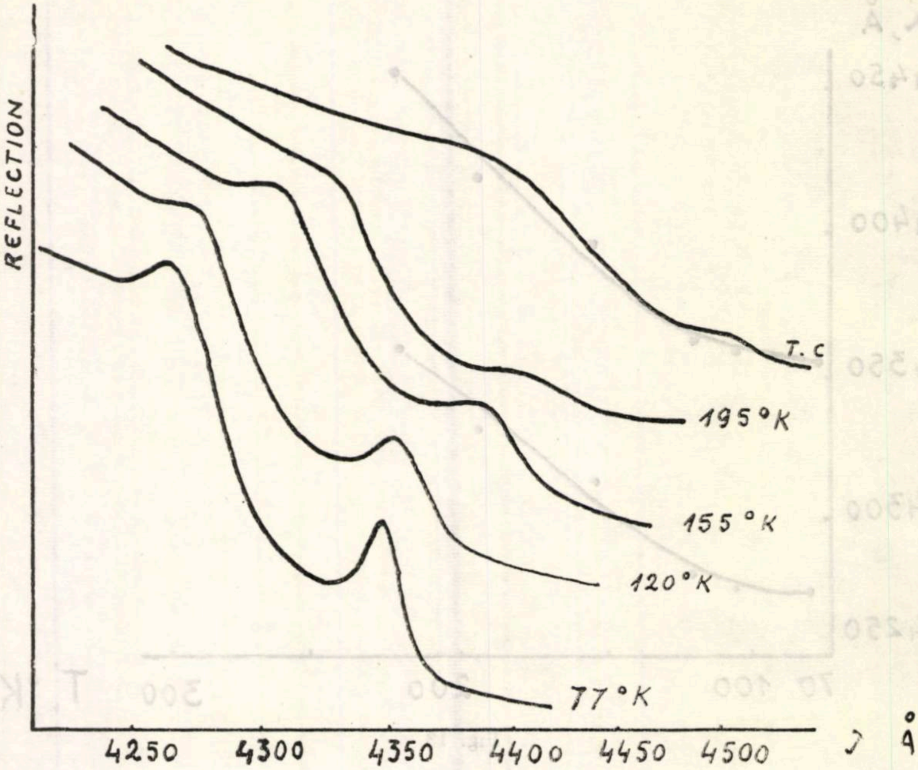

Fig .15

INTERPRETATION

a. The structure of energetic zones of the cubic type zinc selenide has been established in paper [17] by the pseudopotential method and is represented in fig. 16. Using the transitions represented in this figure, all the particularities of the absorption curve from fig. 2c. can be understood. The edge of the fundamental absorption corresponds to the direct transition $\Gamma_{15} \rightarrow \Gamma_1$, placed in the middle of the first Brillouin zone ($k = 0$).

The structure of hexagonal type zinc selenide energetic zones has not been yet established, but it is expected not to be essentially different from that of zinc sulphide or of other substances of hexagonal type with similar optical properties.

b. The peaks presented by zinc selenide absorption edge spectrum can be associated with the transition between the states of the parabolic type excition [4, 5, 6, 16]. The study of the exciton properties is based on the quantum mechanics methods [23, 24]. The quantified expression of the exciton energy, in principle, can be obtained by solving Schrodinger equation

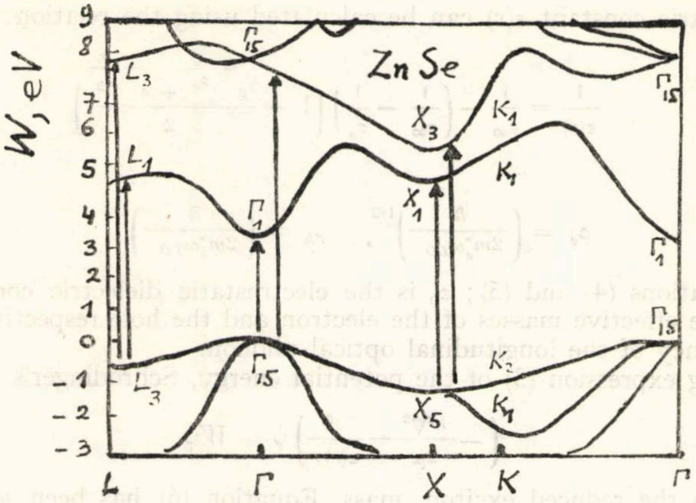

Fig. 16

To write Schrodinger's equation it is necessary to establish the expression of the potential energy of the electron in the field of the hole. The potential energy is in dependency on the lattice polarisation that appears during the electron revolution round the hole. For small radius and high speeds of the electron the potential energy takes the form:

$$W_p = -\frac{e^2}{r} \tag{1}$$

Relation (1) is valid at higher revolution frequencies than the valence electron resonance frequency because the lattice fails to polarisate. At longer radius and frequencies comparable with the resonance one the following relation is valid:

$$W_p = -\frac{e^2}{\varepsilon_\infty r} \tag{2}$$

where ε_∞ is the dielectric constant, for optical frequencies, that can be taken as equal with the square of the refraction index. In the case of relation (2), the valence electrons only participate to the lattice polarisation. Finally, at long exciton radius and low frequencies, when other electrons participate to the lattice polarisation too, the potential energy becomes:

$$W_p = -\frac{e^2}{\varepsilon(r)\, r} \tag{3}$$

The dielectric constant ε(r) can be calculated using the relation:

$$\frac{1}{\varepsilon(r)} = \frac{1}{\varepsilon_\infty} - \left(\frac{1}{\varepsilon_\infty} - \frac{1}{\varepsilon_0}\right)\left(1 - \frac{e^{-\frac{r}{\rho_e}} + e^{-\frac{r}{\rho_h}}}{2}\right) \tag{4}$$

where

$$\rho_e = \left(\frac{\hbar}{2m_e^*\omega_{LO}}\right)^{1/2}, \quad \rho_h = \left(\frac{\hbar}{2m_h^*\omega_{LO}}\right)^{1/2} \tag{5}$$

In the relations (4) and (5); ε_0 is the electrostatic dielectric constant; m_e^*, m_h^*, are the effective masses of the electron and the hole respectively; ω_{LO} is the frequency of the longitudinal optical phonon.

Using expression (3) of the potential energy, Schrodinger's equation is

$$\left(-\frac{h^2\nabla^2}{2\mu} - \frac{e^2}{\varepsilon(r)\,r}\right)\psi = W\psi \tag{6}$$

where μ is the reduced exciton, mass. Equation (6) has been solved for a small particular cases founding for the exciton energy a hydrogenoid type spectrum. The quantified expression of the exciton energy, frequently compared with experimental data, has the form;

$$W = W_g - \frac{\mu e^2}{2h^2 n^2 \varepsilon^2} \tag{7}$$

where W_g is the energetic interval of the forbidden zone; n, the quantum number takes integer values ($n = 1, 2, 3, \ldots$).

If ε values are known, the relation (7) will allow the calculation of the reduced exciton mass. In zinc selenide case, after we estimated from experimental data $W_g - W = 0.4\,eV$, we found $\mu = 0.948\ \mathrm{m}_0$.

Nevertheless the relation (7) is more used in order to identify the absorption peaks from the fundamental absorption edge, observed either in transmitted or in reflected light.

c. The three peaks observed in transmitted light, in the case of cubic structure (fig. 5) can be associated, only aproximatelly, to the first three quantum states of the exciton: the maximum λ_1 coresponds to the transition on the state $n = 1$, for λ_2, $n = 2$, and for λ_3, $n = 3$ [5]. In reflected light there are too three peaks (fig. 5) that can be associated in order to the same exciton states.

We must notice that the study of the monocrystal absorption, in reflected light, has put into evidence two peaks only associated to the states with $n = 1$ and $n = 2$ [4]. We have observed a third peak between the two descovered in the monocrystal case. Comparing our results with those from paper [4] we reached the conclusion that the new peak must be associated to the state with $n = 2$ and second peak descovered in the monocrystal case must be associated to the state with $n = 3$.

In the case of the peaks observed by us, in reflected light, it must underlined the fact that the peak denoted with λ_1 ($n = 1$) is much broader and displaced towards longer wavelengths with respect to the same peak found in transmitted light. The broadening as well as the displacement of the peak can be provoked by the increasing of the number of defects on the model surface. The exciton interaction with these defects leads to shortening of the life time in the state $n = 1$ and to broadening of the peak corresponding to this state.

d. The hexagonal structure absorption peaks, in transmitted as well as in reflected light (fig. 10), can be associated, in order, to the first states of the exciton: $\lambda_1(n = 1)$, $\lambda_2(n = 2)$ [6].

It must be remarked the fact that the peaks of the hexagonal crystalline structure are sensibly broader than in the case of the cubic one. We assume that this fact is owed either to the larger ionic percentage of the chemical-bond or to the increasing of the defect number in the hexagonal type layers compared with the cubic type case.

e. In the peaks displacing process with the temperature, is obvious the existence of a temperature with a special signification, $110° - 120°K$. This temperature can be considered as the boundary between two exciton-phonon interaction mechanisms, or as a jump moment in the behaviour of one and the same type of phonons. This temperature, for exciton-phonon interaction could be what the Debye temperature is for electron-phonon interaction [25]. On one hand under $110°K$ temperature (cubic structure) or $120°K$ (hexagonal structure) an asymmetry can intervene between the phonon emission and absorption. The symmetry is reestablished at higher temperatures. On another hand the mentioned temperature can be considered as a boundary value, from which, at exciton-phonon interaction a definite phonon energy plays a role (or a phonon with definite energy). Replacing in relation $kT = h\nu$ $T = 110°K$ and $T = 120°K$, we obtain the wavenumbers for the two crystalline structures $\tilde{\nu} = 76$ cm^{-1} (cubic), $\tilde{\nu} = 83$ cm^{-1} (hexagonal). The absorption spectrum in infrared had to manifest peaks pointing these two wavenumbers, for the tow crystalline structures.

f. The comparison of our results with those obtained on monocrystal leads to the conclusion that a fundamental absorption edge structure complete study can be made using thin films policrystalline models, obtained, relatively simply and quickly, by the method of deposition in vacuum.

REFERENCES

G. A. Zholkevich, Thesis, Leningrad (1959)
G. A. Zholkevich, Fiz. tverd. Tela, *2*, 1115 (1960)
D. T. F. Marple, B. Segall and M. Aven, Bul. Am. Phys. Soc., *6*, (1961)
M. Aven, D. T. F. Marple and B. Segall, J. Appl. Phys. Suppl., *32*, n. 10 (1961)
E. F. Gross, L. C. Suslina and P. A. Konkov, Fiz. tverd. Tela, *4*, n. 3 (1962)
E. F. Gross, B. S. Razbirin and V. I. Safarov, Fiz. tverd. Tela, *2*, n. 2 (1960)
K. V. Shalimova, T. S. Travina and L. L. Golik DAN SSSR, *138*, n. 1 (1961)
K. V. Shalimova and I. I. V. Karpenko, Radiotehnika i elektronoka, n. 2, (1958)
N. V. Pirogova, Thesis, Moscow (1962)
O. A. F. Andrusko, Thesis, Moscow (1963)
I. Spînulescu-Carnaru, Thesis, Moscow (1964)

N. K. Morozova, Thesis, Moscow (1964)
M. Cardona, Conf. phys. sem., Paris (1964)
M. Cardona and G. Harbeke, Conf. phys. sem., Paris (1964)
M. Balkanski et Y. Petroff, Conf. phys. sem., Paris (1964)
M. Cardona and G. Harbeke, J. Appl. Phys., *34*, 813 (1963)
M. L. Cohen and T. K. Bergstresser, Phys. Rev., *141*, 789 (1966)
T. K. Bergstresser and M. L. Cohen, Phys. Rev., *164*, 1069 (1967)
I. Dima, Thesis, Moscow (1964)
K. V. Shalimova, I. Dima and N. V. Pirogova, Docl. nauc. conf. Inst. Ener. Moscow, p. 13 (1965)
K. V. Shalimova, I. Dima and N. V. Pirogova, Docl. nauc. conf. Inst. Ener. Moscow, p. 19 (1965)
I. Dima, Anal. Univ. București (Fizica) (1968)
R. S. Knox, Theory of Excitons, Acad. Press, New York (1963)
J. C. Phillips, Solid State Physics, *18*, 55 (1966)
C. N. Plăvițu, phys. stat. sol., *12*, 265 (1965)

BUDAPESTI MŰSZAKI EGYETEM
KÖZPONTI KÖNYVTÁRA
1848

Redactor principal: ȘTEFANIA BARBU
Tehnoredactor: GH. TIȚĂ

ANALELE UNIVERSITĂȚII BUCUREȘTI
FIZICĂ
Anul XIX — 1970